博士論文

Study on Spatial Mode Conversion Technique for Space Division Multiplexing

空間分割多重通信における空間モード変換技術に関する研究

北海道大学大学院情報科学院

張　霜露

Contents

List of Figures

Chapter 2

Chapter 3

Chapter 4

Chapter 5

List of Tables

Chapter 3

Chapter 4

Chapter 5

Chapter 1

Overview

1.1 Research background

Optical communication is a communication approach that uses light to carry information. Optical communication can be dated back to antiquity; however, the distance as well as the rate at which information could be transmitted is limited [1]. When French inventor Claude Chappe invented the optical semaphore telegraph in 1792 which was the first optical telecommunication system that spread throughout Europe [2]. The messages can be mechanically coded over long distances using intermediate relay stations. However, it was soon eclipsed by electrical telecommunication systems based on the telegraph and telephone lines. In the 1960s, the invention of the laser [3] which reawakened interest in the possibility of using light as the medium of communication. Subsequently, Charles Kuen Kao who is known as the "father of fiber optics communication" illustrated a critical and theoretical specification in 1964 about the losses of optical fibers could be reduced by removing impurities from silica glass [4], enabling optical fibers to be the communication medium. Optical communication started developing dramatically with the invention of the first semiconductor laser diode to radiate continuously at room temperature [5] and the appearance of low-loss fiber (20 dB/km) [6]. By the end of the 1980s, optical communication based on single mode fibers (SMFs) was mainly used because it can stably transmit a single spatial mode in a long-distance optical fiber transmission network and achieved Gbit/s class transmission capacity combined with optical time division multiplexing (OTDM) technique [7]. The transmission capacity of optical communication based on SMFs exponentially increased due to the emergence of advanced new technologies. In the mid of 1990s, while the Erbium-Doped Fiber Amplifier (EDFA) [8] and the wavelength division multiplexing (WDM) technique [9] were proposed, the optical communication made significant progress, and Tbit/s class transmission capacity was reached. Recent SMF transmission systems have achieved capacity up to about 100Tb/s per fiber [10] by employing various multiplexing techniques such as WDM, time division multiplexing (TDM) [11], polarization division multiplexing (PDM) [12], and multi-level modulation (e.g., phase-shift keying [13], quadrature amplitude modulation [14,15]).

However, nowadays communication traffic has been increasing at an annual growth rate between 30% and 60% [16] which leads to the notion of "optical communication capacity crunch" [17,18] as

the capacity of SMF transmission systems approaches its fundamental limit owing to Shannon effects and fiber fuse phenomenon [19,20]. Realizing that spectral efficiencies over the required transmission distances are no longer scalable, alternative solutions have to be developed. Space division multiplexing (SDM) technology [21-24] as the preferred solution for network capacity growth is proposed and developed. It can use space dimension to construct signal channels for multiplexing in optical communication. Spatial utilization in SMFs is quite poor because its structure allows only one propagation mode whereas the density of optical power and the capacity of payload reached the limit of one core. In contrast, SDM fibers have a larger core diameter, which allows multiple modes/cores to be contained in one fiber. The transmission capacity of SDM systems can be improved in proportion to the number of cores/modes owing to each mode/core can be treated as an independent optical path. SDM technology typically consists of two approaches: the core multiplexing based on multi-core fibers (MCFs) [25,26] which have multiple cores within a fiber cable, and the mode division multiplexing (MDM) based on the few-mode fibers (FMFs) or multi-mode fibers (MMFs) [27-30] which allow multiple spatial-mode to propagate in one fiber. In MCFs, the transmission capacity is increased related to the number of cores due to each individual core being treated as an independent waveguide. In MDM systems, since the spatial modes are orthogonal to each other, each spatial mode can be treated as an independent transmission channel. More recently, dense SDM (DSDM) using few-mode multicore fibers (FM-MCFs) with a large spatial multiplicity exceeding 30 have considerable potential for meeting the large capacity. The transmission multiplicity is expanded to 32 multi-cores with transmission distances over 1600 km in low cross-talks has been achieved [31] and enabling optical fibers with over 100 spatial channels and total bit rates over 10 Pbit/s when using both the C and L bands [32]. Besides, SDM combined with conventional multiplexing techniques can further increase the transmission capacity. However, it is noted that deploying SDM in its most trivial form by using M parallel optical paths is a scalable but not yet economically sustainable path forward since the consumption of cost and energy is also M times. Thus, SDM must not only increase the capacity, but also reduce the cost and increase energy efficiency [33].

On the other hand, the integration and flexibility of SDM systems are critical keys for optical communication. An optical network is not as simple as using only one type of fiber, which SMF is preferred to use in long-distance and SDM fiber is used for short-distance transmission. Thus, mode conversion techniques are essential for mode-to-mode and fiber-to-fiber conversion in optical applications which support SDM components and links added to the existing non-SDM infrastructure. Mode conversion techniques have various of types such as photonic lanterns [34,35], optical fiber coupler [36], waveguide-type using plane light wave circuit (PLC) [37-40], and free-space optics using beam splitters and phase plates [41] and so on. Although the PLC-based scheme is developed as the main scheme due to its advantages of compactness, low insertion loss, and easy integration, the ability of multiplexity is restricted due to its tiny structure. The free-space optics-based scheme has the

characteristics of high multiplexity, but the scale becomes complicated with the expanding number of phase plates and beam splitters. Recently, the multi-plane light conversion (MPLC) scheme [45,46] of free-space optics has attracted widespread attention due to low loss and high mode selectivity. However, the scale of equipment, configuration complexity, and manufacturing increase as the number of multiplexity increases. Thus, advanced mode conversion techniques with small size, low cost, and high mode selectivity are essential to realizing SDM systems in optical applications.

1.2 Research purpose

In this study, to realize simplified cost-efficient SDM optical networks with switching flexibility and scaling potential, we propose two spatial mode conversion schemes for mode-to-mode and fiber-to-fiber conversion. In MDM systems, the transmission quality is restricted by the differential mode delay (DMD) [47-49], which is defined as the relative group delay between the propagating modes. This delay is related to the computational cost of the multi-input-multiple-output digital signal processing (MIMO-DSP) technique [50,51] developed for compensating crosstalk. In MIMO-DSP, the computation required to recover the signals at the receiver becomes more complex as the DMD between the propagation modes increases, which restricts the transmission distance. Moreover, the power consumption of the system also increases as the MIMO-DSP calculation increases. Thus, a reduction in DMD is essential to facilitate long-haul transmissions in MDM transmission systems. A mode-to-mode conversion technique using volume holograms is proposed in this study by exchanging the spatial modes with difference transmission speed to reduce the DMD. This spatial mode exchange technique using volume holograms (VHET) utilizes multiplexed volume holograms to exchange multiplexed spatial mode. The cost and size of the optical system are markedly lower because this scheme requires only a single holographic medium, which is independent of the number of multiplexed modes. This technique also can be applied for the conversion between high-order modes to realize data transmission flexibility networks. On the other hand, in FM-MCF transmission systems, it is essential to ensure that all spatial channels are routed together as a unit from the transmitter to receiver [52]. Thus, integration and implementation cost of the switching elements are decisive factors in SDM networks [53]. Although various switching elements have been proposed [55,56], no switching elements for DSDM networks have been proposed so far. Therefore, a spatial light modulator (SLM) [57-60] based optical-fiber joint switch (OFJS) is proposed herein as an switching photonic node for fiber-to-fiber conversion. This scheme is a cost-effective integration technique with a simple configuration that can switch all signal paths of the FM-MCF as a unit in an optical free space to obtain a greater throughput; in addition, it can achieve selective operation by changing the SLM display patterns. However, unlike the mode conversion techniques applied in SMF transmission systems, crosstalk is a serious issue that must be considered in SDM transmission systems since integration generally comes at the expense of crosstalk among parallel optical paths. Thus, based on the noted

above schemes, we further propose improved methods to suppress the crosstalk.

1.3 Chapter outlines

Spatial mode conversion schemes applied in SDM systems are proposed in this study. Chapter outlines are shown as follows.

- **Chapter 1:** We review the development of optical communication and then introduce the research background and the purpose of this study.
- **Chapter 2**: The configuration and key technologies of SDM transmission systems are introduced in this chapter. We first introduce the structure and classification of the optical fibers, and then describe the configuration of MDM transmission systems. The principle and characteristics of Volume Holograms (VHs) and SLMs as the primary components used for mode conversion are finally introduced in detail. Besides, the classification of crosstalk is discussed, which is an important parameter to evaluate the performance of systems.
- **Chapter 3**: VHET as a spatial mode conversion technique is proposed in this chapter. Multiple spatial modes can be exchanged simultaneously using a single holographic medium. The basic principle and characteristics of VHET are introduced in detail. Subsequently, numerical simulations and experiments are conducted by using a linearly polarized (LP) mode group comprised of LP01, LP11, and LP21. A dual-wavelength method that enables VHET applied in the optical transmission bands is lastly discussed.
- **Chapter 4**: Since the conversion performance is severely degraded by crosstalk owing to the non-target holograms, VHET combined with phase plates is proposed in this chapter to suppress the crosstalk by modulating the intensity distribution of light signals. To confirm the basic operation of the proposed methods, numerical simulations of a specific LP mode group are performed. The simulation results of three improved methods are then discussed.
- **Chapter 5**: An SLM-based OFJS for FM-MCFs is proposed in this chapter to realize DSDM networks with routing flexibility and scaling potential. This scheme can switch all signal paths of the FM-MCF as a unit and achieve selective operation by changing the SLM display patterns. Subsequently, numerical simulations and experiments by jointly switching optical signals and routing them in a specified direction are demonstrated. Further, the method of changing the position of the output port to reduce the port crosstalk is described and performed.
- **Chapter 6**: We summarize the research results of this study and describe the prospects of our research.

References

[1] G. P. Agrawal, “Optical communication: its history and recent progress,” Optics in our time, edited by M. D. A. Amri, M. M. E. Gomati, M. S. Zubairy, Springer publisher, 2016, 177-199.

[2] L. U. J. Chappe, (1824) Histoire de la télégraphie, Chez l'auteur, University of Michigan Library.

[3] G. Friedman, “The light fantastic: Ted Maiman and the world’s first laser,” OE Reports, 2000.

[4] K. C. Kao and G. A. Hockham, “Dielectric-fibre surface waveguides for optical frequencies,” Proc. IEE **133** (7),1151-1158 (1966).

[5] I. Hayashi, M. B. Panish, and P. W. Foy, “Junction lasers which operate continuously at room temperature,” Appl. Phys. Lett. **17** (3), 109 (1970).

[6] F. P. Kapron, D. B. Keck, and R. D. Maurer, “Radiation losses in glass optical waveguides,” Appl. Phys. Lett. **17**(10), 423 (1970).

[7] R. S. Tucker, G. Eisenstein, S. K. Korotky, “Optical time-division multiplexing for very high bit-rate transmission,” J. Light. Technol. **6**(11), 1737-1749 (1988).

[8] M. Nakazawa, Y. Kimura, and K. Suzuki, “Efficient Er3+-doped optical fiber amplifier pumped by a 1.48 μm InGaAsP laser diode,” Appl. Phys. Lett. **54**, 295 (1989).

[9] H. Takahashi, S. Suzuki, and K. Kato, “Arrayed-waveguide grating for wavelength division multi/demultiplexer with nanometer resolution,” Electron. Lett. **26**(2), 87 (1990).

[10] A. Sano, T. Kobayashi, S. Yamanaka, A. Matsuura, H. Kawakami, Y. Miyamoto, K. Ishihara, and H. Masuda, “102.3-Tb/s (224 × 548-Gb/s) C- and extended L-band all-Raman transmission over 240 km using PDM-64QAM single carrier FDM with digital pilot tone,” Opt. Fiber Commun. Conf., CA, PDP5C.3(2012).

[11] W. R. Bennett, “Time division multiplex systems, ” in Bell Syst. Tech. J. **20**(2) 199-221 (1941).

[12] K. Iwatsuki, K. Suzuki, S. Nishi, and M. Saruwatari, “80 Gb/s optical soliton transmission over 80 km with time/polarization division multiplexing, ” in IEEE Photon. Technol. Lett. **5**(2), 245-248 (1993).

[13] S. Park, K. Hong, Y. S. Jang, and K. Kim, “One the WDM transmission using multilevel (M>4) DPSK modulation format”, IEEE Photon. Technol. Lett. 17(7), 1546-1548 (2005).

[14] Y. Mori, C. Zhang, K. Igarashi, K. Katoh, and K. Kikuchi, “Transmission of 40-Gbit/s 16-QAM signal over 100-km standard single-mode fiber using digital coherent optical receiver”, 34th Eur. Conf. Opt. Commun., Tu.1.E.4, 53-54 (2008).

[15] K. Kikuchi, “Analyses of wavelength- and polarization-division multiplexed transmission characteristics of optical quadrature-amplitude-modulation signals,” Opt. Express **19**(19), 17985-17995 (2011).

[16] P. J. Winzer, R. Ryf, and S. Randel, “Spatial multiplexing using multiple-input multiple-output signal processing,” 6th Optical fiber telecommunications VIB, edited by I. P. Kaminow, T. Li and A. E. Willner, Elsevier publisher, 2013.

[17] A. Chralyvy, “Plenary paper: The coming capacity crunch, ” 35th Eur. Conf. Opt. Commun., 2009.

[18] R. J. Essiambre and R. W. Tkach, “Capacity trends and limits of optical communication networks,” Proc. IEEE **100**(5), 1035-1055 (2012).

[19] M. Secondini and E. Forestieri, “The limits of the nonlinear Shannon limit,” Proc. Optical Fiber

Communication Conf. (OFC), 2016, Th3D.1.

[20] S. Todoroki, "Transient propagation mode of fiber fuse leaving no voids," Opt. Express **13**(23), 9248-9256 (2005).

[21] D. J. Richardson, J. M. Fini, and L. E. Nelson, "Space-division multiplexing in optical fibres," Nat. Photonics **7**(5), 354-362 (2013).

[22] Y. Awaji, "Review of space-division multiplexing technologies in optical communications," IEICE Trans. Commun. **E102-B**(1), 1-16 (2019).

[23] Y. Miyamoto and R. Kawamura, "Space Division Multiplexing Optical Transmission Technology to Support the Evolution of High-capacity Optical Transport Networks," NTT Tech. Rev. **15** (6), 1-7 (2017)

[24] B. Zhu, J. M. Fini, M. F. Yan, X. Liu, S. Chandrasekhar, T. F. Taunay, M. Fishteyn, E. M. Monberg, and F. V. Dimarcello, "High-capacity space-division-multiplexed DWDM transmissions using multicore fiber," J. Light. Technol. **30**(4), 486-492 (2012).

[25] K. Takeshima, T. Tsuritani, Y. Tsuchida, K. Maeda, T. Saito, K. Watanabe, T. Sasa, K. Imamura, R. Sugizaki, K. Igarashi, I. Morita, and M. Suzuki, "51.1-Tbit/s MCF transmission over 2520 km using cladding-pumped 7-core EDFAs," J. Light. Technol. **34**(2), 761-767 (2016).

[26] H. Takara, T, Mizuno, H. Kawakami, Y. Miyamoto, H. Masuda, K. Kitamura, H. Ono, S. Asakawa, Y. Amma, K. Hirakawa, S. Matsuo, K. Tsujikawa, and M. Yamada, "120.7-Tb/s MCF-ROPA unrepeated transmission of PDM-32QAM channels over 204 km," J. Light. Technol. **33**(7), 1473-1478 (2015).

[27] S. Berdagué and P. Facq, "Mode division multiplexing in optical fibers," Appl. Opt. **21**(11), 1950-1955 (1982).

[28] E. Ip, M. J. Li, K. Bennett, Y-K. Huang, A. Tanaka, A. Korolev, K. Koreshkov, W. Wood, E. Mateo, J. Hu, and Y. Yano "146λ×6×19-Gbaud wavelength and mode-division multiplexed transmission over 10×50km spans of few-mode fiber with a gain-equalized few-mode EDFA," J. Light. Technol. **32**(4), 790-797 (2013).

[29] A. Li, X. Chen, A. A. Amin, J. Ye, and W. Shieh, "Space-division multiplexed high-speed Ssuperchannel transmission over few-mode fiber," J. Light. Technol. **30**(24), 3953-3964 (2012).

[30] R. Ryf, S. Randel, A. H. Gnauck, C. Bolle, A. Sierra, S. Mumtaz, M. Esmaeelpour, E. C. Burrows, R.-J. Essiambre, P. J. Winzer, D. W. Peckham, A. H. McCurdy, and R. Lingle, "Mode-division multiplexing over 96 km of few-mode fiber using coherent 6 × 6 MIMO processing," J. Light. Technol. **30**(4), 521-531 (2012).

[31] T. Mizuno, K. Shibahara, H. Ono, Y. Abe, Y. Miyamoto, F. Ye, T. Morioka, Y. Sasaki, Y. Amma, K. Takenaga, S. Matsuo, K. Aikawa, K. Saitoh, Y. Jung, D. J. Richardson, K. Pulverer, M. Bohn, and M. Yamada, "32-core Dense SDM unidirectional transmission of PDM-16QAM signals over 1600 km using crosstalk-managed single-mode heterogeneous multicore transmission line," Optical Fiber Communication Conference and Exhibition (OFC), Anaheim, CA, Th5C.3 (2016).

[32] D. Soma, Y. Wakayama, S. Beppu, S. Sumita, T. Tsuritani, T. Hayashi, T. Nagashima, M. Suzuki, M. Yoshida, K. Kasai, M. Nakazawa, H. Takahashi, K. Igarashi, I. Morita, and M. Suzuki, "10.16-peta-b/s dense SDM/WDM transmission over 6-mode 19-core fiber across the C+L band," J. Light. Technol. **36**(6), 1362-1368 (2018).

[33] P. J. Winzer, "Energy-efficient optical transport capacity scaling through spatial multiplexing," IEEE Photon. Tech. Lett. **23**(13), 851-853 (2011).

[34] S. G. L-Saval, N. K. Fontaine, J. R. S-Gil, B. Ercan, R. Ryf, and J. B-Hawthorn, "Mode-selective photonic lanterns for space-division multiplexing," Opt. Express **22**(1), 1036-1044 (2014).

[35] N. K. Fontaine, R. Ryf, J. Bland-Hawthorn, and S. G. Leon-Saval, "Geometric requirements for photonic lanterns in space division multiplexing," Opt. Express **20**(24), 27123-27132 (2012).

[36] N. Hanzawa, K. Saitoh, T. Sakamoto, T. Matsui, S. Tomita, and M. Koshiba, "Mode-division multiplexed transmission with fiber mode couplers," Optical Fiber Communication Conference and Exposition (OFC/NFOEC), Los Angeles, CA, OW1D.4 (2012).

[37] N. Hanzawa, K. Saitoh, T. Sakamoto, T. Matsui, K. Tsujikawa, M. Koshiba, and F. Yamamoto "Two-mode PLC-based mode multi/demultiplexer for mode and wavelength division multiplexed transmission," Opt. Express **21**(22), 25752-25760 (2013).

[38] H. Kubota, M. Oguma, and H.Takara, "Three-mode multi/demultiplexing experiment using PLC mode multiplexer and its application to 2+1 mode bi-directional optical communication," IEICE Electron. Expr. **10**(12), 1-6 (2013).

[39] Y. Yamashita, S. Makino, T. Fujisawa, N. Hanzawa, T. Sakamoto, T. Matsui, K. Tsujikawa, F. Yamamoto, K. Nakajima, and K. Saitoh , "PLC-Based LP_{11}mode rotator with curved trench structure devised from wavefront matching method," IEEE Photon. Tech. Lett. **29**(13), 1063-1066 (2017).

[40] Y. Chaen, K. Tanabe, H. Jiang, and K. Hamamoto, "Low Wavelength Dependency Design for MMI (Multi-Mode Interference) Mode Converter," IEICE Electron. Expr. **12**(20), 20150727 (2015).

[41] S. Shwartz, M. A. Golub, and S. Ruschin, "Computer-generated holograms for fiber optical communication with spatial-division multiplexing," Appl. Opt. **56**(1), A31-40 (2017).

[42] W. Q. Thornburg, B. J. Corrado, and X. D. Zhu, "Selective launching of higher-order modes into an optical fiber with an optical phase shifter," Opt. Lett. **19**(7), 454-456 (1994).

[43] K. Igarashi, D. Souma, T. Tsuritani, and I. Morita, "Performance evaluation of selective mode conversion based on phase plates for a 10-mode fiber," Opt. Express **22**(17), 20881-20893 (2014).

[44] K. Igarashi, D. Soma, K. Takeshima, and T. Tsuritani, "Selective mode multiplexer based on phase plates and Mach-Zehnder interferometer with image inversion function," Opt. Express **23**(1), 183-194 (2015).

[45] G. Labroille, B. Denolle, P. Jian, P. Genevaux, N. Treps, and J. F. Morizur, "Efficient and mode selective spatial mode multiplexer based on multi-plane light conversion," Opt. Express **22**(13), 15599-15607 (2014).

[46] N. Fontaine, R. Ryf, H. Chen, D. Neilson, and J. Carpenter, "Design of high order mode-multiplexers using multiplane light conversion," Eur. Conf. Opt. Commun., Tu.1.F.4. (2017).

[47] T. Sakamoto, T. Mori, T. Yamamoto, and S. Tomita, "Differential mode delay managed transmission line for WDM-MIMO system using multi-step index fiber," J. Light. Technol. **30**(17), 2783-2787 (2012).

[48] T. Sakamoto, T. Mori, T. Yamamoto, N. Hanzawa, S. Tomita, F. Yamamoto, K. Saitoh, and M. Koshiba, "Mode-division multiplexing transmission system with DMD-independent low complexity MIMO processing," J. Light. Technol. **31**(13), 2192-2199 (2013).

[49] Y. Wakayama, D. Soma, K. Igarashi, H. Taga, and T. Tsuritani, "Intermediate mode interchange for reduction of differential mode-group delay in weakly-coupled 6-mode fiber transmission line," Proc. OFC2016, M3E.6 (2016).

[50] T. Mori, T. Sakamoto, M. Wada, T. Yamamoto, and F. Yamamoto, "Few-mode fibers supporting more than two LP modes for mode-division-multiplexed transmission with MIMO-DSP," J. Light. Technol. **32**(14), 2468-2479 (2014).

[51] K. Shibahara, T. Mizuno, D. Lee, and Y. Miyamoto, "Advanced MIMO signal processing techniques enabling long-haul dense SDM transmissions," J. Light. Technol. **36**(2), 336-348 (2018).

[52] P. J. Winzer and G. J. Foschini, "MIMO capacities and outage probabilities in spatially multiplexed optical transport systems," Opt. Express **19**(17), 16680-16696 (2011).

[53] D. M. Marom and M. Blau, "Switching solutions for WDM-SDM optical networks," IEEE Commun. Mag. **53**(2), 60-68 (2015).

[54] N. K. Fontaine, T. Haramaty, R. Ryf, H. Chen, L. Miron, L. Pascar, M. Blau, B. Frenkel, L. Wang, Y. Messaddeq, S. LaRochelle, R. J. Essiambre, Y. Jung, Q. Kang, J. K. Sahu, S. U. Alam, D. J. Richardson, and D. M. Marom, "Heterogeneous space-division multiplexing and joint wavelength switching demonstration," Proc. Opt. Fiber Commun. Conf. (OFC), Th5C.5 (2015).

[55] D. J. Bishop, C. R. Giles, and G. P. Austin, "The Lucent LambdaRouter: MEMS technology of the future here today," IEEE Communications magazine **40**(3), 75-79 (2002).

[56] A. Himeno, K. Kato, and T. Miya, "Silica-based planar lightwave circuits," IEEE J. Sel. Top. Quantum Electron. **4**(6), 913-924 (1998).

[57] M. Wang, L. Zong, L. Mao, A. Marquez, Y. Ye, H. Zhao, and F. J. V. Caballero, "LCoS SLM study and its application in wavelength selective switch," Photonics **4**(2), 22 (2017).

[58] Z. Guo, J. Yan, Y. Xing, Y. Zheng, and Q. Li, "A novel three electrodes structure LCoS with low fringing field effect," SID Symp. Dig. Tech. Papers **47**(1), 183-184 (2016).

[59] M. Persson, D. Engström, and M. Goksör, "Reducing the effect of pixel crosstalk in phase only spatial light modulators," Opt. Express **20**(20), 22334-22343 (2012).

[60] H. Yang, B. Robertson, and D. Chu, "Crosstalk reduction in holographic wavelength selective switches based on phase-only LCOS devices," Proc. Opt. Fiber Commun. Conf. (OFC), Th2A.23 (2014).

Chapter 2

Space Division Multiplexing

2.1 Introduction

Optical fiber communication systems can carry enormous traffic volumes, which support large-capacity and long-distance communications owing to their large available bandwidths and extremely low propagation losses. Current backbone optical networks are exclusively based on single-mode fibers (SMFs) due to their advantages: the greatest transmission bandwidths, superior transmission quality over other fiber types, and the lowest losses, which are suitable for long-distance transmission. However, with the increasing demand for internet, traffic demands have reached their capacity limits for SMFs owing to the nonlinear Shannon effects and fiber fuse phenomenon [1,2]. The Shannon-Hartley theorem [3] indicates the maximum rate at which information can be transmitted over a communications channel of a specified bandwidth in the presence of noise, and is expressed as

$$C = B\log_2\left(1+\frac{S}{N}\right) \tag{2.1}$$

where C is the channel capacity in bits per second, B is the bandwidth of the channel in hertz, S is the average received signal power over the bandwidth, N is the average power of the noise and interference over the bandwidth, S/N is the signal-to-noise ratio of the communication signal to the noise and interference at the receiver. It seems that the transmission capacity can be expanded by increasing the signal power S. However, the phenomenon of fiber fuse, a kind of catastrophic damage, limits the spectrum efficiency and troubles all silica-based optical fibers. Realizing that spectral efficiencies over the required transmission distances are no longer scalable, alternative solutions have to be developed. Space division multiplexing (SDM) as the preferred solution for network capacity growth is proposed and developed which uses space dimension to construct signal channels. SDM technology includes two approaches: mode-division multiplexing (MDM) using few-mode fibers (FMFs) or multi-mode fibers (MMFs) and core multiplexing using multi-core fibers (MCFs). SDM technology treats each core/mode as an independent optical path; thus, the capacity can be improved in proportion to the number of cores/modes. To realize simplified cost-efficient SDM optical networks with switching flexibility and scaling potential, mode conversion techniques are essential for mode-to-mode and fiber-

to-fiber conversion in optical applications. In this study, we propose two spatial mode conversion schemes: the spatial mode exchange technique using volume holograms (VHET) for mode-to-mode conversion and the spatial light modulator (SLM) based optical-fiber joint switch for fiber-to-fiber conversion. For better understanding, in this chapter, we first introduce the structure and classification of the optical fibers, and then described the configuration of MDM transmission systems. The volume holography (VH) and spatial light modulator (SLM) as the key components used for the mode conversion are finally introduced in detail.

2.2 Optical fiber

2.2.1 Classification of optical fibers

Optical fiber [4,5], a fiber made of glass or plastic, is used as a light transmission tool that permits signals to transmit over longer distances with low loss. Figure 2.1 shows the structure of an optical fiber consisting of a core, cladding, and coating. The fiber core is in the center of the fiber which optical energy is transmitted in. The fiber cladding is located around the core, providing a reflective surface and optical isolation for the transmission of light. The refractive index of the fiber core is slightly higher than that of the cladding. The coating is the outermost layer to protect the optical fiber from the external environment such as moisture and mechanical scratches. Figure 2.2 shows the conceptual diagram of light transmission in an optical fiber. Based on the structure of optical fibers, when a light propagates in a core with an angle θ which lower than a certain angle of θ_c, the light can be reflected into the core. Here, θ_c is called critical angle of the total reflection and calculated by Snell's law

$$\theta < \theta_c = \cos^{-1}\left(\frac{n_{\text{clad}}}{n_{\text{core}}}\right) \tag{2.2}$$

where n_{core} is the refractive index of the core and n_{clad} is the refractive index of the cladding. When the difference of refractive index between the core and cladding is extremely small <<1, the relative refractive index difference Δ is expressed as

$$\Delta = \frac{n_{\text{core}}^2 - n_{\text{clad}}^2}{2n_{\text{core}}} \approx \frac{n_{\text{core}} - n_{\text{clad}}}{n_{\text{core}}} \tag{2.3}$$

When the limiting case for total internal reflection is considered, θ is equal to the critical angle θ_c. We assume that the external medium is air where n_{air} is unity and equal to 1. The maximum acceptance angle θ_{max}, which is the maximum incidence angle of a light ray that able to enter the fiber, is expressed as

$$2\theta_{\max} = 2\sin^{-1}(n_{\text{core}}\sin\theta_c) \cong 2\sin^{-1}(\sqrt{n_{\text{core}}^2 - n_{\text{clad}}^2}) \tag{2.4}$$

The numerical aperture (NA) of a fiber is a useful measure of the light gathering capability, and is expressed as

$$NA = \sin\theta_{\max} \approx n_{\text{core}}\sqrt{2\Delta} \tag{2.5}$$

So far, we have described the basic principles of light transmission in optical fibers. It is noted that not all light that satisfies the total reflection condition can propagate through the optical fiber, only the specific light whose incident angle satisfies a certain angle can stably exist in the optical fiber. Those specific lights are called spatial modes. We will describe it in detail in Section 2.2.2.

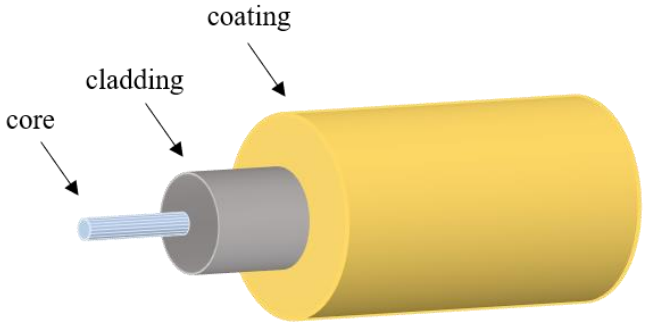

Figure 2.1. Structure of an optical fiber.

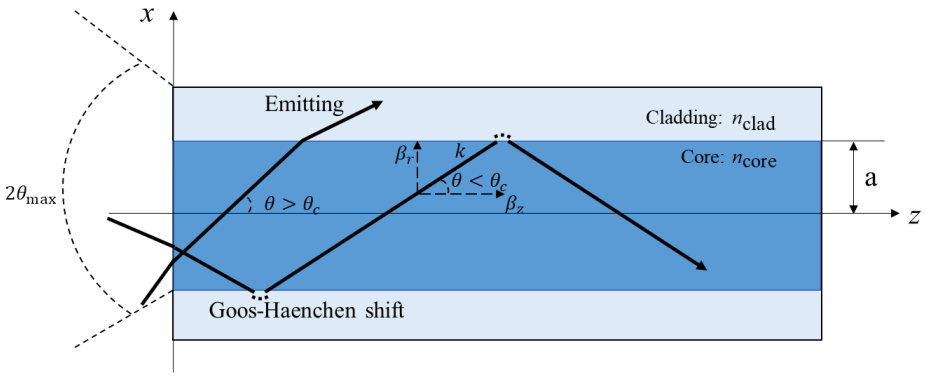

Figure 2.2. Conceptual diagram of light transmission in the optical fiber.

Optical fibers typically categorized based on the refractive index profile and modes number. Based on the refractive index profile, optical fibers are classified into step-index (SI) fibers and graded-index (GI) fibers. Figure 2.3(a) shows the refractive index profile of SI fiber with a core of constant refractive index and a cladding of a slightly lower refractive index. The refractive index profile of SI fiber makes a step change at the core-cladding interface. Figure 2.3(b) shows the refractive index profile of GI

fiber with a core of decreasing refractive index along the radial distance and a cladding of constant refractive index. The refractive index of the core is higher at the center and gradually decreases as the interface approaches. The r is the distance from the center of the core, a is the core radius and α determines the index profile in GI fibers. The refractive index distribution $n(r)$ can be expressed as

SI fiber
$$n(r)=\begin{cases} n_{\text{core}} & (r<a) \\ n_{\text{clad}} & (r\geq a) \end{cases} \tag{2.6}$$

GI fiber
$$n(r)=\begin{cases} n_{\text{core}}\sqrt{1-2\Delta\left(\dfrac{r}{a}\right)^{\alpha}} & (r<a) \\ n_{\text{core}} & (r\geq a) \end{cases} \tag{2.7}$$

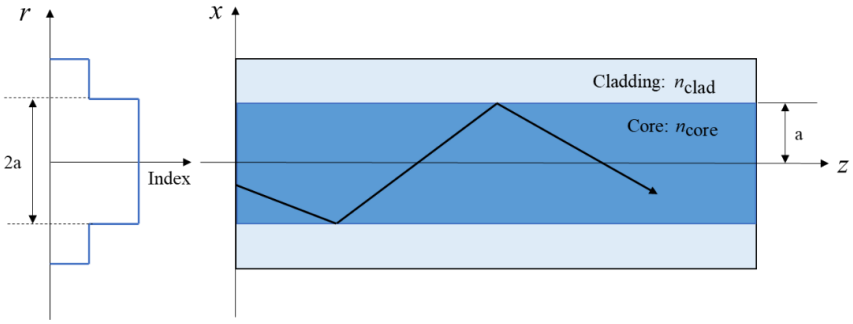

(a) Step-index fiber

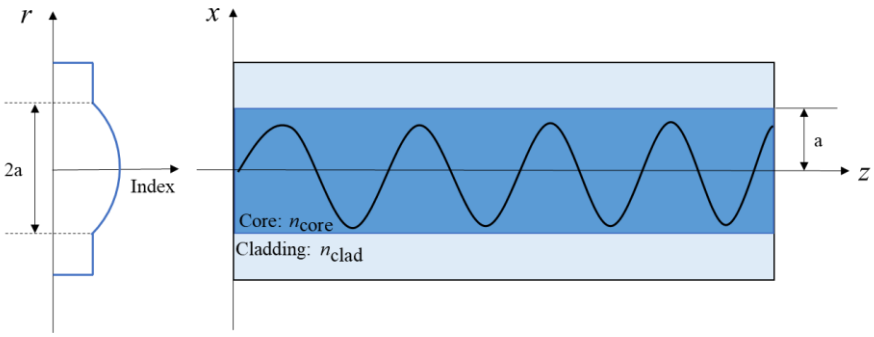

(b) Graded-index fiber

Figure 2.3 Refractive index profiles of SI fiber and GI fiber.

Based on the number of modes supported, optical fibers are classified into SMF and MMF. Firstly, we introduce the concept of spatial modes by geometrical optics. We assume a light wave propagates in an SI fiber with an angle of θ, the propagation constant is expressed as

$$k = n_{core}\frac{2\pi}{\lambda} \tag{2.8}$$

where k is the wave number and λ is the free spatial wavelength. The propagation constant in the propagation direction and radial direction can be determined by

$$\beta_z = k\cos\theta \tag{2.9}$$

$$\beta_r = k\sin\theta \tag{2.10}$$

respectively. Since the radial component is reflected at the core-cladding interface, a standing wave in the radial direction will be generated when the phase variation $\Delta\varphi$ in one reciprocation is an integer multiple of 2π. This standing wave can stably exist and propagate through the optical fiber. However, Goos-Haenchen phenomenon occurs in the core-cladding interface with a propagation angle θ as shown in Fig. 2.2. When Goos-Haenchen shift equal to π, the propagation angle can be expressed as

$$\theta = \sin^{-1}\left(\frac{\pi(N+1)}{2ak}\right) \quad (N = 0,1,2,...) \tag{2.11}$$

where a is the radius of the core. Here, θ is a discrete value indicating that not all the lights can transmit through a fiber. Only the lights which satisfy the conditions of total internal reflection and noted above angle can stably exist in a fiber. According to Eq. 2.12, the phase profiles of lights are determined by N, resulting in specific propagation forms called propagation modes or guided modes. N is called mode number. SMFs typically have a fractional index difference between core and cladding of 0.3 percent, an NA of about 0.1, and a small core diameter of between 8 and 10 μm. Therefore, SMFs support only a single mode propagates in due to the sufficiently small core diameter and index difference. The condition for single mode propagation is that the normalized frequency V be less than 2.405, which expressed as

$$V = \frac{2\pi a}{\lambda}\sqrt{n_{core}^2 - n_{clad}^2} \tag{2.12}$$

where λ is the free space wavelength. The normalized frequency V can be used to calculate the number of modes supported and the cut-off wavelength. Current backbone optical networks are exclusively based on SMFs due to their advantages: the greatest transmission bandwidths, superior transmission quality over other fiber types, and the lowest losses, which are suitable for long-distance transmission. SI profile design is widely employed in SMFs. MMFs typically have a fractional index difference between core and cladding of between 1 and 1.5 percent, an NA in the range of 0.2 to 0.3, and a small core diameter of between 50 and 100 μm. MMFs support the propagation of many modes within one fiber core simultaneously and treat each mode as an independent optical path. Since the multiple modes enter the fiber core from different angles, their transmission paths and transmission time in the fiber are different. When the multiple modes arrive at the receiver, the pulse expansion (modal dispersion) will be generated. In MMFs based on SI design, modal dispersion may occur due to the different group velocities of the propagation modes. In MMFs based on GI design, the modal dispersion is far less due

to the refractive index profile. The rays transmitted close to the fiber axis have shorter paths when compared with rays that are transmitted into the outer regions of the core. However, due to the high-to-low index interfaces, the rays are transmitted through the central region with a lower velocity than that in the outer region, which compensates for the shorter path lengths and reduces dispersion in MMFs. For MMFs which support only a relatively small number of modes propagating within one core are called FMFs.

Figure 2.4 shows the classification of optical fibers. As noted above, the transmission capacity of SMFs is approaching its limit owing to nonlinear Shannon effects and the fiber fuse phenomenon. To meet the needs of a significantly increasing communication traffic, SDM as the preferred solution for network capacity growth is proposed and developed. FMFs, MCFs, and few-mode multi-core fibers (FM-MCFs) are three typical representatives. As a specific form of multiple SMF strands within a fiber cable, MCFs with multiple cores inside a single cladding have been widely studied. Further, FM-MCFs combined FMFs and MCFs enable a few modes to transmit in multi-core fibers, which have the potential to improve the fiber capacity drastically. MCFs can be divided into uncoupled MCFs and coupled MCFs [6-9]. Uncoupled MCF tends to have a thicker cladding to provide sufficient spacing between cores (over 30 μm). Thus, the light can propagate independently in each core with sufficiently low inter-core crosstalk. Although the uncoupled MCF is the most common MCF type with low-level crosstalk, it is essential to improve mechanical reliability with increasing multiplexity. Moreover, the large-scale multiplexing is difficult due to its structure. In the coupled MCF, several cores are placed close to be strongly/weakly coupled to each other and are able to be used as large-mode area (LMA) fibers. Thus, the coupled MCFs can provide higher spatial channel density than uncoupled MCF. However, coupled MCFs generally require a multiple-input-multiple-output (MIMO) processing to recover the original input signals from the output signals at the end of the transmission line [10].

Number of modes	Single-core	Multi-core	
		Uncoupled-type	Coupled-type
Single	SMF 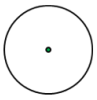	MCF 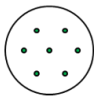	LMA fiber 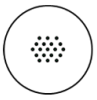
Few	FMF 	FM-MCF 	Strongly / Weakly coupling 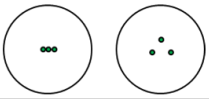
Multi	MMF 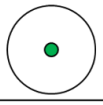	MM-MCF 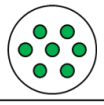	LMA fiber 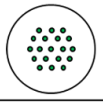

Figure 2.4. Classification of optical fibers.

2.2.2 Linearly polarized mode

In the above section, we know that only the lights which satisfy the conditions of total internal reflection and incident angle can exist stably and transmit through a fiber. According to wave optics, spatial mode refers to a specific solution of the wave equation that satisfies the appropriate boundary conditions from Maxwell's equations. By solving the wave equation, multiple true eigenmodes such as transverse-electric (TE) modes, transverse-magnetic (TM) modes, hybrid modes (EH or HE mode), can be obtained. Under the weakly guided approximation for the difference of refractive index between the core and cladding of fibers is extremely small <<1, the vectorial modes can be simplified using linearly polarized ($LP_{l,m}$) mode [11-14] which is presented by a linear combination of multiple true eigenmodes. The suffix l stands for the l-th order Bessel function which corresponds to the cutoff condition for the mode. The suffix m enumerates the successive zeroes of the corresponding Bessel function. The mode number N is expressed as

$$N = 2(m-1)+l \tag{2.13}$$

LP mode is easy to generate an ideal field distribution and is widely used as a practical mode pattern. In mode division multiplexing systems, GI-FMFs are usually used because they can suppress the mode dispersion. Thus, we take the GI-MMFs whose index profile α = 2 as an example to analyze the field distribution of LP modes. The core refractive index profile of the GI-MMF is expressed as

$$n(r) = n(0)\sqrt{1-2\Delta\left(\frac{r}{a}\right)^2} \qquad (r<a) \tag{2.14}$$

When the gradient of the dielectric constant is extremely small, the field distribution $\Psi_{l,m}$ of $LP_{l,m}$ mode in the cylindrical coordinate system is defined as

$$\Psi_{l.m}(\rho,\phi,z) = \rho^l \exp\left(-\frac{\rho^2}{2}\right) L_{m-1}^l(\rho^2)\cos(l\phi)\exp(-j\beta z), \tag{2.15}$$

where β is the propagation constant, and ρ is defined as standardized radial coordinate expressed as

$$\rho \equiv \frac{r}{a}\sqrt{V} \tag{2.16}$$

$L_n^k(x)$ is Bi-Laguerre polynomials and expressed as

$$L_n^k(x) = \sum_{s=0}^{n}(-1)^s \frac{(n+k)!}{s!(k+s)!(n-s)!}x^s \tag{2.17}$$

Since LP mode is orthogonal to each other according to Eq. 2.15, they are considered as the independent channels, and usually used in mode division multiplexing (MDM) technique. Figure 2.5 shows the intensity and phase distributions of several LP modes. It indicates that the intensity distribution of low-order mode is closer to the center and the intensity distribution of high-order mode is outer side. LP01 mode is the lowest order mode (fundamental mode) which is never cut-off and used in SMFs. In the situation of $l \geq 1$, LP mode can be regarded as $LP_{l,ma}$ and $LP_{l,mb}$ degenerate modes orthogonal to each other by rotation of the LP mode. Moreover, since the difference of propagation constant between modes is relatively small in GI-MMF, the mode group with the same mode number may be treated as pseudo degenerate modes even if the mode orders are different.

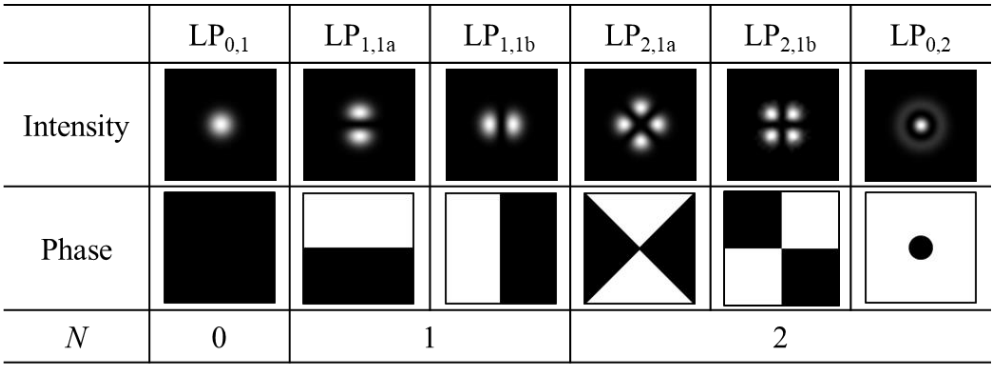

Figure 2.5. Intensity and phase distribution of LP modes.

2.3 MDM systems

MDM, as the primary technique for space-division multiplexing, has been investigated in several studies. In this section, MDM transmission systems will be introduced. The MDM transmission system consists of the transmitter which encodes messages into optical signals, the channel which carries the optical signals to its destination, and the receiver which decodes the messages from the received optical signals. Figure 2.6 shows the configuration of MDM transmission systems using FMFs. In the transmitter, the input signal is modulated by an electro-optical modulator with the form of a multi-level format for higher spectrum efficiency, such as polarization-division multiplexed quadrature PSK (PDM-QPSK) [15] and PDM-QAM [16]. It can convert the fundamental modes (LP01) emitted from SMFs into different higher-order modes and incident them into an FMF or MMF. Each signal is modulated in each mode treating as an independent transmission channel. Each signal is modulated in each mode treating as an independent transmission channel. Devices with such a function are called mode multiplexers (MUXs) [17-19]. In the receiver, multiple high-order modes emitted from the FMFs or MMFs can be converted into LP01 and incident into SMFs. This devices with such a function are called mode demultiplexers (DEMUXs) [20,21] which are the reverse process of MUXs due to the optical reversibility theorems. Generally, since each LP mode is orthogonal to the other, it can stably

transmit through fibers and does not mix with others. However, cross-talks (XTs) occur between multiple spatial modes within one core due to various factors such as structural defects during fiber manufacturing, misalignment of connection points, bending of the fiber, the diffident mode channel interference, and so on. Thus, MIMO digital signal processing (MIMO-DSP) [10,22,23] with low complexity is needed at the receiver side to recover the signals transmitted through the MMF. For an optical fiber with a multiplicity of m per core, $2m \times 2m$ MIMO processing is required. Since MIMO processing requires complex amplitude information of the light wave, the signal is detected by digital coherent detection that detects the phase information of the signal light by interference between the local light from the local oscillator and the signal light. On the other hand, to expand transmission capacity, more modes are expected to be used as transmission channels to carry signals. However, the different modes experience different propagation delays resulting in pulse dispersion. For SI fibers, the lowest dispersion per unit length is given approximately by

$$\frac{\delta\tau}{L} = \frac{n_{\text{core}}}{c}\Delta \tag{2.18}$$

where L is the fiber length, c is the transmission speed, and τ is the differential mode delay (DMD) defined as the relative group delay between the propagating modes. As a result, the pulse would broaden considerably at the end of the fiber due to τ is proportional to Δ. For GI fibers, this phenomenon can be reduced, and expressed as

$$\frac{\delta\tau}{L} = \frac{n_{\text{core}}}{10c}\Delta^2 \tag{2.19}$$

When the refractive index of the core is higher at the center and gradually decreases as the interface approaches, the fundamental mode will be total internal reflected near the center of the core, the higher-order modes will be total internal reflected near the core-cladding interface. Hence, all rays received together at the fiber output can be achieved if choosing the suitable refractive index distribution. However, it is difficult for GI fibers to completely reduce the DMD to zero. Although DMD can be compensated by the MIMO-DSP technique, the computation required to recover the signals at the receiver becomes more complex as the DMD between the propagation modes increases, which restricts the transmission distance. Moreover, the power consumption of the system also increases as the MIMO-DSP calculation increases. Thus, a reduction in DMD is essential to facilitate long-haul transmissions in MDM transmission systems. A scheme to reduce DMD using intermediate-mode interchange with low-crosstalk mode multiplexers (MUXs)/demultiplexers (DEMUXs) [24] has been reported. However, this scheme increases the system size owing to the requirement of two devices, a MUX and a DEMUX. Moreover, the increase in the number of multiplexed modes also increases the cost and size of the optical system. Thus, advanced mode conversion techniques which are independent of the number of multiplexity are essential to realize MDM systems in optical applications.

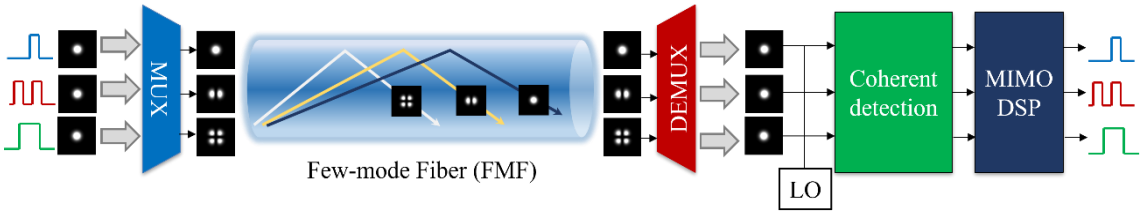

Figure 2.6. Configuration of FMF transmission system.

2.4 Mode conversion techniques

Mode conversion techniques are essential to connect different types of fibers in SDM transmission systems. Mode conversion techniques such as photonic lanterns, optical fiber couplers, waveguide-type using plane light wave circuit (PLC), and free-space optics using beam splitters and phase plates have been widely investigated. However, in the noted above mode conversion techniques, their scale of equipment and configuration complexity increase as multiplexity increases. Thus, advanced mode conversion techniques which are independent of the number of multiplexity are essential to realize SDM systems in optical applications. In this study, we propose two spatial mode conversion schemes: the spatial mode exchange technique using volume holograms for mode-to-mode conversion and the spatial-light-modulator-based optical-fiber joint switch for fiber-to-fiber conversion. The cost and size of the optical system are markedly lower because these schemes can convert all optical paths as a unit using a single optical component (VH or SLM), which is independent of the number of multiplexity. In this section, we will describe the primary principles and characteristics of the VH and SLM in detail.

2.4.1 Volume holography

The study of holography has led to applications in many optical areas. The holography is a technique that involves three-dimensional images using interference and diffraction. In holography, the interference patterns of two coherence light waves will be stored in the recording medium. Since the diffraction efficiency of VHs is affected by the thickness of the photosensitive material, we will first show the principle of holography and then make a brief introduction about photosensitive materials in this section.

(a) Principle of holography

Figure 2.7 shows the schematic diagrams of the holography. The scheme consists of recording and reconstruction procedures. During the recording procedure (Fig. 2.7(a)), the object beam is vertically incident on the recording medium and propagates along the z-axis. The reference beam makes an angle of θ to the z-axis. The object beam U_o and the reference beam U_r are both plane waves, and are expressed as

$$U_o(\boldsymbol{r}) = \sqrt{I_o}\exp(-j\boldsymbol{k}_o \cdot \boldsymbol{r}) \tag{2.20}$$

$$U_r(\boldsymbol{r}) = \sqrt{I_r}\exp(-j\boldsymbol{k}_r \cdot \boldsymbol{r}) \tag{2.21}$$

respectively, where I_o and I_r are the intensity distribution and $\boldsymbol{k}_o$ and $\boldsymbol{k}_r$ are the wavenumber vector of object beam and reference beam, respectively. $\boldsymbol{r}$ is the position vector. The interference fringes generated between the reference beam and object beam is given as

$$\begin{aligned} I(\boldsymbol{r}) &= |U_o + U_r|^2 \\ &= I_o + I_r + U_r^* U_o + U_r U_o^* \\ &= I_o + I_r + 2\sqrt{I_r}\sqrt{I_o}\cos(\boldsymbol{k}_g \cdot \boldsymbol{r}) \end{aligned} \tag{2.22}$$

where * denotes the conjugation, and $\boldsymbol{k}_g$ is the grating vector oriented perpendicular to the fringe planes, and is expressed as

$$\boldsymbol{k}_g = \boldsymbol{k}_o - \boldsymbol{k}_r \tag{2.23}$$

The three-dimensional volume hologram can be generated by the reaction in the recording medium according to the light intensity. The reaction according to the light intensity varies depending on the medium material, such as refractive index, transmittance, and polarization. According to Eq. 2.22, the modulation term that holds the complex amplitude of light wave is the third term. The period of the grating Λ (spatial frequency $f = 1 / \Lambda$) is expressed as

$$|\boldsymbol{k}_g| = \frac{2\pi}{\Lambda} \tag{2.24}$$

$$\Lambda = \frac{\lambda}{2\sin\theta} \tag{2.25}$$

A three-dimensional interference field with bright and dark fringes is formed in the recording medium, possessing complex amplitude information of both the object and reference beams. The complex amplitude transmittance T of volume holograms is expressed as

$$\begin{aligned} T(x, y, z) &= U_r^* U_o \\ &= \sqrt{I_r}\sqrt{I_o}\exp(-j\boldsymbol{k}_g \cdot \boldsymbol{r}) \end{aligned} \tag{2.26}$$

During the reconstruction procedure (Fig. 2.7(a)), the object beam can be reconstructed by irradiating the holograms with the reference beam. Difference from the planar hologram, the volume hologram has a three-dimensional diffraction grating in which the grating distribution is not only in the surface but in the depth direction. As shown in Fig. 2.8, when the optical path difference between the reflected beam from the front and back surface matches the integral multiplication of wavelength λ, the relation of incident angle and wavelength satisfies equation 2.25, which is called Bragg's condition. Only when the incident beam satisfies Bragg's condition, the diffracted beam can pass through the recording medium in the depth direction. Since the diffracted beam other than the first order diffracted beam does not satisfy Bragg's condition, they will sharply attenuate in the depth direction and is negligible. The diffracted beam U_d can be expressed as

$$\begin{aligned} U_d(x,y,z) &= T \times U_r \\ &= U_r^* U_o \times U_r \\ &= I_o \sqrt{I_r} \exp(-j\boldsymbol{k}_o \cdot \boldsymbol{r}) \end{aligned} \tag{2.27}$$

The diffracted beam possessing the complex amplitude of the object beam diffracts along with the direction of $\boldsymbol{k}_o$. Thus, the holography can reconstruct the beam recorded in the volume holograms without causing useless higher-order diffracted beams.

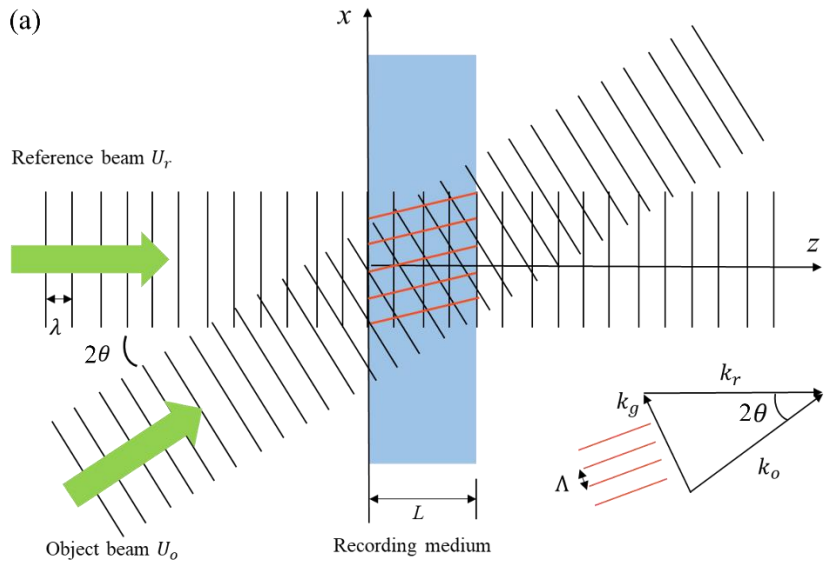

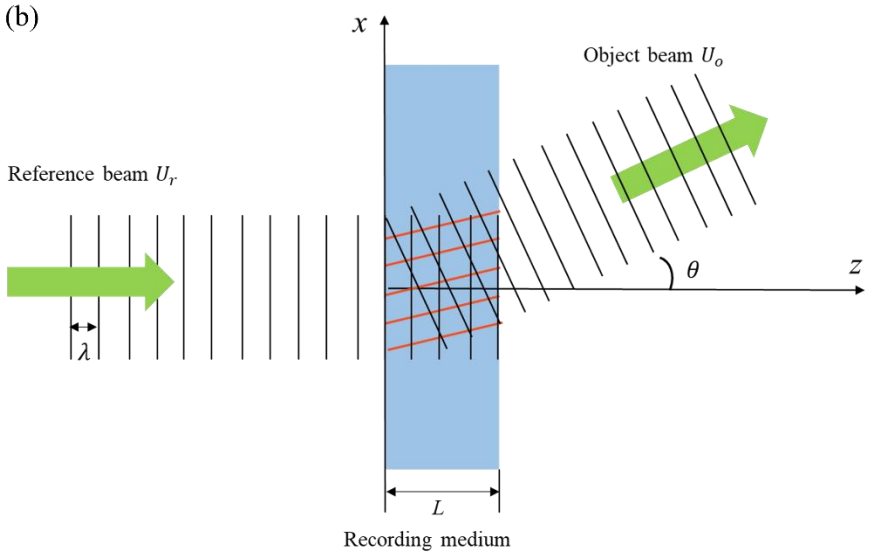

Figure 2.7. Model of volume hologram.

(a) Recording procedure. (b) Reconstruction procedure.

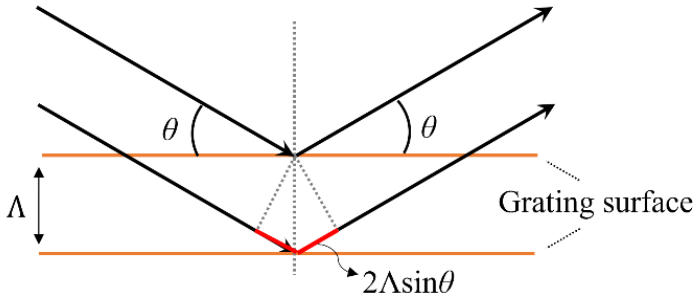

Figure 2.8. Diffraction corresponding to the Bragg condition.

(b) Diffraction efficiency

The diffraction efficiency of the holograms is defined that a periodic function of the index perturbation amplitude-thickness product. Holograms are typically classified to thin holograms where the thickness of the recording medium is much less than the spacing of the interference fringes, and thick holograms where the thickness of the recording medium is greater than the spacing of the interference fringes. The diffraction phenomenon of holography varies with the thickness of recording mediums. The hologram thickness index of holograms is called Klein-Cook parameter Q [25-27]

$$Q = \frac{2\pi\lambda L}{n\Lambda^2} \tag{2.28}$$

where L is the thickness of the grating, n is the spatially average refractive index of the recording medium, Λ is the grating period, and λ is the incident wavelength. For a thin hologram ($Q \leq 1$),

multiple-order diffraction occurs, which is called Raman-Nath diffraction. The medium disturbed by the light wave is similar to a plane phase grating. For a thick hologram ($Q \geq 10$), it corresponds to the Bragg diffraction, and only two diffraction orders (zeroth and first order) can be observed. The zeroth order diffraction beam corresponds to the reference information with a low diffraction efficiency, and the first order beam corresponds to the object information with a higher diffraction efficiency. For a transmission volume hologram, when incident angle satisfies the phase matching conditions, the relation between grating vector in *k*-space and the wavevectors of the readout light and the diffracted light (object light) are shown in Fig. 2.9. The circle radius is $|k| = 2\pi / \lambda$. This circle called Ewald sphere which is a geometric construction to demonstrate the relationship between the wavevector of the incident and diffracted beams, and the diffraction angle for a given reflection. The diffraction efficiency of fixed volume holograms has been adequately described by the coupled-wave theory of Kogelnik [28], and it is expressed as

$$\eta = \sin^2(\kappa L) \tag{2.29}$$

where κ is a constant proportional to the variety of the refractive index Δn, and is expressed as

$$\kappa = \frac{\pi \Delta n}{\lambda \cos\theta} \tag{2.30}$$

Considering the absorption coefficient α, diffraction efficiency is expressed as

$$\eta = \sin^2(\kappa L)\exp\left(-\frac{2\alpha L}{\cos\theta}\right) \tag{2.31}$$

It indicates that diffraction efficiency increases with the increasing thickness of the recording medium. Thus, the volume hologram can usually achieve a higher diffraction efficiency tan that of thin hologram. However, it is essential to balance the thickness and absorption coefficient due to the absorption loss is proportional to the thickness of the recording medium. On the other hand, if the Bragg condition is not satisfied, the triangle constructed by each wavevector does not close and creates a gap of Δk as shown in Fig. 2.10. The diffraction efficiency is approximated as

$$\eta = \kappa^2 L \mathrm{sinc}^2 \sqrt{\kappa^2 + (\Delta\kappa)^2 L} \tag{2.32}$$

It indicates that when the diffraction is not satisfied with the Bragg condition, the readout beam will attenuate rapidly in terms of the square of *sinc* function. Thus, the volume holograms have highly sensitive in wavelength and angle selectivity.

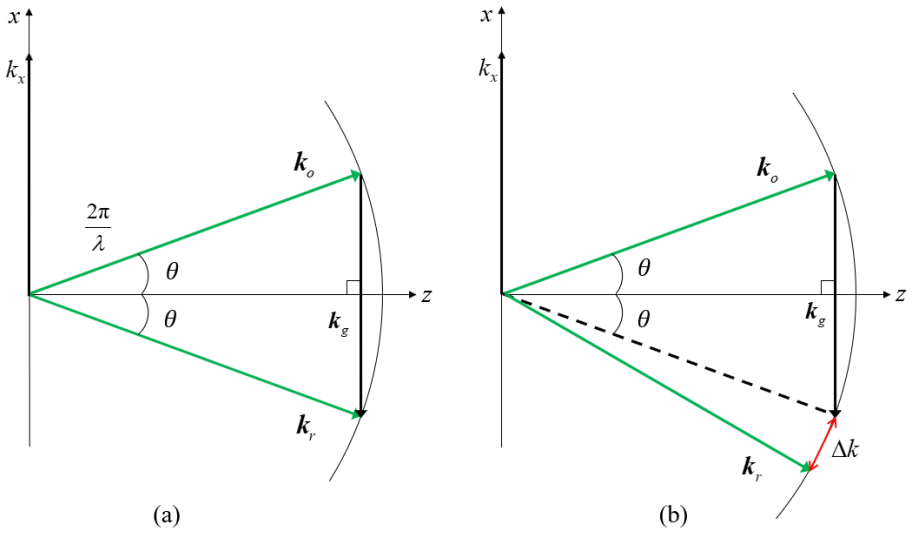

Figure 2.9. Ewald sphere of the relationship between wavevectors.
(a) satisfied Bragg's law. (b) unsatisfied Bragg's law.

(c) Photopolymer

The practical application of holography depends largely on the properties of recording materials. Generally, the recording medium should have good photosensitivity, flat spatial frequency responses, no absorption, no shrinkage, stability for long-term preservation, and so on. The recording materials have various types such as photographic emulsion [29], dichromate gelatin [30], photoresist [31], photorefractive [32], and photopolymer [33]. Among the above holographic materials, photopolymers are promising materials for use in holography due to their ease of preparation, high dynamic range, and self-processing. Moreover, their thick layers perform as a true volume material giving high diffraction efficiency and good angular selectivity. Therefore, the photopolymer is used in this study as a recording medium. The photopolymer is a polymer consisting of photopolymerizable monomers, non-photopolymerizable monomers (or binder polymers), matrixes, and photoinitiators. Their properties can be changed by heat treatment and exposure to light, usually in the ultraviolet or visible region of the electromagnetic spectrum. The photopolymerizable monomers can react and polymerize to light as a component for recording holograms. The non-photopolymerizable monomers diffuse into the non-irradiated region as photopolymerizable monomers are polymerized, causing a difference in the refractive index between them. It is expected that the difference in refractive index between the photopolymerizable monomers and non-photopolymerized monomers is as large as possible. The matrix can maintain the shape of the photopolymer and is desirable that the difference in the refractive index from photopolymerizable monomers is also large to promote the reaction.

Figure 2.10 shows the refractive index distribution process in photopolymer. When two coherent light waves irradiate the photopolymer, interference fringes are generated with alternately bright and

dark patterns, and the photoinitiators start to react by exposure to the interference fringes. Since there is a density difference between photopolymerizable monomers in the bright region and the dark region, photopolymerizable monomers will diffuse from the dark region to the bright region to keep the concentration gradient constant, and non-photopolymerizable monomers reverse. This causes an accelerated polymerization of photopolymerizable monomers in the bright regions. Then, the shapes of the polymerized polymers are maintained by matrixed and turn into a steady state. Under the circumstance, a refractive index difference is generated between the bright and dark regions of the interference fringes, and this refractive index distribution is used as a diffraction grating to record the holograms. This photopolymerization is a chemical reaction, and the bonding of molecules is difficult to break unless high-temperature heating or ultraviolet irradiation is performed; thus, it is stably maintained for a long period. However, many factors will deteriorate the performance of photopolymers, such as volume shrinkage during the photopolymerization reaction. When the volume shrinkage occurs, the period of the diffraction grating changes, resulting in a change in Bragg's condition. Therefore, even if irradiating the recorded photopolymer with the same reference information, Bragg's condition cannot be satisfied due to the phase mismatch. Recently, hologram materials with a shrinkage rate of less than 0.1% have been achieved by suppressing the additional amount of the photopolymerizable monomers or reducing the shrinkage of monomers themself. However, in this case, it has a tradeoff with the hologram recording capacity.

On the other hand, the refractive index saturates exponentially with respect to the amount of exposure on the photopolymer. When multiple holograms are recorded with the same exposure amount, the later recorded hologram exhibits lower diffraction efficiency. In order to ensure the diffraction efficiency is uniform for all holograms, it is necessary to gradually increase the exposure amount during the multiplex recording procedure [34]. As noted above, it is assumed that polymerization responded instantaneously to changes in light intensity, resulting in an instantaneous cessation of polymerization when the exposure is stopped. However, it has been widely noted that under certain conditions, post-exposure grating magnification can be observed, which is referred to as "dark reactions" or "post-exposure growth". Using these latest materials [35], the refractive index distribution can be formed uniformly by a post-exposure process using an incoherent light source after all the recording procedures are performed.

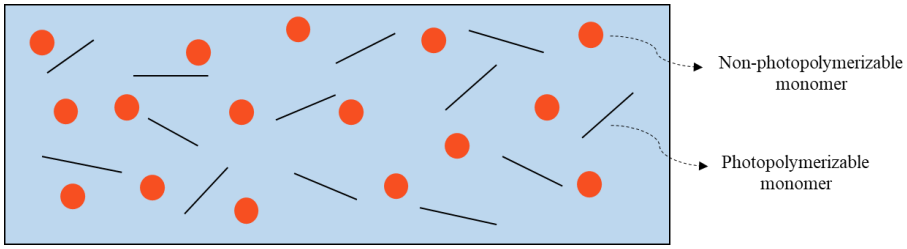

(a) Before light exposure.

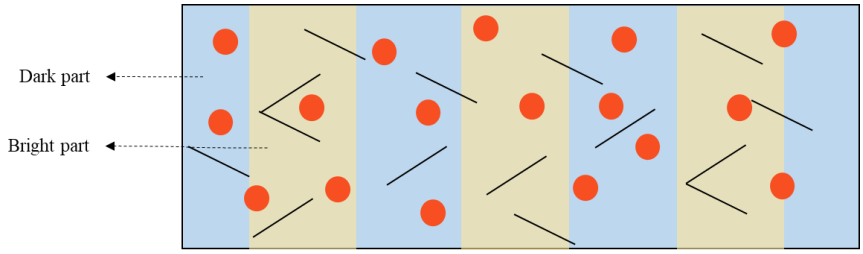

(b) During light exposure.

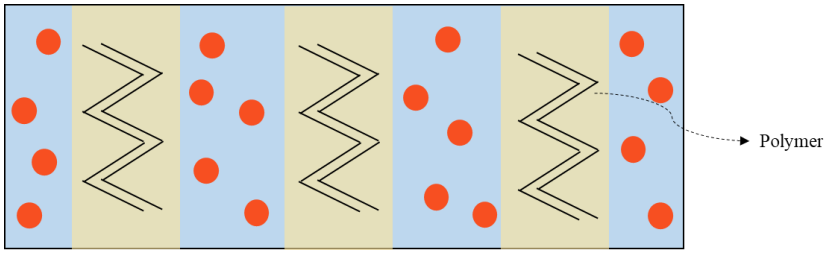

(c) Steady state.

Figure 2.10. Formation process of refractive index distribution.

2.4.2 Spatial light modulator

Micro-display performance has been widely investigated due to its fabrication of small display pixels and high-resolution arrays of pixels. Spatial light modulators (SLMs) are well-established micro-display devices that allow for the modulation of the amplitude, phase, and polarization of light waves according to the two dimensions (2D) of the modulator [36-39]. Based on the modulation method, SLMs can be classified as phase-only, amplitude-only, polarization, or a combination of phase-amplitude modulation. On the other hand, different from the spatial light modulators such as segmented or thermally deformable mirrors, liquid crystals (LCs), organic materials with extraordinary electro-optical properties, are widely used in optics. Liquid crystal on silicon (LCoS) is the most attractive reflective micro-display technology for all sorts of SLM applications as optical storage, diffractive optics, reconfigurable interconnects, and wave shaper technology, due to their high mobility so that the pixel size can be made small (< 10 μm) and has a high aperture ratio (> 90 percent). Since the extraordinary properties of LCoS-SLMs, we propose a mode conversion technique using a

phase-only LCoS-SLM to switch all the spatial paths of an FM-MCF as a unit to a specific direction. Subsequently, we will introduce the principle and configuration of the LCoS-SLMs in detail.

Figure 2.11 shows the schematic diagram of the LCoS-SLM. The phase of input light can be modulated by the LCoS in which nematic liquid crystals are enclosed between a transparent electrode deposited on a glass substrate and a matrix of the complementary metal oxide semiconductor (CMOS). The digital signals output from the computer is converted to analog signals by a dedicated drive circuit, and voltage is applied to the pixel electrodes on the CMOS. The LC molecules of each pixel rotate according to the applied voltage; the higher voltage leads to a larger rotation. Thus, the orientation of LC molecules and the refractive index of LCs can be modulated by the applied voltage. Since LCs is a birefringent material, the alignment of the LC molecules can in turn control the phase shift of each pixel. Thus, if a linearly polarized light incident to the LCoS display and aligned to the long axis of the LC, SLM will act as a phase modulator. The length of the optical path will be changed by the refractive index. Figure 2.12 show the 2D pixelated SLM geometry. The spatial resolution is an importance parameter to determine the smallest resolvable diffracted angle, which is related to the pixel size and pixel pitch. A higher pixel density of LCoS is typically 1920 × 1080 pixels. However, the modulated optical property of SLM is discontinuous due to the pixel gaps between two adjacent segments. Inactive gaps are responsible for light scattering. This feature is defined as the fill factor (FF) or aperture ratio, which is approximately as

$$FF = \frac{\text{pixel size} \times \text{pixel size}}{\text{pixel pitch} \times \text{pixel pitch}} \tag{2.33}$$

The fill factor is usually above 90% for commercial systems which the gaps between pixels is about 0.2 μm. Here, LCoS displays have the same properties to the thin holograms. When the light incident to the LCoS display, the light may be diffracted into higher orders due to the grating like structure of the pixel matrix. Thus, the diffraction efficiency is not 100%, and is typically between 70% and 90%. On the other hand, the imperfection hologram generated on the LCoS due to the phase flicker [40] and fringing field effect [41] will cause device-level crosstalk in SLMs.

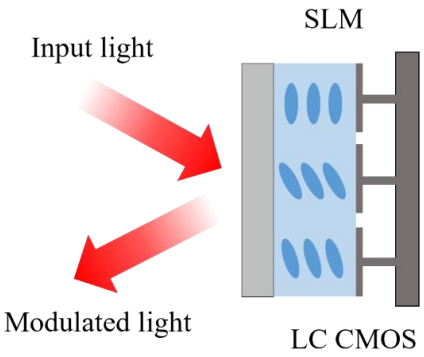

Figure 2.11. Schematic diagram of the LCoS-SLM.

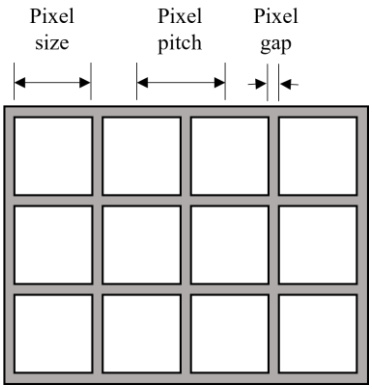

Figure 2.12. Two-dimensional pixelated SLM geometry.

2.5 Summary

In this chapter, we introduced the configuration and key technologies of SDM transmission systems. The structure and classification of the optical fibers were introduced firstly. Based on the number of modes supported, the optical fibers can be classified as SMFs, FMFs or MMFs. SDM technologies includes two approaches: mode division multiplexing using FMFs or MMFs, and core multiplexing using MCFs, treating each core/mode as an independent optical path. Thus, in SDM systems, mode conversion techniques are essential to connect different types of fibers in SDM transmission systems. The volume holograms and spatial light modulators as the key components used for the mode conversion were introduced in detail. Due to the practical application of holography depends largely on the properties of recording materials, photopolymers were chosen as the recording medium in our study due to their ease of preparation, high dynamic range, and self-processing. On the other hand, LCoS-SLMs, the reflective micro-display technology, were chosen for the mode conversion in FM-MCFs due to the high spatial resolution, high light efficiency, and quick response.

References

[1] M. Secondini and E. Forestieri, “The limits of the nonlinear Shannon limit,” Proc. Optical Fiber Communication Conf. (OFC), 2016, Th3D.1.

[2] S. Todoroki, “Transient propagation mode of fiber fuse leaving no voids,” Opt. Express **13**(23), 9248-9256 (2005).

[3] C. E. Shannon, “A Mathematical Theory of Communication,” Bell Syst. Tech. J. **27**, 379-423 (1948).

[4] J. Crisp and B. Elliott, “Introduction to fiber optics (3rd edition),” Elsevier publisher, 2005.

[5] I. Jacobs, “Optical fiber communication technology and system overview,” Handbook of optics (3rd edition), Volume V: Atmospheric optics, modulators, fiber optics, X-ray and neutron optics, edited by M. Bass, C. MacDonald, G. Li, C. M. DeCusatis and V. H. Mahajan, McGraw-Hill publisher, 2005.

[6] K. Saitoh and S. Matsuo, “Multicore fibers for large capacity transmission,” Nanophotonics **2**(5-6),

441-454 (2013).

[7] K. Saitoh and S. Matsuo, "Multicore fibers technology," J. Light. Technol. **34**(1), 55-66 (2016).

[8] T. Hayashi, Y. Tamura, T. Hasegawa, T. Nakanishi, and T. Taru, "Coupled multi-core optical fiber suitable for long-haul transmission," Sei Technical review **85**, 19-23 (2017).

[9] R. M. Kingsta and R. S. Selvakumari, "A review on coupled and uncoupled multicore fibers for future ultra-high capacity optical communication," Optik-International journal for light and electron optics 199, 163341 (2019).

[10] T. Sakamoto, T. Mori, M. Wada, T. Yamamoto, F. Yamamoto, and K. Nakajima, "Strongly-coupled multi-core fiber and its optical characteristics for MIMO transmission systems," Opt. Fiber Technol. **35**, 8-18 (2017).

[11] D. Gloge, "Weakly guiding fibers," Appl. Opt. **10**(10), 2252 (1971).

[12] S. Pillay, D. Kumar, and H. A. A-Rashid, "Weakly guiding fibers and LP modes in circular and elliptical waveguides," Journal of electromagnetic analysis and applications **5**(8), 333-335 (2013).

[13] J. Qian and W. Huang, "LP modes and ideal modes on optical fiber", J. Light. Technol. **4**(6), 626-630 (1986).

[14] T. Yamaguchi, S. Miura, and Y. Kokubun, "Demonstration of true-eigenmode propagation in few-mode fibers by selective LP mode excitation and near-field observation," IEICE Electron. Expr. **15**(10), 1-12 (2018).

[15] S. Chandrasekhar, A.H. Gnauck, X. Liu, P. J. Winzer, Y. Pan, E. C. Burrows, B. Zhu, T. F. Taunay, M. Fishteyn, M. F. Yan, J. M. Fini, E. M. Monberg, and F. V. Dimarcello, "WDM/SDM transmission of 10 × 128-Gb/s PDM-QPSK over 2688-km 7-core fiber with a per-fiber net aggregate spectral-efficiency distance product of 40,320 kmb/s/Hz," 37th European Conference and Exhibition on Optical Communication, Geneva, Th.13.C4 (2011).

[16] H. Hu, M. P. Yankov, F. D. Ros, Y. Amma, Y. Sasaki, T. Mizuno, Y. Miyamoto, M. Galili, S. Forchhammer, L. K. Oxenlowe, and T. Morioka, "Ultrahigh-spectral-efficiency WDM/SDM transmission using PDM-1024-QAM probabilistic shaping with adaptive rate," J. Light. Technol. **36**(6), 1304-1308 (2018).

[17] K. Igarashi, D. Soma, K. Takeshima, and T. Tsuritani, "Selective mode multiplexer based on phase plates and Mach-Zehnder interferometer with image inversion function," Opt. Express **23**(1), 183-194 (2015).

[18] G. Labroille, B. Denolle, P. Jian, P. Genevaux, N. Treps, and J. F. Morizur, "Efficient and mode selective spatial mode multiplexer based on multi-plane light conversion," Opt. Express **22**(13), 15599-15607 (2014).

[19] N. Fontaine, R. Ryf, H. Chen, D. Neilson, and J. Carpenter, "Design of high order mode-multiplexers using multiplane light conversion," European Conference on Optical Communication (ECOC), Tu.1.F.4 (2017).

[20] Y. Wakayama, A. Okamoto, K. Kawabata, A. Tomita, and K. Sato, "Mode demultiplexer using angularly multiplexed volume holograms," Opt. Express **21**(10), 12920-12933 (2013).

[21] K. Aoki, A. Okamoto, Y. Wakayama, A. Tomita, and S. Honma, "Selective multimode excitation using volume holographic mode multiplexer," Opt. Lett. **38**(5), 769-771 (2013).

[22] T. Sakamoto, T. Mori, T. Yamamoto, and S. Tomita, "Differential mode delay managed transmission line for wide-band WDM-MIMO system using multi-step index fiber," J. Light. Technol. **30**(17), 2783-2787 (2012).

[23] D. Soma, Y. Wakayama, K. Igarashi, and T. Tsuritani, "Partial MIMO-based 10-Mode-multiplexed transmission over 81km weakly-coupled few-mode fiber," Optical Fiber Communications Conference (OFC), M2D.4 (2017).

[24] Y. Wakayama, D. Soma, K. Igarashi, H. Taga, and T. Tsuritani, "Intermediate mode interchange for reduction of differential mode-group delay in weakly-coupled 6-mode fiber transmission line," Proc. OFC2016, M3E.6 (2016).

[25] W. R. Klein and B. D. Cook, "Unified Approach to Ultrasonic Light Diffraction," IEEE Transactions on Sonics and Ultrasonics **14**(3), 123-134 (1967).

[26] J. Gao, G. Han, and J. Zhu, "Research on the characteristics of Klein–Cook parameter and diffraction efficiency of acousto-optic interaction for low-frequency ultrasonic in the liquid," Opt. Appl. **LI**(3), 445-456 (2021).

[27] Y. J. Liu and X. W. Sun, "Holographic polymer-dispersed liquid crystals: materials, formation, and applications," Advances in OptoElectronics 2008, 684349 (2008).

[28] H. Kogelnik "Coupled Wave Theory for Thick Hologram Gratings", Bell Syst. Tech. J. **48**(9), 2909-2947 (1969).

[29] J. M. Kim, B. S. Choi, U. I. Kim, J. M. Kim, H. I. Bjelkhagen, and N. J. Phillips "Holographic optical elements recorded in silver halide sensitized gelatin emulsions. Part I. Transmission holographic optical elements," Appl. Opt. **40**(5), 622-632 (2001).

[30] T. Kubota and T. Ose, "Lippmann color holograms recorded in methylene-blue-sensitized dichromated gelatin," Opt. Lett. **4**(9), 289-291 (1979).

[31] F. H. Dill, W. P. Hornberger, P. S. Hauge and J. M. Shaw, "Characterization of positive photoresist," IEEE Transactions on Electron Devices **22**(7), 445-452 (1975).

[32] K. Meerholz, B. L. Volodin, Sandalphon, B. Kippelen, and N. Peyghambarian, "A photorefractive polymer with high optical gain and diffraction efficiency near 100%," Nature **371**, 497-500 (1994).

[33] J. R. Lawrence, F. T. O'Neill and J. T. Sheridan, "Photopolymer holographic recording material," Optik-International journal for light and electron optics **112**(10), 449-463 (2001).

[34] A. Pu, K. Curtis, and D. Psaltis, "Exposure schedule for multiplexing holograms in photopolymer films," Opt. Eng. **35**(10), 2824-2829 (1996).

[35] M. R. Gleeson, J. Guo, and J. T. Sheridan, "Optimisation of photopolymers for holographic

applications using the Non-local Photo-polymerization Driven Diffusion model," Opt. Express **19**(23), 22423-22436 (2011).

[36] A. Jullien, "Spatial light modulators," Photoniques **101**, 59-64 (2020).

[37] W. P. Bleha, L. Juan and A. Lei, "Advances in liquid crystal on silicon (LCOS) spatial light modulator technology," Proc. of SPIE 8736, 87360A (2013).

[38] N. Collings, T. Davey, J. Christmas, and B. Crossland, "The applications and technology of phase-only liquid crystal on silicon devices," J. Disp. Technol. **7**(3), 112-119 (2011).

[39] M. Wang, L. Zong, L. Mao, A. Marquez, Y. Ye, H. Zhao, and F. J. V. Caballero, "LCoS SLM study and its application in wavelength selective switch," Photonics **4**(2), 22 (2017).

[40] H. Yang and D. P. Chu, "Phase flicker in liquid crystal on silicon devices," J. Phys. Photonics **2**(3), 1-19 (2020).

[41] U. Efron, B. Apter, and E. B. Treidel, "Fringing-field effect in liquid-crystal beam-steering devices: an approximate analytical model," J. Opt. Soc. Am. A **21**(10), 1996-2008 (2004).

Chapter 3

Spatial Mode Exchange Technique Using Volume Holograms

3.1 Introduction

In mode-division multiplexing systems [1-3], its transmission quality is restricted by differential mode delay (DMD) [4], which is defined as the relative group delay between the propagating modes. This delay is related to the computational cost of the multiple-input/multiple-output digital signal processing (MIMO-DSP). In MIMO-DSP, the computation required to recover the signals at the receiver becomes more complex as the DMD between the propagation modes increases, which restricts the transmission distance [5]. Moreover, the power consumption of the system also increases as the MIMO-DSP calculation increases. Thus, a reduction in DMD is essential to facilitate long-haul transmissions in MDM transmission systems. A scheme to reduce DMD using intermediate-mode interchange with low-crosstalk mode multiplexers (MUXs)/demultiplexers (DEMUXs) [6] has been reported. However, this scheme increases the system size owing to the requirement of two devices, a MUX and a DEMUX. Moreover, the increase in the number of multiplexed modes also increases the cost and size of the optical system. Therefore, to miniaturize the optical system and to reduce the cost, the mode exchanger can be downsized to implement a simpler structure. In this chapter, we propose a spatial mode exchange technique using volume holograms (VHET) to reduce DMD. The cost and size of the optical system are markedly lower because this scheme requires only a single holographic medium, which is independent of the number of multiplexed modes. Moreover, the VHET is able to perform mode exchanging in the optical transmission bands by using dual-wavelength method [7,8].

To confirm the feasibility of the proposed method, in Section 3.2, we demonstrate its operating principle. In Section 3.3, we perform numerical simulations to model the exchanges within a linearly polarized (LP) mode group. In Section 3.4, we present an experiment on exchanging using three LP modes. In Section 3.5, application on optical communication wavelength bands using dual-wavelength method is demonstrated. In Section 5.6, the research results and prospects of this work are summarized and discussed.

3.2 Operational principle of VHET

VHET utilizes multiplexed volume holograms to exchange multiplexed spatial modes simultaneously. The multiplexed volume holograms are recorded as fringes resulting from the interference between the object beam and the reference beam, and the object beam is then reconstructed by irradiating the holograms with the reference beam. Thus, by using an object beam consisting of multiple spatial modes to read the holograms, the reference beam consisting of the desired spatial modes is reconstructed. Using this method, VHET can reduce the DMD by exchanging multiple spatial modes with different transmission speeds in an FMF using a volume hologram. The cost and size of the optical system are markedly lower because this scheme requires only a single holographic medium, which is independent of the number of multiplexed modes.

Figure 3.1 shows a conceptual model of a two-mode MDM transmission system combined with VHET. We assume that the difference in the signal path lengths between the two modes is negligible. The signal beams comprising LP01 and LP11 propagate through a 1-km FMF, and the undergo times are τ_1 and τ_2, respectively. When $\tau_1<\tau_2$, we define DMD as $\tau_2-\tau_1$. If the signal beams propagate in the second 1-km FMF without mode exchange, the DMD will become $2(\tau_2-\tau_1)$. As shown in the Fig. 3.2, DMD can be compensated by VHET at the relay point between the two FMFs because both modes experience the same time of $\tau_1+\tau_2$. The DMD will become zero and the impulse responses of the modes will overlap at P_{mid} if the modes propagate through the fiber without crosstalk.

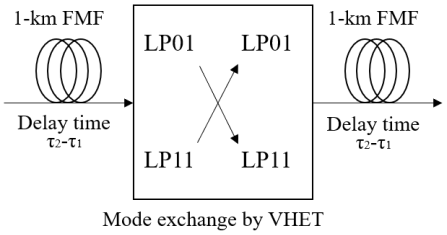

Figure 3.1. 2-km MDM system combined with VHET.

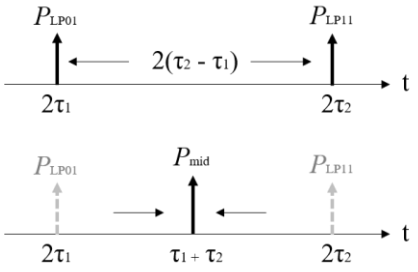

Figure 3.2. Impulse responses with mode exchange.

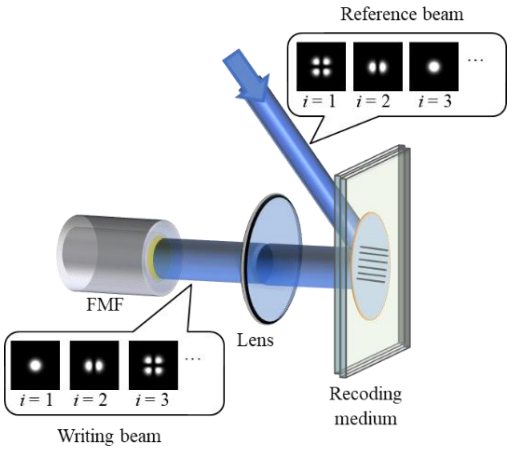

(a)

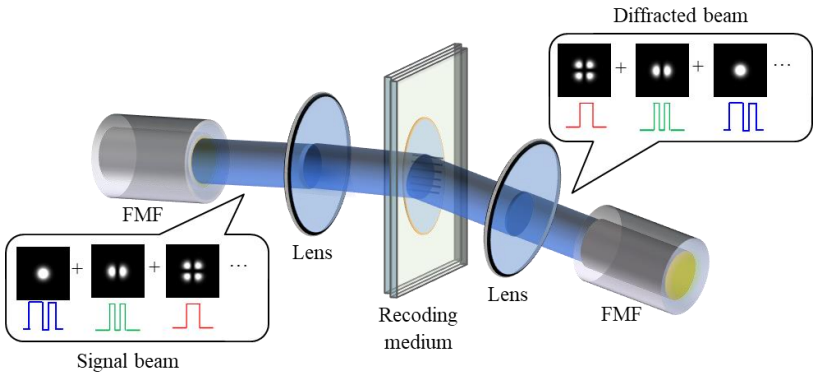

(b)

Figure 3.3. Schematic diagram of the proposed method. (a) Recording procedure. Writing beams are incident on a recording medium sequentially with reference beams to record holograms. (b) Exchange procedure. By irradiating the MDM signal beams to the holograms, each mode component is diffracted simultaneously at the incident angle of the reference beam.

Figure 3.3 shows schematic diagrams of the VHET. VHET utilizes volume holograms consisting of interference fringes between the writing beams (object targets) and reference beams (exchange targets) to facilitate the exchange of multiple spatial modes with different transmission speeds. By irradiating the holograms with MDM signal beams (object targets), the spatial mode components are diffracted with complex amplitude distributions corresponding to those of the reference beams (exchange targets). Based on the above description, the principle of the proposed method is explained as follows.

The scheme consists of recording and exchange procedures. During the recording procedure (Fig. 3.3(a)), the writing beam W_i (i = 1, 2, …, m) and reference beam R_i, which are generated by a complex amplitude generator, such as a spatial light modulator (SLM), possess a complex amplitude

distribution of the spatial modes. The writing beam W_i and reference beam R_{m-i+1} are combined according to the modal delay time. Here, the writing beam is vertically incident on the recording medium and propagates along the *z*-axis. The reference beam forms an angle θ with the *z*-axis. Thus, for the i^{th} hologram, W_i and R_{m-i+1} are expressed as follows:

$$W_i = A_i(x, y, z)\exp[jkz + j\varphi_i(x, y, z)] \tag{3.1}$$

$$R_{m-i+1} = A_r(x, y, z)\exp[jk(x\sin\theta + z\cos\theta) + j\varphi_r(x, y, z)] \tag{3.2}$$

where A_i (x, y, z) and A_r (x, y, z) are the amplitudes and φ_i (x, y, z) and φ_r (x, y, z) are the phase distributions of the writing and reference beams, respectively; k is the wave number in the recording medium. The complex amplitude transmittance T (x, y, z) of the recorded holograms of the writing beam and reference beam is expressed as follows:

$$\begin{aligned} T(x, y, z) = \sum_{i=1}^{N} A_r(x, y, z)A_i^*(x, y, z)\exp[j(\varphi_r(x, y, z) - \varphi_i(x, y, z)) \\ + jkx\sin\theta + jkz(\cos\theta - 1)] \end{aligned} \tag{3.3}$$

where * denotes a complex conjugate.

During the exchange procedure (Fig. 3.3(b)), the MDM signal beam *S*, which consists of spatial modes corresponding to the writing beam, is collimated in the same manner as the recording procedure. The MDM signal is expressed as follows:

$$S = \sum_{n=1}^{M} a_n(t)A_n(x, y, z)\exp[jkz + j\varphi_n(x, y, z)] \tag{3.4}$$

where A_n and φ_n $(n = 1, 2, \ldots, m)$ are the amplitude and phase distribution of the signal beam, respectively. When the MDM signal beam irradiates the multiplexed volume holograms, the spatial mode components are diffracted as

$$\begin{aligned} D &= \eta\int_0^L TS\,dz \\ &= \eta\sum_{n=1}^{m}\sum_{i=1}^{m}\int_0^L a_n(t)A_nA_i^*A_r(x, y, z)\exp\left[j\left(\varphi_n - \varphi_i + \varphi_r\right) + jk\left(x\sin\theta + z\cos\theta\right)\right]dz, \end{aligned} \tag{3.5}$$

where L is the thickness of the recording medium, η is the diffraction efficiency, and $a_n(t)$ is the time series signal. When $n = i$, the spatial mode component is converted to a beam, of which, the spatial phase corresponds to that of the reference beam and is strongly diffracted in the direction of θ. When $n \neq i$, the mode fields between the writing beams and MDM signals are mismatched, and the spatial mode components are weakly diffracted as crosstalk components. It is noticed that for the general volume holography, we usually define all components, except the signal, as the crosstalk components [9-11]. However, in the MDM transmission system, although the spatial modes other than those used for multiplex recording are generated by the multiplexed hologram, only the crosstalk components

from the spatial modes that need to be coupled to the next FMF are considered. For example, we consider an exchange behavior between the three modes. If we assume that there are three modes as signals that need to be coupled to the next FMF, we only need to consider the crosstalk components between these three modes. If we assume that there are six modes as signals that need to be coupled to the next FMF, we need to consider the crosstalk components between these six modes. Thus, of all the crosstalk components generated by the hologram, only the modal components that can be coupled to the FMF remain as crosstalk. Consequently, the diffracted beam D is expressed as follows:

$$D=\eta\sum_{n=1}^{m}a_n(t)\int_0^L\left|A_n\right|^2 A_r\exp\left[\,j\varphi_r+jk\left(x\sin\theta+z\cos\theta\right)\right]dz \tag{3.6}$$

The spatial mode components of the signal beams are diffracted simultaneously at the incident angle of the reference beam. The diffracted beam is shaped to fit the complex amplitude distributions corresponding to those of the reference beam by using a lens. By this way, the multiple spatial modes with difference transmission speeds are exchanged simultaneously by using only a single optical element. Besides, VHET as a free-space optics technique, it would not need any extra optical element. Thus, the optical system can be miniaturized, and the cost can be suppressed.

3.3 Numerical simulation

3.3.1 Simulation model

To validate the basic operation of the proposed scheme, we performed a numerical simulation to model the exchanges within an LP mode group comprising of LP01, LP11, and LP21. The simulation parameters are presented in Table 3.1. We assumed that the wavelength of the light source is 1550 nm. The recording medium was a photopolymer with a thickness of 150 μm, and the incident angle θ was set to 6°. The models and flow of the simulations are shown in Fig. 3.4. During the recording procedure (Fig. 3.4(a)), the complex amplitudes of the spatial modes are generated as the writing beam and reference beam with an oblique phase corresponding to the incident angle θ in the Fourier space, and the complex amplitudes on the back surface of the recording medium were then calculated by FFT. Subsequently, the complex amplitudes of the spatial modes on the front surface of the recording medium were acquired using an antidromic angular spectrum method (ASM) [12]. We calculated the refractive index distribution of each layer induced by the interference fringe profile in the photopolymer using the FFT beam propagation method (FFT-BPM) [13]. This process was performed for the number of modes m, and the refractive index distribution in the photopolymer was obtained by m multiple recordings. During the exchange procedure (Fig. 3.4(b)), the intensity distribution of the MDM signals, which is consistent with the writing beams, are generated and collimated by FFT. The complex amplitude of the diffracted beam was then acquired in the same manner as the recording

procedure. Subsequently, the complex amplitude of the diffracted beam received on the FMF plane was calculated by FFT.

We assume that the delay time in a 1-km FMF of LP11-LP01 is -0.2 ns and that for LP21-LP01 is -1.8 ns [6]; thus, the DMD of three modes is 1.8 ns. If the spatial modes propagate in the second 1-km FMF without mode exchange, the DMD will become 3.6 ns. Here, we exchange LP01 and LP21 to compensate for the difference in the transmission speeds. LP11 does not change. Thus, in this simulation, LP01, LP11, and LP21 were changed to LP21, LP11, and LP01, respectively. DMD can ideally be compensated to 1.4 ns with mode exchange at the relay point between the two FMFs, as shown in Fig. 3.5. As observed, there is an overlap between the lines of the signal component of LP11 with and without mode exchange.

Here, crosstalk generally exists during the exchange procedure. The i^{th} (i = 1,2,3) spatial mode of the diffracted beam is reconstructed by irradiating the multiplexed holograms with the n^{th} (n = 1,2,3) mode of MDM signals denoted as $D_{n,i}$. The spatial mode component corresponds to the reference beam as a signal component, and the other diffracted components correspond as crosstalk. The signal component governs the situation in which $n = i$. We evaluated the exchange accuracy by calculating the coupling efficiency (CE) between each complex amplitude of the diffracted beam obtained and the complex amplitude of the desired ideal mode. The CE of $D_{n,i}$ is denoted as $\mathrm{CE}_{n,i}$, and it is calculated by:

$$CE_{n,i} = \left| \iint E_{n,i}^{*}(x,y) E_{id}(x,y) dxdy \right|^2 \tag{3.7}$$

where * denotes a complex conjugate. Note that $E_{n,i}^{*}(x,y)$ and $E_{id}(x,y)$ are the complex amplitude distributions of the n^{th} diffracted mode and the ideal desired mode, respectively. The crosstalk from the n^{th} mode to the i^{th} mode is denoted as $\mathrm{XT}_{i,n}$, and it is calculated as:

$$\mathrm{XT}_{i,n} = 10\log_{10}\left(\frac{CE_{n,i}}{CE_{n,n}}\right) \quad (n \neq i) \tag{3.8}$$

where $\mathrm{CE}_{n,i}$ is the coupling efficiency between the ideal mode and diffracted mode of the noise components, and $\mathrm{CE}_{n,n}$ is the signal component.

Table 3.1. Simulation parameters of VHET.

Common parameters			
Wavelength of beam source	1550 nm	Average refractive index	1.5
Incident angle of reference beam	6°	Pixel number	1024 × 1024
Thickness of photopolymer	150 μm	Pitch of data pixel	0.5 × 0.5 μm
Focal length of Fourier transform lens	150 mm	Pitch of z-direction, Δz	1.0 μm
Exposure time	0.1 s	Over sampling rate	2

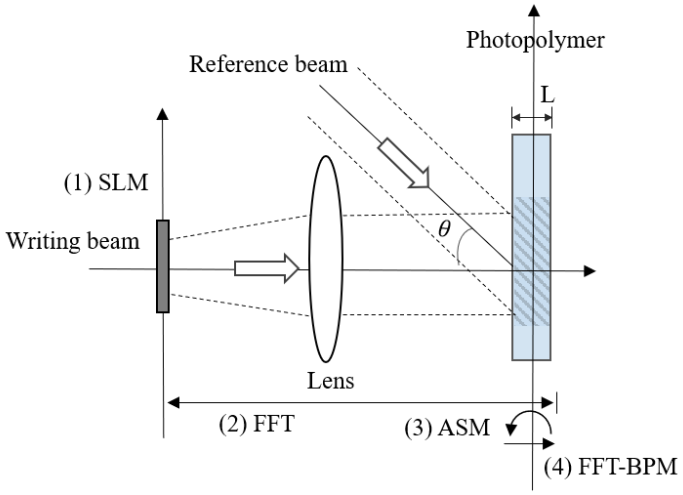

(a)

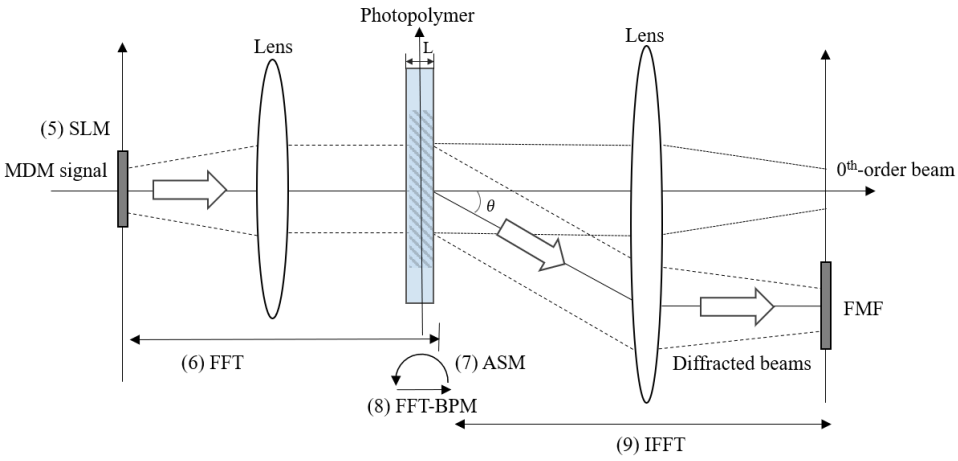

(b)

Figure 3.4. Simulation models. (a) Recording procedure. (b) Exchange procedure. Overviews of each process are as follows. (1), (5): Set complex amplitude(s) of each mode. (2), (6): Calculate complex amplitude(s) on the back surface of the photopolymer using FFT. (3), (7): Calculate complex amplitude(s) on the front surface of the photopolymer using the free-space transfer function. (4), (8): Calculate complex amplitude(s) of the inside of the photopolymer using FFT-BPM. (9): Calculate final result on FMF plane using FFT. Processes (1)–(4) and (5)–(9) are repeated for each mode.

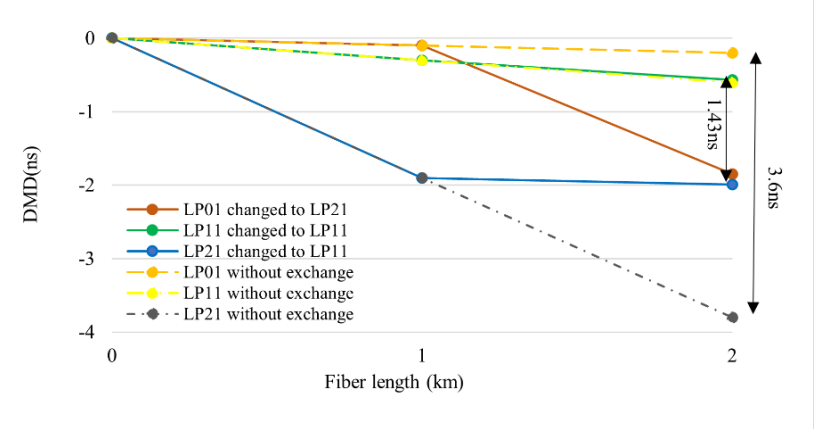

Figure 3.5. DMD with mode exchange at relay point.

3.3.2 Simulation results and discussion

We assume that the delay time in 1-km FMF of LP11-LP01 is -0.2 ns, LP21-LP01 is -1.8 ns, and the DMD of three modes is 1.8 ns. To verify the principle of VHET, we performed a numerical simulation between LP01, LP11, and LP21. We assume that only three spatial modes, LP01, LP11, and LP21, can be coupled to the second FMF. As mentioned above, of all the crosstalk components generated by the hologram, only the modal components that can be coupled to the FMF remain as crosstalk. Thus, only the crosstalk components between LP01, LP11, and LP21 were considered. As shown in Table 3.2, y_1, y_2, and y_3 indicate the components of diffracted beam that LP21 converted to LP01, LP11 converted to LP11, and LP01 converted to LP21, respectively. In the conversion of LP21 to LP01, upon irradiating the multiplexed holograms by LP21, the components LP01, LP11, and LP21 are generated simultaneously. LP01 is regarded as the signal, and LP11 and LP21 are considered as the crosstalk components. In the conversion of LP11 to LP11, LP11 is regarded as the signal, and LP01 and LP21 are considered as the crosstalk components. In the conversion of LP01 to LP21, LP21 is regarded as the signal, and LP01 and LP11 are generated as crosstalk components. Therefore, y_i (i = 1,2,3) can be described as [5]

$$y_1 = a_1 x_1(\tau_1) + b_1 x_2(\tau_2) + c_1 x_3(\tau_3), \tag{3.9}$$

$$y_2 = a_2 x_1(\tau_1) + b_2 x_2(\tau_2) + c_2 x_3(\tau_3), \tag{3.10}$$

$$y_3 = a_3 x_1(\tau_1) + b_3 x_2(\tau_2) + c_3 x_3(\tau_3). \tag{3.11}$$

where a_i, b_i, and c_i are the coefficients that are determined on the basis of CE. x_1, x_2, and x_3 indicate the complex amplitudes of LP01, LP11, and LP21, respectively. τ_i is the duration of i^{th} mode transmit in the fiber. Thus, each equation includes three terms, a signal component and two crosstalk components.

It should be noted that in contrast to the definition of crosstalk components in mode exchange by VHET, when the spatial modes are separated by a DEMUX, the components of the received signal in the output port are described as

$$S_1 = a_1 x_1(\tau_1) + a_2 x_1(\tau_2) + a_3 x_1(\tau_3), \tag{3.12}$$

$$S_2 = b_1 x_2(\tau_1) + b_2 x_2(\tau_2) + b_3 x_2(\tau_3), \tag{3.13}$$

$$S_3 = c_1 x_3(\tau_1) + c_2 x_3(\tau_2) + c_3 x_3(\tau_3). \tag{3.14}$$

In the mode DEMUX, S_1, S_2, and S_3 indicate the components of the received signal in the outports of LP01, LP11, and LP21, respectively. Considering the output port of LP01 as an example, when LP21 is converted to LP01 by VHET, the components of LP11 and LP21 are generated simultaneously as holographic crosstalk. However, these components of LP11 and LP21 are not outputted from the outport of LP01 in the mode DEMUX; thus, they do not become crosstalk after mode separation. The LP01 component generated in the conversion of LP11 to LP11 and the LP01 component generated in the conversion of LP01 to LP21 in VHET must be added as the output of the crosstalk from the outport of LP01. Among the various crosstalk components that are coupled from the VHET to the FMF, only the crosstalk components having the same spatial mode as the signal are outputted to each outport of the mode DEMUX.

Table 3.2. Components of diffracted beam.

Output mode	Mode	Signal
LP01	LP01	$a_0x_0(n_0)$
	LP11	$a_1x_0(n_1)$
	LP21	$a_2x_0(n_2)$
LP11	LP01	$b_0x_1(n_0)$
	LP11	$b_1x_1(n_1)$
	LP21	$b_2x_1(n_2)$
LP21	LP01	$c_0x_2(n_0)$
	LP11	$c_1x_2(n_1)$
	LP21	$c_2x_2(n_2)$

Next, we evaluated the exchange performance based on the CE and XT characteristics. Figure 3.6 shows the value CE and XT characteristics for the exchange between two modes LP01 and LP11 by proposed method. In the conversion of LP01 to LP11, the CE of the signal component is 97.3% and crosstalk is -24.5 dB. In the conversion of LP11 to LP01, the CE of the signal component is 53.6% and crosstalk is -31.0 dB. The CEs are beyond 53.6% and the crosstalk components are lower than -24.5 dB. These results confirmed that the signal components are diffracted at the incident angle of the reference beam and converted to the desired mode successfully with the low crosstalk. Figure 3.7 shows the simulation results of exchanging between three mode LP01, LP11, and LP21. CEs of the conversion from LP01 to LP21, LP11 to LP11, and LP21 to LP01 are 52%, 30%, and 17%, respectively. In the conversion of LP21 to LP01, the crosstalk is 0.4 dB, indicating that crosstalk

component is larger than signal component. From the simulation results, the reconstruction quality is severely degraded by crosstalk. Figure 3.8 shows the normalized intensity distribution of mode fields. These results show that unwanted intensity peaks appear around the signal components. Moreover, the exchange performance becomes worse as the number of spatial modes increases. This is attributed to the crosstalk generated from the non-target holograms, as the other spatial modes are also multiplex recorded in the entire volume of holograms in which a specific spatial mode is recorded [9]. When the number of spatial modes increases, the crosstalk generated from non-target holograms increases. However, in MDM systems, the transmission capacity is in proportion to the number of spatial modes. Thus, it is essential to reduce the crosstalk components diffracted from the non-target hologram in VHET. To address this issue, we demonstrate the VHET combined with phase plates to reduce the crosstalk in the next chapter. Nonetheless, as the simulation results show, the multiple spatial modes can be exchanged simultaneously by VHET.

Input	Output	CE	MXT
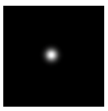	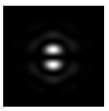	97.3%	-24.5 dB
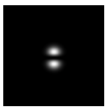		53.6%	-31.0 dB

Figure 3.6. CE and XT characteristics for exchange between LP01 and LP11.

Input mode	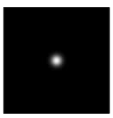		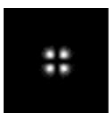
Desired mode			
Diffracted mode			
CE	52%	30%	17%
Maximum crosstalk	-6.9 dB	-30.1 dB	0.4 dB

Figure 3.7. CE and XT characteristics for exchange between LP01, LP11, and LP21.

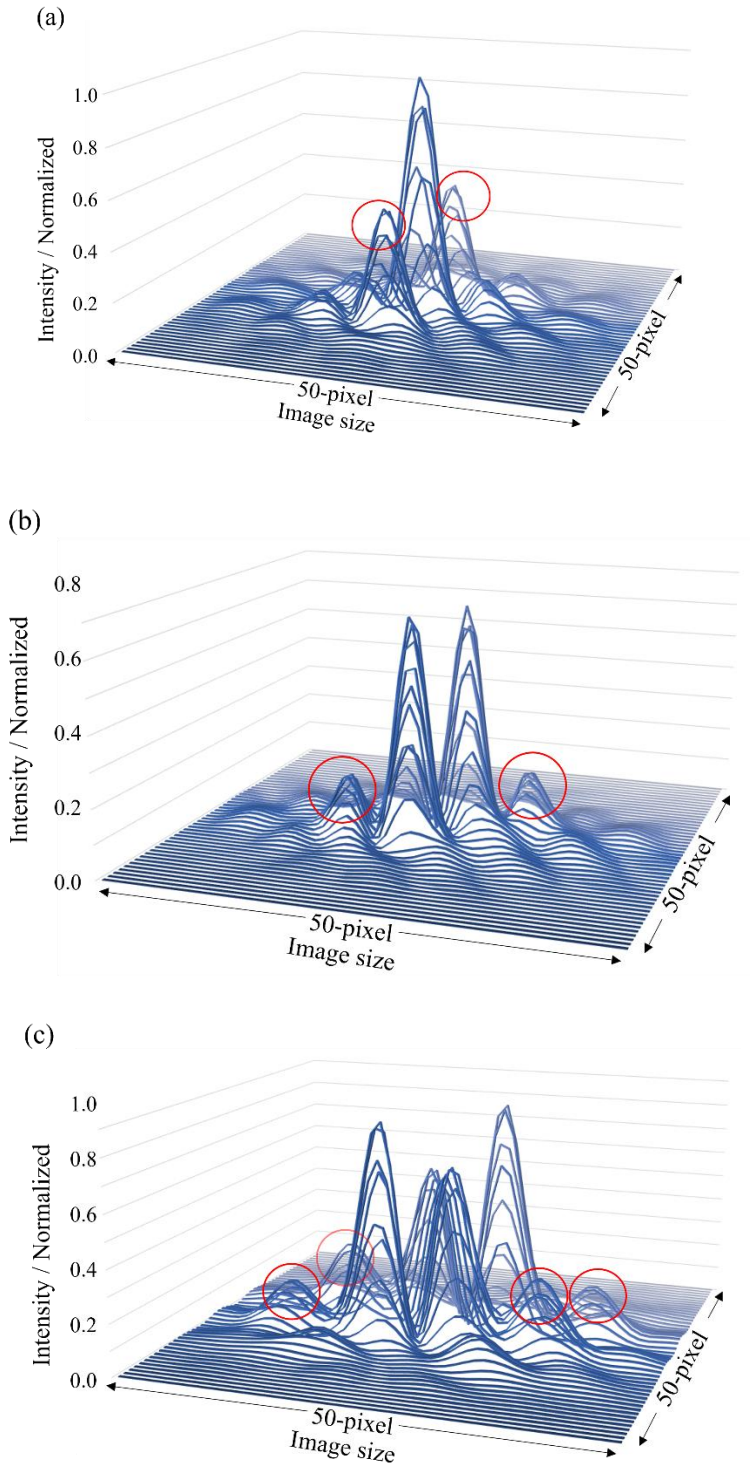

Figure 3.8. Intensity distributions of spatial modes by proposed method.

(a) LP01. (b) LP11. (c) LP21.

3.4 Spatial mode exchange experiment

3.4.1 Experimental setup

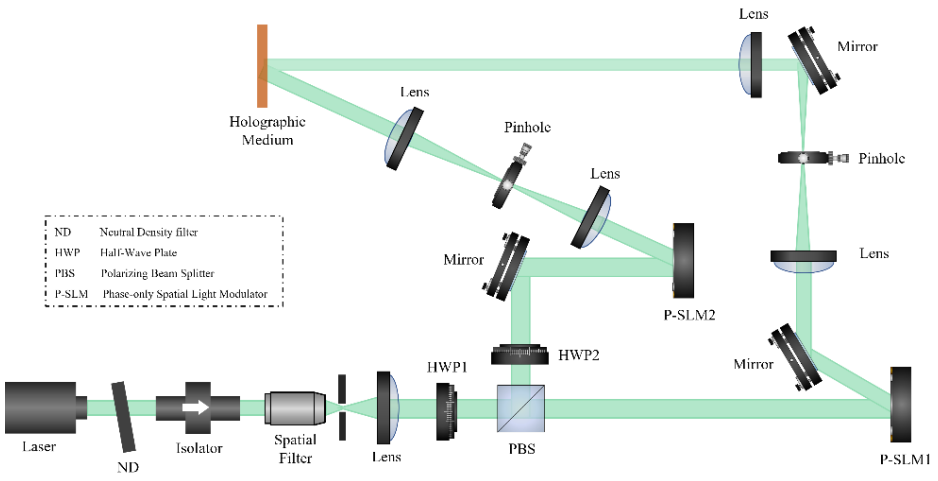

Figure 3.9. Experimental setup for spatial mode exchange.

Figure 3.9 shows the experimental setup for spatial mode exchange using volume holograms. We performed an experiment on exchanging for an LP mode group comprising LP01, LP11, and LP21. We exchange LP01 and LP21 to compensate for the difference in the transmission speeds. LP11 does not change. Thus, in this experiment, LP01, LP11, and LP21 were changed to LP21, LP11, and LP01, respectively. A photopolymer [14,15] with thickness of 400 μm is used as the recording medium. A diode-pumped solid-state laser at a wavelength of 532 nm, which is within the sensitivity range of the photopolymer, is used as the light source. The laser beam is cleaned up and expanded using a spatial filter, a pinhole, and a lens after passing through an isolator. The light beam is then divided into the writing and reference arms using a polarizing beam splitter (PBS), combing with a half-wave plate (HWP) to control the power density ratio of the writing beam (p-polarized light) and reference beam (s-polarized light). Here, the reference beam is then modulated to a p-polarized light by a HWP to interfere with the writing beam. The power densities of two light beams are adjusted to about 1.95 mW/cm^2 on the photopolymer. The complex amplitude of each spatial mode is sequentially generated by a phase-type spatial light modulator (PSLM, Santec SLM-100) displaying computer-generated holograms (CGHs) [16] on it. The pixel size of the PSLM is 10 μm, and the gap between each pair of adjacent pixels is 0.4 μm. The CGH is calculated using an interference pattern between a spatial mode field and a plane wave, which enables us to generate an accuracy complex amplitude distribution of the mode filed. The size of the mode filed generated by CGH is 1.8 mm. Subsequently, a pinhole, placed along the Fourier plane of the 4-*f* system, is used to extract the first-order diffracted beam due to the CGH generates other order diffracted beams. The incident angle of the reference beam is set to 14°. The exposure times are set to 12s to ensure all modes are diffracted with almost the same

efficiency. After recoding all the holograms, signal beams are sequentially irradiated into the photopolymer along the same path as that of the writing beams during the recording procedure. Subsequently, the diffracted beams are shaped to fit the complex amplitude distributions corresponding to those of the reference beam by using a lens.

3.4.2 Experimental results and discussion

The i^{th} (i = 1,2,3) spatial mode of the diffracted beam is reconstructed by irradiating the multiplexed holograms with the n^{th} (n = 1,2,3) mode of MDM signals denoted as $D_{m,i}$. The spatial mode component corresponds to the reference beam as a signal component, and the other diffracted components correspond as crosstalk. We evaluate the exchange performance by calculating the diffracted efficiency (DE). The DE of the signal component reconstructed by irradiating the m^{th} mode is denoted as DE_m, and is expressed as

$$DE_m = \frac{P_{m,m}}{P_0 + \sum_i P_{m,i}} \tag{3.15}$$

where P_0 and $P_{m,i}$ are the optical power of the zero-order beam and $D_{m,i}$, respectively. Table 3.3 shows the DE characteristics for incident beam of each spatial mode. In the conversions of LP01 to LP21, LP11 to LP11, and LP21 to LP01, the DEs are 0.65%, 2.24%, and 0.59%, respectively. Although the desired spatial modes are reconstructed successfully, the DEs are extremely low. We note that the DE from LP11 converted to LP11 is higher than the other conversion cases. The reasons considered as the beam diameter of the reference beams is small, and the incident beam did not sufficiently overlap with the recorded holograms. To ensure the visibility of the interference fringes, the power density ratio of the writing beam and the reference beam is approximately 1:1, and the power of the reference beam is slightly stronger than that of the writing beam as shown in Fig. 3.10. Moreover, the beam diameter of the reference beam prefers to sufficiently cover the fields of the writing beam. However, in this experiment, the distribution of 1.8 mm mode field is displayed on the SLM to generate the writing beam and reference beam. The impulse width of LP 21 is larger than that of LP01. Thus, in the conversion of LP01 and LP21, the writing beam and the reference beam cannot sufficiently overlap, resulting in the imperfection of the interference fringes. In the future research, we will improve the DE characteristics by adjusting the beam diameter of the reference beam and writing beam.

Table 3.3 DE characteristics for incident beam of each spatial mode.

Incident beam	Diffracted beam	Power density	Exposure time	DE
LP01	LP21	1.96 mW/cm^2	12 s	0.65 %
LP11	LP11	1.95 mW/cm^2	12 s	2.24 %
LP21	LP01	2.01 mW/cm^2	12 s	0.59 %

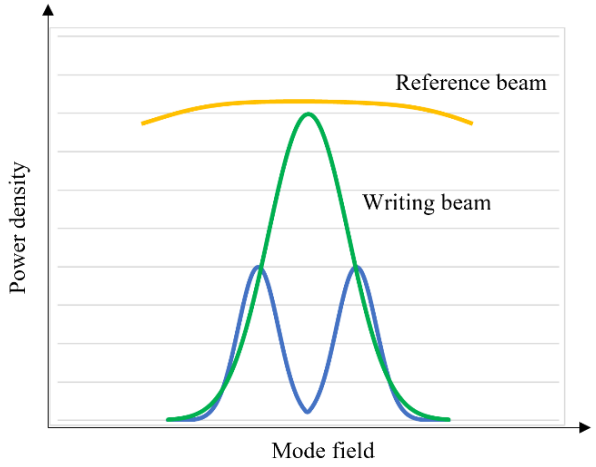

Figure 3.10. Power density relationship between the reference beam and writing beam.

3.5 VHET combined with Dual-wavelength method

As stated above, VHET exhibits its potentiality for spatial mode exchange in MDM transmission systems. However, applying VHET to practical optical communication systems is difficult, as typical holographic mediums have no sensitivity in the infrared region, which includes optical transmission bands. To address this issue, we propose a VHET combined with dual-wavelength method (DWM). The DWM, which was proposed for non-destructive reconstruction of recorded holograms in holographic data storages (HDS) [17,18], allows light of different wavelengths to be used in the recording and exchange procedure. By this method, VHET can be realized in the optical transmission bands. In this section, we describe the principle of DWM and combine it with VHET to realize the application for optical communication bands.

3.5.1 Operational principle of DWM

Figure 3.11 shows a conceptual diagram of the DWM applied in a volume hologram. This method can use different wavelengths by adjusting the incident angle of the beam according to Bragg condition, which is expressed as

$$\Lambda = \frac{\lambda_w}{2\sin\theta_w}, \tag{3.16}$$

where Λ is the grid spacing of a volume hologram recorded the interference fringes between the writing beam and the reference beam. λ_w is the wavelength of writing beam, and θ_w is the incident angle. According to the Bragg condition, when the wavelength and the incident angle of readout beam satisfy Eq. 3.16, the readout beam can be strongly diffracted. If the wavelength of the readout beams

different from λ_w, the Bragg condition is expressed as

$$\frac{\lambda_w}{2\sin\theta_w} = \frac{\lambda_r}{2\sin\theta_r}, \tag{3.17}$$

Where λ_r and θ_r are the wavelength and the incident angle of the recoded hologram of the readout beam, respectively. As shown in Fig. 12, when the λ_r and θ_r satisfy Eq. 3.17, holograms can be reconstructed. By this method, the holograms can be recorded in a recording medium within the sensitivity range and reconstructed using readout beams at wavelengths outside of the sensitivity range of recording medium.

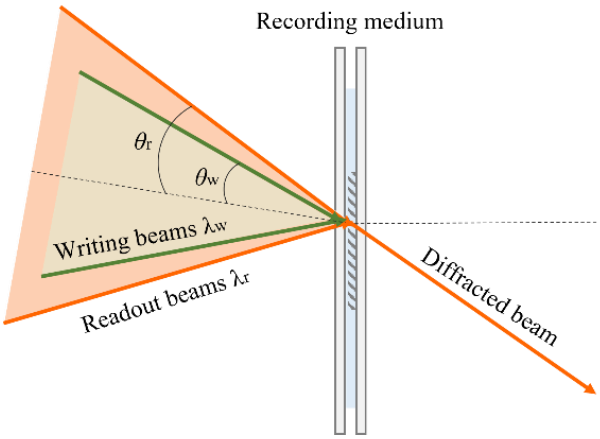

Figure 3.11. Conceptual diagram of the DWM.

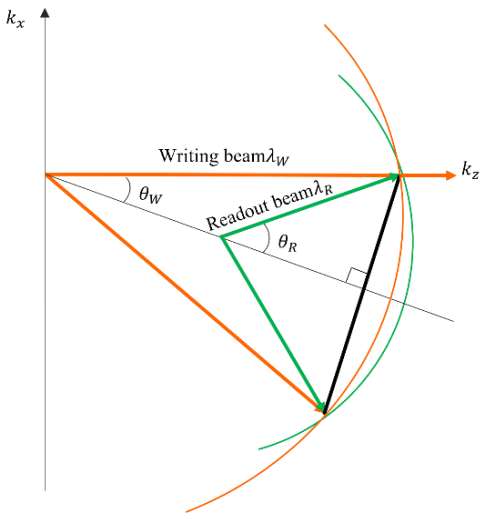

Figure 3.12. Schematic diagram of Ewald sphere.

Then, we describe the basic operation of the VHET using the DWM. Figure 3.13 shows the conceptual diagram of our proposal which consists of recording and exchange procedures. During the recoding procedure (Fig. 3.13(a)), the interference fringes between writing beams and reference beams

are recorded in the recording medium. The incident angle of reference beams is θ. During the exchange procedure (Fig. 3.13(b)), the signal beams is irradiating the holograms with the angle θ_s which fulfilling the Bragg's condition with corresponding to all recoded holograms, and then the spatial mode components are diffracted simultaneously at the incident angle of the reference beam and shape to the complex amplitude distributions corresponding to those of reference beam, respectively.

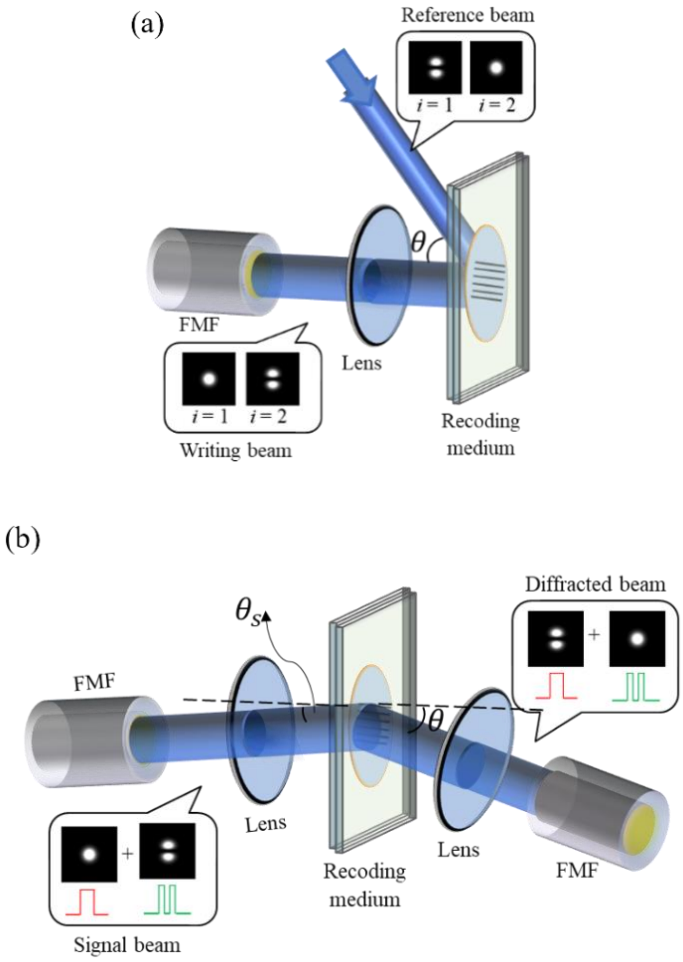

Fig. 3.13. Schematic diagram of the proposed method. (a) Recording procedure. Writing beams are incident on a recording medium sequentially with reference beams to record holograms. (b) Reconstruction procedure. By irradiating the holograms with the MDM signal beam at an angle satisfying the Bragg condition, the spatial modes are diffracted simultaneously.

3.5.2 Numerical simulation of VHET combined with the DWM

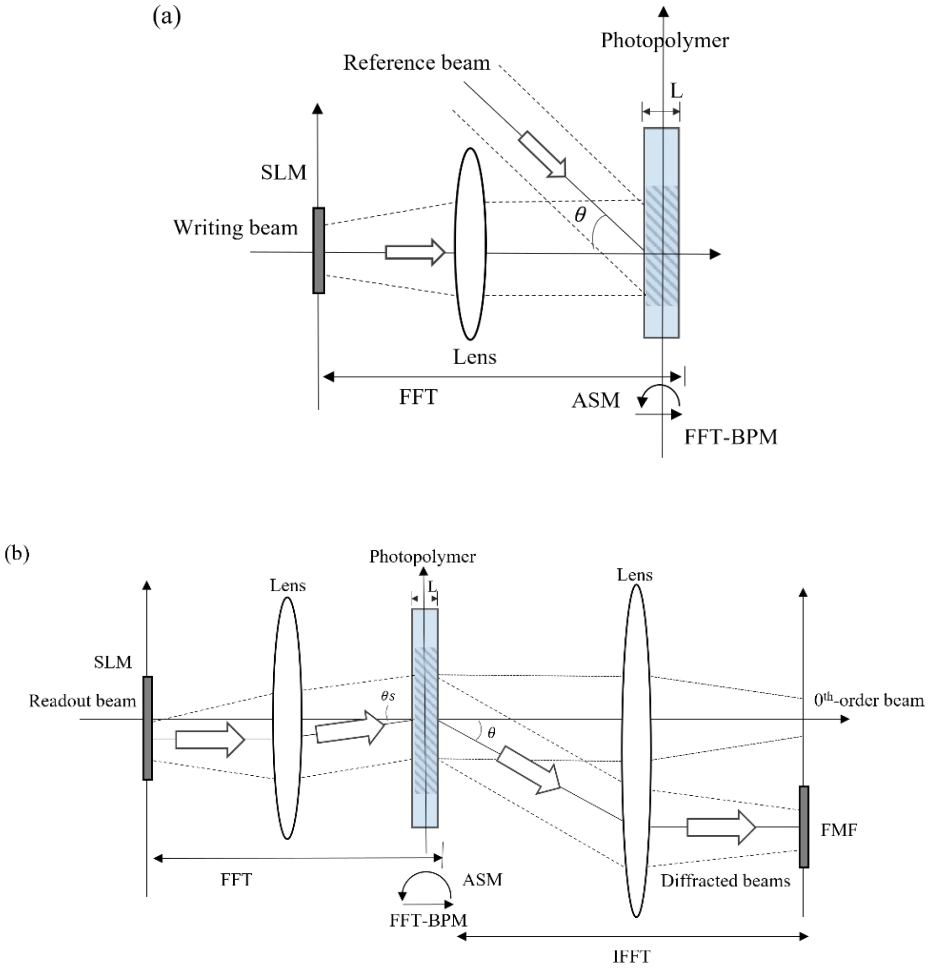

Figure 3.14. Simulation model. (a) Recording procedure. (b) Exchange procedure.

To confirm the basic operation of the proposed scheme, we performed a numerical simulation between the spatial mode LP01 and LP11. We describe the simulation model shown in Fig. 3.14. The calculation flows are the same as stated in Section 3.3.1. Here, we assume that a light source with a wavelength of 532 nm, which is within the sensitivity range of the photopolymer, is used as the writing beam. A light source with a wavelength of 1550 nm, which has the lower loss in the C bands, is used as the readout beam. During the recording procedure (Fig. 3.14(a)), the complex amplitudes of the spatial modes are generated as the writing beam and reference beam with an oblique phase corresponding to the incident angle θ in the Fourier space. The complex amplitudes on the back surface of the recording medium are then calculated by FFT. Subsequently, the complex amplitudes of the spatial modes on the front surface of the recording medium are acquired using ASM. The refractive index distribution of each layer is calculated by using FFT-BPM. This process is performed for the number for modes m, and the refractive index distribution in the photopolymer is obtained by m

multiple recordings. During the reconstruction procedure (Fig. 3.14(b)), the readout beam is generated with a wavelength of 1550 nm, and the incident angle satisfy the Bragg condition. The complex amplitude distributions of the diffracted beam are calculated in the same manner as the recording procedure. Subsequently, the complex amplitude of the diffracted beam received on the FMF plane was calculated by FFT. In the simulation, we assumed that recording medium is a photopolymer with a thickness of 150μm. The angle factor is set to 2.0°.

3.5.3 Simulation results and discussion

We evaluate the reconstruction quality by calculating the crosstalk characteristics and CE between each obtained complex amplitude of the diffracted beam and that of the desired ideal mode. Figure 3.15 shows the simulation results by using the proposed method. In the conventional method, both the writing beam and reference beam use the light source with a wavelength of 1550 nm. In the proposed method, the wavelength of writing beam is 532 nm which within the sensitivity range of recording medium, and the wavelength of readout beam is 1550 nm which the transmission loss is minimized in the practical optical communication bands. Compared with the simulation results by the conventional method shown in Fig. 3.6, the intensity distributions of the diffracted beams by VHET combined with the DWM are the same as that of conventional method. Moreover, the CE in the conversion of LP01 to LP11 is 99.3%, and in the conversion of LP11 to LP01 is 55.4%, which are slightly higher than that of the conventional method. This is because the wavelength and the incident angle will affect the diffracted efficiency according to the coupled-wave theory [19]. Nonetheless, these results confirmed that the VHET can be applied in the optical transmission bands by combining with the dual-wavelength method.

Input	Output	CE	MXT
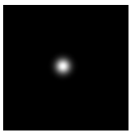		99.3%	-24.6 dB
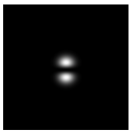	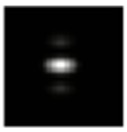	55.4%	-29.4 dB

Figure 3.15. CEs and XTs by VHET combined with the DWM.

3.6 Summary

In this chapter, we proposed a mode exchange technique using volume holograms for MDM transmission systems to reduce the differential mode delay. In this work, VHET utilizes multiplexed volume holograms

to exchange multiplexed spatial modes simultaneously. Thus, the cost and the size of the optical system are markedly lower because this scheme requires only a volume hologram, which is independent of the number of multiplexed modes. To confirm the basic operation of the proposed method, a mode-exchange numerical simulation was conducted using an LP mode group comprising of LP01, LP11, and LP21. Moreover, dual-wavelength method was proposed to realize the application of VHET in the practical optical transmission bands. As a result, in the exchange of the two modes, the CEs were beyond 53.6% and the maximum crosstalk was -24.5 dB. In the exchange of three modes, the CEs were beyond 17% and the maximum crosstalk was 0.4 dB. Although the multiple spatial modes can be exchanged simultaneously by the proposed method, it is essential to reduce the crosstalk to improve the reconstruction quality. Moreover, the simulation results of the VHET combined with dual-wavelength method are the same as the conventional method, which indicated that VHET can be applied in the practical optical transmission bands by using dual-wavelength method.

References

[1] S. Berdagué and P. Facq, "Mode division multiplexing in optical fibers," Appl. Opt. **21**(11), 1950-1955 (1982).

[2] R. Ryf, S. Randel, A. H. Gnauck, C. Bolle, A. Sierra, S. Mumtaz, M. Esmaeelpour, E. C. Burrows, R.-J. Essiambre, P. J. Winzer, D. W. Peckham, A. H. McCurdy, and R. Lingle, "Mode-division multiplexing over 96 km of few-mode fiber using coherent 6 × 6 MIMO processing," J. Light. Technol. **30**(4), 521-531 (2012).

[3] A. Okamoto, K. Morita, Y. Wakayama, J. Tanaka, and K. Sato, "Mode division multiplex communication technology based on dynamic volume hologram and phase conjugation," Proc. SPIE 7716, 771627 (2010).

[4] T. Sakamoto, T. Mori, T. Yamamoto, and S. Tomita, "Differential mode delay managed transmission line for WDM-MIMO system using multi-step index fiber," J. Light. Technol. **30**(17), 2783-2787 (2012).

[5] T. Sakamoto, T. Mori, T. Yamamoto, N. Hanzawa, S. Tomita, F. Yamamoto, K. Saitoh, and M. Koshiba, "Mode-division multiplexing transmission system with DMD-independent low complexity MIMO processing," J. Light. Technol. **31**(13), 2192-2199 (2013).

[6] Y. Wakayama, D. Soma, K. Igarashi, H. Taga, and T. Tsuritani, "Intermediate mode interchange for reduction of differential mode-group delay in weakly-coupled 6-mode fiber transmission line," Proc. OFC2016, M3E.6 (2016).

[7] E. Chuang and D. Psaltis, "Storage of 1, 000 holograms with use of a dual- wavelength method," Appl. Opt. **36**, 8445-8454 (1997).

[8] S. Shimizu, A. Okamoto, F. Mizukawa, K. Ogawa, A. Tomita, T. Takahata, S. Shinada, and N. Wada,

"Volume holographic spatial mode demultiplexer with a dual-wavelength method," Appl. Opt. **57**(2), 146-153 (2018).

[9] A. Shibukawa, A. Okamoto, Y. Wakayama, A. Tomita, H. Funakoshi, and K. Sato, "Digital image diffusion technique for suppressing interpage crosstalk in holographic data storage," Jpn. J. Appl. Phys. **52**, 09LD03 (2013).

[10] Y. Wakayama, A. Okamoto, K. Kawabata, A. Tomita, and K. Sato, "Mode demultiplexer using angularly multiplexed volume holograms," Opt. Express **21**(10), 12920-12933 (2013).

[11] A. Shibukawa, A. Okamoto, M. Takabayashi, and A. Tomita, "Spatial cross modulation method using a random diffuser and phase-only spatial light modulator for constructing arbitrary complex fields," Opt. Express **22**(4), 3968-3982(2014).

[12] K. Matsushima, H. Schimmel, and F. Wyrowski, "Fast calculation method for optical diffraction on tilted planes by use of the angular spectrum of plane waves," J. Opt. Soc. Am. A **20**(9), 1755-1762 (2003).

[13] J. Tanaka, A. Okamoto, and M. Kitano, "Development of Image-Based Simulation for Holographic Data Storage System by Fast Fourier Transform Beam-Propagation Method," Jpn. J. Appl. Phys. **48**(3), 03A028 (2009).

[14] C. Katahira, N. Morishita, J. Ikeda, P. B. Lim, M. Inoue, Y. Iwasaki, H. Aota, and A. Matsumoto, "Mechanistic discussion of cationic crosslinking copolymerizations of 1,2-epoxycyclohexane with diepoxide crosslinkers accompanied by intramolecular and intermolecular chain transfer reactions," J. Polym. Sci. A Polym. Chem. **48**, 4445-4455 (2010).

[15] J. Ikeda, R. Arai, N. Morishita, C. Katahira, Y. Takatani, S. Yumoto, K. Yokouchi, Y. Hayashi, Y. Tanaka, K. Watanabe, P. B. Lim, and M. Inoue, "Nano-gel photopolymer recording material," in Proceedings of International Workshop on Holographic Memories and Display (IWHM&D, 2009), 3A-4.

[16] F. Dubois, P. Emplit, and O. Hugon, "Selective mode excitation in graded-index multimode fiber by a computer-generated optical mask," Opt. Lett. **19**, 433-435 (1994).

[17] F. H. Mok, "Angle-multiplexed storage of 5000 holograms in lithium niobate," Opt. Lett. **18**(11), 915-917 (1993).

[18] D. Psaltis and G. W. Burr, "Holographic data storage," Computer **31**(2), 52-66 (1998).

[19] H. Kogelnik, "Coupled-wave theory for thick hologram grating," Bell Syst. Tech. J., 48(9), 2909-2947 (1969).

Chapter 4

Methods of Improving Reconstruction Quality for VHET

4.1 Introduction

In mode-division multiplexing (MDM) systems, a reduction in differential mode delay (DMD) is essential to facilitate long-haul transmissions. We proposed a spatial mode exchange technique using volume holograms (VHET) to reduce the DMD in chapter 3. Using this method, VHET can reduce the DMD by exchanging multiple spatial modes with different transmission speeds in an FMF using volume holography. The cost and size of the optical system are markedly lower because this scheme requires only a single holographic medium, which is independent of the number of multiplexed modes. Nevertheless, the reconstruction quality of VHET is severely degraded by crosstalk (XT) owing to the non-target holograms, as the other spatial modes are also multiplex recorded in the entire volume of holograms in which a specific spatial mode is recorded [1,2]. Moreover, previous studies also have indicated that reconstruction quality is affected by the correlation of the intensity distributions in the mode fields [3,4]. In MDM systems, near-order modes with large overlaps are widely used. The reconstruction quality decreases as the overlap amount increases.

Thus, we propose three methods of combining VHET and phase plates to improve the reconstruction quality. In Section 4.2, the method of VHET combined with a phase plate is proposed to reduce the intensity overlap of spatial modes. In Section 4.3, the method of VHET combined with a random optical diffuser is proposed to improve the exchange accuracy due to the reduction in the influence of non-targeted holograms. In Section 4.4, the mode diffusion technique combined with VHET is then proposed to reduce the data-page crosstalk. In Section 4.5, the simulation results and prospects of this work are summarized and discussed.

4.2 VHET combined with a phase plate

Previous studies have indicated that the separation performance of a volume holographic demultiplexer (VHDM) with a large overlap is lower than that with a small overlap. The basic principle

of our proposed VHET is the same as that of the VHDM because they both utilize volume holograms to reconstruct spatial modes. Thus, the reconstruction quality of VHET is also degraded because of the intensity overlap between the spatial modes. Since the amount of overlap between spatial modes tends to increase as the mode is closer in order, it is serious in typical MDM systems. However, the near-order modes with large mode overlap are expectedly used in MDM systems [2]. In this work, to improve the performance of the VHET for near-order modes without significantly increasing the number of optical elements, the VHET combined with a phase plate is proposed. In this method, reconstruction quality can be improved by converting the intensity distribution of near-order modes with a high correlation to that of far-order modes with a low correlation. To confirm the basic operation of the proposed method, we perform a numerical simulation of a specific linearly polarized (LP) mode group consisting of LP01, LP11a, and LP11b.

4.2.1 Operational principle

In this section, we will describe the operational principle of the VHET combined with a phase plate. Figure 4.1 shows the schematic diagrams of the proposed scheme of an exchange between two spatial modes LP01 and LP11, as the simplest case for an explanation. The scheme consists of recording and exchange procedures. The recording procedure (Fig. 4.1(a)) generates a doubly multiplexed volume hologram. For the first hologram (i=1), the spatial mode LP01 is used as the writing beam and spatial mode LP11 is used as the reference beam. We modulate the phase of the writing beam by a phase plate to convert the intensity distribution and reduce the intensity overlap between LP01 and LP11. Then, interference fringes between the converted beam and reference beam are recorded in the recording medium. For the second (i=2) hologram, the two spatial modes interchange their role. The writing mode LP11 is converted similarly and the interference fringe with the reference mode LP01 is recorded at the same spot as the first hologram. The writing beam is vertically incident on the recording medium and propagates along the z-axis. The reference beam forms an angle θ with the z-axis. Thus, the writing beam W_i (i = 1, 2, …, m) and reference beam R_{m-i+1} are expressed as follows:

$$W_i = A_i(x, y, z)\exp[\,jkz + j\varphi_i(x, y, z)] \tag{4.1}$$

$$R_{m-i+1} = A_r(x, y, z)\exp[\,jk(x\sin\theta + z\cos\theta) + j\varphi_r(x, y, z)] \tag{4.2}$$

where A_i (x, y, z) and A_r (x, y, z) are the amplitudes and φ_i (x, y, z) and φ_r (x, y, z) are the phase distributions of the writing and reference beams, respectively; k is the wave number in the recording medium. Next, we modulate the intensity distribution of the writing beam using a phase plate and a lens. The converted beam W_i' is expressed as

$$W_i' = A_i'(x, y, z)\exp[jkz + j\varphi_i'(x, y, z)] \tag{4.3}$$

where A_i' (x, y, z) and φ_i' (x, y, z) are the amplitude and phase distribution of the converted beam, respectively. The complex amplitude transmittance T (x, y, z) of the recorded holograms of the converted beam and reference beam is expressed as

$$\begin{aligned} T(x, y, z) = \sum_{i=1}^{N} A_r(x, y, z) A_i'^{*}(x, y, z) \exp[j(\varphi_r(x, y, z) - \varphi_i'(x, y, z)) \\ + jkx\sin\theta + jkz(\cos\theta - 1)] \end{aligned} \tag{4.4}$$

where * denotes a complex conjugate. Here, the intensity overlap of spatial modes is reduced due to the intensity distribution of spatial modes modulated by a phase plate. The profile of the phase plate is determined by the combinations of spatial modes.

During the exchange procedure (Fig. 4.1(b)), the MDM signal S, which consists of spatial modes LP01 and LP11, is collimated and converted by the phase plate whose profile is the same as that used in the recording procedure. When the multiplexed volume holograms are irradiated by the converted signal beam, the spatial mode components are diffracted as

$$\begin{aligned} D &= \eta \int_0^L TS dz \\ &= \eta \sum_{n=1}^{m} \sum_{i=1}^{m} \int_0^L a_n(t) A_n' A_i'^{*} A_r \exp\left[j\left(\varphi_n' - \varphi_i' + \varphi_r\right) + jk\left(x\sin\theta + z\cos\theta\right)\right] dz \end{aligned} \tag{4.5}$$

where L is the thickness of the recording medium, η is the diffraction efficiency, and $a_n(t)$ is the time series signal. A_n' and φ_n' (n = 1, 2, …, m) are the amplitude and phase distribution of the converted signal beam, respectively. When $n = i$, the spatial mode component is converted to a beam, of which, the spatial phase corresponds to that of the reference beam and is strongly diffracted in the direction of θ. When $n \neq i$, the mode fields between the writing beams and MDM signals are mismatched, and the spatial mode components are weakly diffracted as crosstalk components. Here, the crosstalk components generated by the hologram can be suppressed by reducing the overlap amount of the intensity distributions using a phase plate. Consequently, the diffracted beam D is expressed as follows:

$$D = \eta \sum_{n=1}^{m} a_n(t) \int_0^L \left|A_n'\right|^2 A_r \exp\left[j\varphi_r + jk\left(x\sin\theta + z\cos\theta\right)\right] dz \tag{4.6}$$

The spatial mode components of the signal beams are diffracted simultaneously at the incident angle of the reference beam. The diffracted beam is shaped to fit the complex amplitude distributions corresponding to those of the reference beam by using a lens. According to Eq. 4.6, the diffracted beam is mostly not modulated by the non-targeted holograms because the intensity distribution of the signal beam is converted to $|A_n'|^2$ by using a phase plate, resulting in a low overlap with the A_r. Thus,

a highly accurate exchange function can be performed by utilizing both the phase matching characteristics of a volume hologram and the conversion of the intensity distribution of spatial modes using a phase plate.

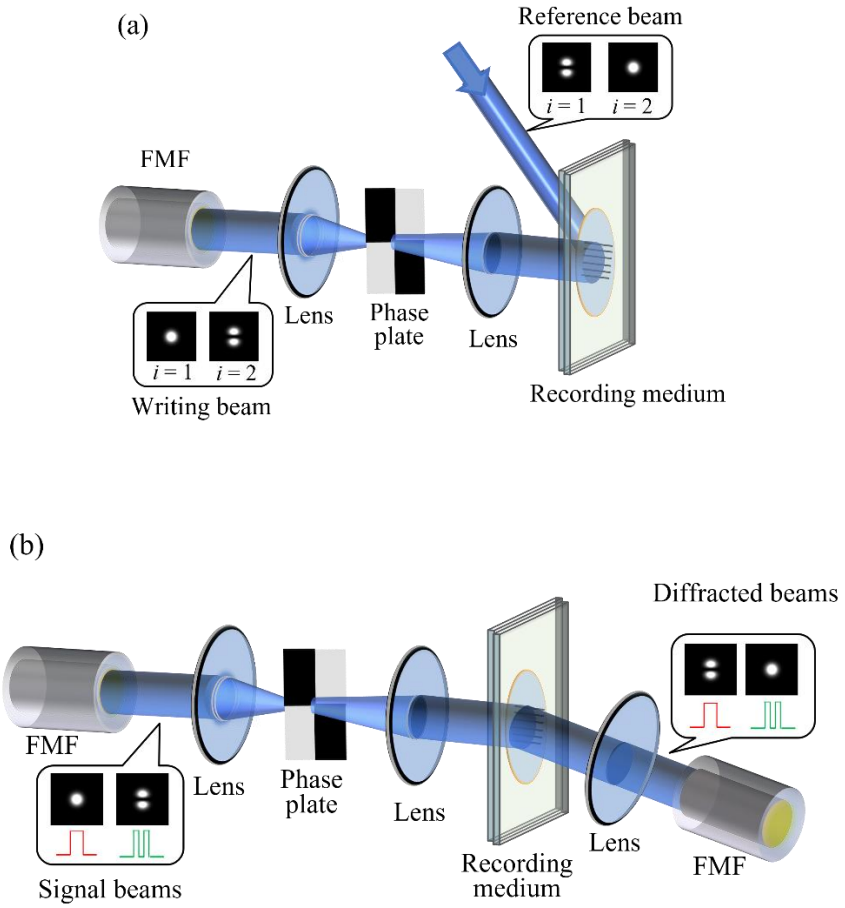

Figure 4.1. Schematic diagrams of VHET combined with a phase plate.
(a) Recording procedure. (b) Exchange procedure.

4.2.2 Simulation model

To validate the basic operation of the proposed method, we performed a numerical simulation. The models and flow of the simulations are shown in Figure 4.2. During the recording procedure (Fig. 4.2(a)), the complex amplitudes of spatial modes are generated as the writing beam and reference beam with an oblique phase corresponding to the incident angle θ in the Fourier space, and they are collimated by fast Fourier transform (FFT). Subsequently, the phase distribution of the writing beam was modulated by a phase plate. The complex amplitudes on the back surface of the recording medium were then calculated by FFT. Here, the intensity of writing beam was converted depend on the phase distribution by optical FFT. Subsequently, the complex amplitudes of spatial modes on the front surface of the recording medium were acquired using an antidromic angular spectrum method (ASM) [5]. We calculated the refractive index distribution of each layer induced by the interference fringe profile in the photopolymer using the FFT beam propagation method (FFT-BPM) [6]. This process was performed for the number of modes *m*, and the refractive index distribution in the photopolymer was obtained by *m* multiple recordings. During the exchange procedure (Fig. 3(b)), the intensity distribution of the MDM signals, which is consistent with the writing beams, was collimated and transformed by a phase plate and a lens. The complex amplitude of the diffracted beam was then acquired in the same manner as the recording procedure. Subsequently, the complex amplitude of the diffracted beam received on the FMF plane was calculated by FFT. This process was repeated *m* times.

The simulation parameters are presented in Table 4.1. We assumed that the wavelength of the light source is 1550 nm. The recording medium was a photopolymer with a thickness of 150 μm, and the incident angle θ was set to 6°. We performed an exchange between three near-order modes of LP01, LP11a, and LP11b. LP01, LP11a, and LP11b were changed to LP11a, LP11b, and LP01, respectively. The profile of the phase plate was set to the phase profile of LP21. To evaluate the proposed method, we also performed a numerical simulation by the conventional method without a phase plate under the same conditions.

Table 4.1. Simulation parameters of VHET combined with a phase plate.

Common parameters			
Wavelength of beam source	1550 nm	Average refractive index	1.5
Incident angle of reference beam	6°	Pixel number	1024 × 1024
Thickness of photopolymer	150 μm	Pitch of data pixel	0.5 μm
Focal length of Fourier transform lens	150 mm	Pitch of *z*-direction, Δz	1.0 μm
Exposure time	0.1 s	Over sampling rate	2

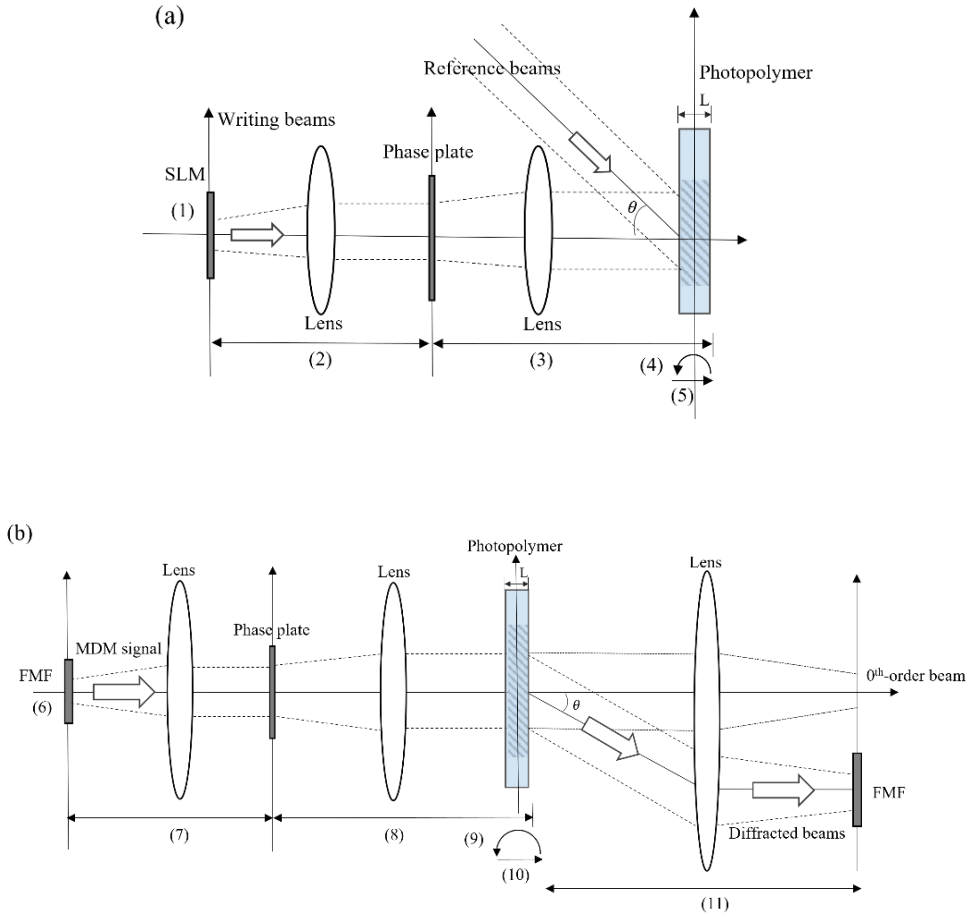

Figure 4.2. Simulation models of VHET combined with a phase plate. (a) Recording procedure. (b) Exchange procedure. Overviews of each process are as follows. (1), (6): Set complex amplitude(s) of each mode. (2), (7): Calculate complex amplitude(s) on the phase plate using FFT. (3), (8): Calculate complex amplitude(s) on the back surface of the photopolymer using FFT. (4), (9): Calculate complex amplitude(s) on the front surface of the photopolymer using the free-space transfer function. (5), (10): Calculate complex amplitude(s) of the inside of the photopolymer using FFT-BPM. (11): Calculate final result on FMF plane using FFT. Processes (1)–(5) and (6)–(11) are repeated for each mode.

4.2.3 Simulation results and discussion

Figure 4.3 shows the profile of phase plate and the intensity distributions of spatial modes with (w/) and without (w/o) the phase modulation. For the quantitative estimation of the intensity overlap amount between two modes, we define the overlap ratio (OR) as the proportion of the overlap area, and it is calculated as

$$\mathrm{OR} = \frac{2\sum_x \sum_y I_o(x,y)}{\sum_x \sum_y \{I_1(x,y) + I_2(x,y)\}} \tag{4.7}$$

where $I_1(x, y)$ and $I_2(x, y)$ are the intensity of refence beam and writing beam, and $I_o(x, y)$ is the overlapping intensity calculated as

$$\mathrm{I}_o(x,y) = \min\{I_1(x,y), I_2(x,y)\} \tag{4.8}$$

Besides, as mentioned above, crosstalk is generally existed during the exchange process. We evaluate the exchange performance based on the CE and XT characteristics according to Eq. (3.7) and Eq. (3.8).

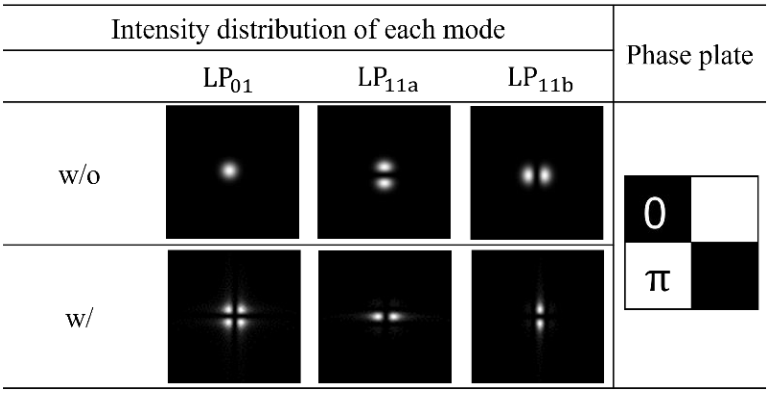

Figure 4.3. Intensity distributions of spatial modes with and without the phase modulation.

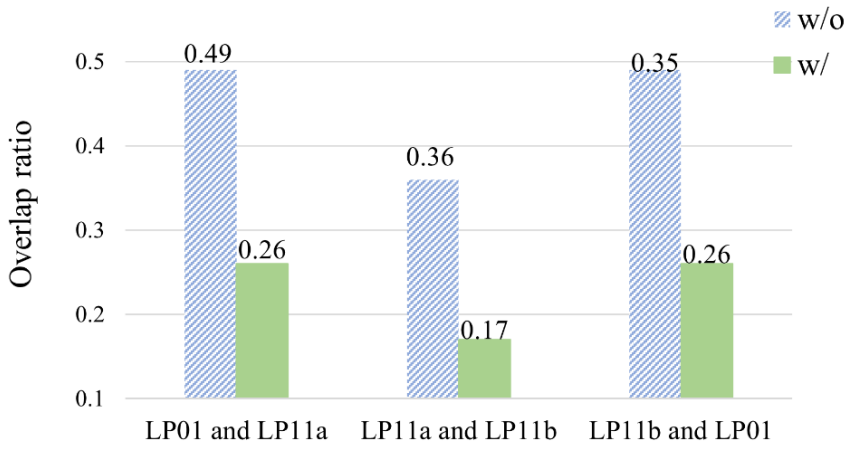

Figure 4.4. ORs of the different combinations of spatial modes.

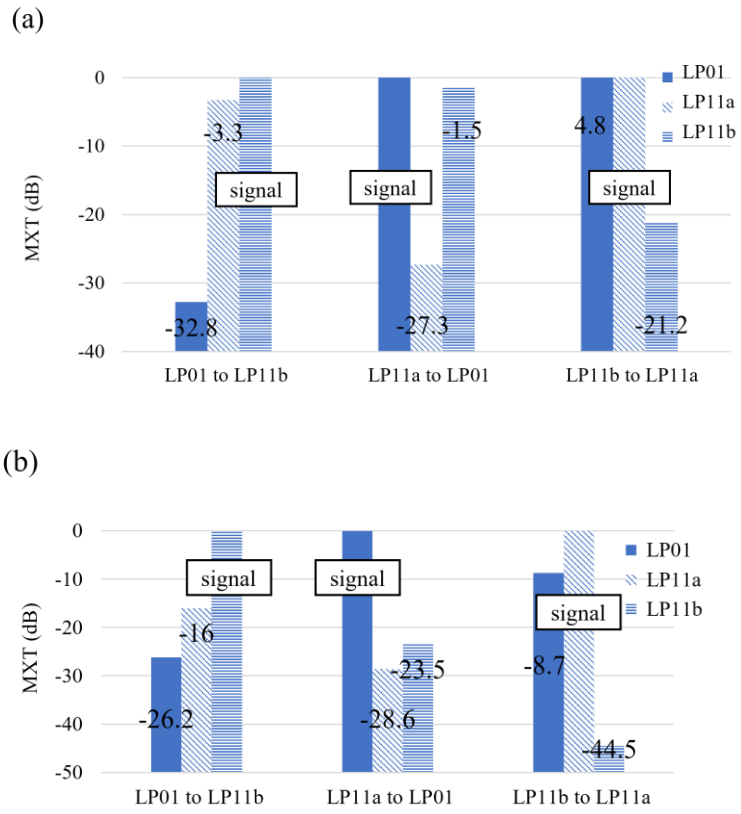

Figure 4.5. XT characteristics of (a) conventional scheme (b) proposed scheme.

Figure 4.3 shows the intensity distribution of each mode with and without the phase modulation. The intensity distribution of each mode is modulated by the phase plate whose phase profile is LP21. Figure 4.4 shows ORs of different combinations of two spatial modes. These results indicated that the ORs were reduced for all the combinations of spatial modes. The overlap amount of LP01 and LP11 was remarkably reduced from 0.49 to 0.26. The maximum OR was lower than 0.26, which indicated that all the combinations of spatial modes with a low correlation can be attained by the proposed method. Figure 4.5 shows the crosstalk characteristics of the proposed method and conventional method, which indicates the desired mode interfered with the other spatial modes. Compared with the conventional scheme, XTs have significantly improved by the proposed scheme. In the conversion between LP11a to LP01, the crosstalk was reduced from -1.49 dB to -23.5 dB, which was the most effective combination for the reduction of OR. The maximum crosstalk was improved from 4.8 dB to -8.7 dB. Moreover, a similar correlation between the crosstalk characteristics and OR has also been observed between the other modes. Here, it is noted that the crosstalk of the conversion from LP01 to LP11b was worse. This is because, in the conventional method, LP01 has a uniform intensity distribution and thus can match LP11b perfectly. In the proposed method, the intensity of LP01 is modulated by the phase plate, which is slightly mismatched with LP11b. These results confirmed that

reducing the intensity overlap between the recorded spatial modes is effective for improving the mode exchange performance. On the other hand, in this simulation, the profile of the phase plate was set to the phase profile of LP21. The phase profile is determined by the phase distribution of the recorded spatial modes. Therefore, to apply the proposed scheme to more mode groups, the profile of the phase plate should be optimized so that the overlap between modes is further reduced.

4.3 VHET combined with a random optical diffuser

Besides the effect of overlap amount between recorded spatial modes, the reconstruction quality of VHET is also degraded by the crosstalk generated from the non-target holograms. In Section 4.2, we proposed a spatial mode exchange technique using volume holograms with a phase plate to reduce the overlap amount between the recorded spatial mode, resulting in a high exchange accuracy. As the simulation results show, the overlap ratios between all combinations of the spatial modes are remarkably reduced by VHET combined with a phase plate. Moreover, the maximum crosstalk is improved from 4.8 dB to -8.7 dB. However, compared to the other spatial mode exchanger [7], the crosstalk is expected to further reduce. Therefore, to realize a spatial mode exchanger with low crosstalk, we proposed the scheme of VHET combined with a random optical diffuser. The random optical diffuser is a specific phase plate. It works by creating a random phase profile on the beam front. By scattering the intensity distribution of the recorded spatial modes uniformly using a random optical diffuser, high exchange performance can be attained due to the reduction in the influence of non-targeted holograms. To confirm the basic operation of the proposed method, we perform a numerical simulation of an LP mode group consisting of LP01, LP11, and LP21. In addition, we confirm the dependence of the reconstruction quality on the diffusion angle of the random optical diffuser, which is an essential parameter that restricts the reconstruction quality.

4.3.1 Operational principle

Figure 4.6 shows schematic diagrams of the VHET combined with a random optical diffuser. The operational principle is the same as that of VHET combined with a phase plate stated in Section 4.2. The scheme consists of recording and exchange procedures. During the recording procedure (Fig. 4.6(a)), the multiplexed volume holograms are recorded as fringes resulting from the interference between the writing beam and reference beam. During the exchange procedure (Fig. 4.6(b)), by irradiating the holograms with signal beams, the spatial mode components are diffracted with complex amplitude distributions corresponding to those of the reference beam. To reduce the XTs from the non-targeted holograms, the intensity distribution of the writing beam is diffused uniformly using a random optical diffuser and a lens as a preprocessor in the recording and exchange procedures. As stated above, the diffracted beam D is expressed as

$$D=\eta\sum_{n=1}^{m}a_n(t)\int_0^L\left|A_n'\right|^2 A_r\exp\left[j\varphi_r+jk\left(x\sin\theta+z\cos\theta\right)\right]dz$$

where L is the thickness of the recording medium, η is the diffraction efficiency, and $a_n(t)$ is the time series signal. A_n' and φ_n' (n = 1, 2, …, m) are the amplitude and phase distribution of the converted signal beam, respectively. A_r (x, y, z) is the amplitudes and φ_r (x, y, z) is the phase distributions of the reference beams, respectively; k is the wave number in the recording medium. The spatial mode components of the signal beams are diffracted simultaneously and shaped to fit the complex amplitude distributions corresponding to those of the reference beam. According to the above equation, the diffracted beam is mostly not modulated by the non-targeted holograms because the intensity distribution of the signal beam is converted to $|A_n'|^2$, which is uniformly scattered by the random optical diffuser. Thus, the XT components are suppressed by diffusing the intensity distribution of the signal beam uniformly and by using a random optical diffuser to reduce the effect of the intensity distribution of the signal beam related to the non-targeted holograms. Moreover, as shown in Fig. 4.7, we can improve the exchange accuracy by improving the inhomogeneity of the intensity distribution of the signal beam and the scattered wavefront with a higher diffusion ratio N_{diff}, related to the diffusion angle θ_d of the random optical diffuser. However, upon increasing N_{diff}, the XTs increase as the size of the scattered beam exceeds the imaging range; thus, the information of the signal beam is lost. Therefore, it is also important to confirm the dependence of the reconstruction quality on θ_d.

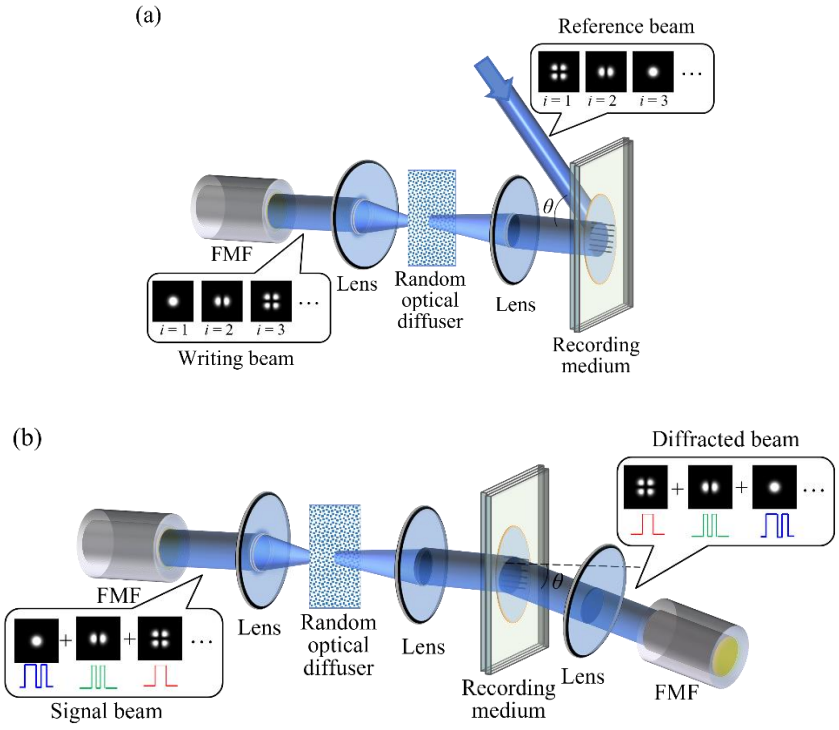

Figure 4.6. Schematic diagram of VHET combined with a diffuser.

(a) Recording procedure. (b) Exchange procedure.

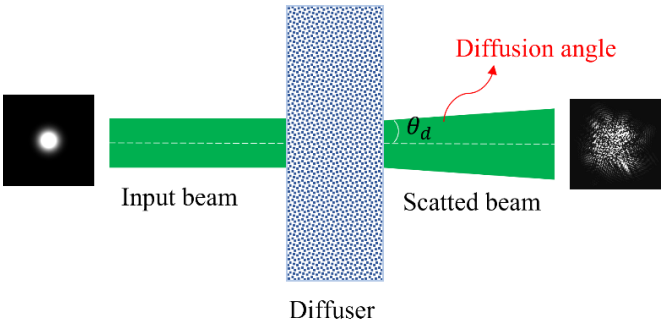

Figure 4.7. Diffusion angle of diffuser.

4.3.2 Simulation model

To validate the basic operation of the proposed scheme, we performed a numerical simulation to model the exchanges within an LP mode group comprising of LP01, LP11, and LP21. The simulation parameters are presented in Table 4.2. We assumed that the wavelength of the light source is 1550 nm. The recording medium was a photopolymer with a thickness of 150 μm, and the incident angle θ was set to 6°. The original mode consists of $N_{dx} \times N_{dy}$ SLM pixels, where N_{dx} and N_{dy} are the number of data pixels along the x and y axes, respectively. Next, the scattered mode is calculated by extending the original mode over a wider region with the diffuser at a diffusion ratio of N_{diff} [13]. Furthermore, the diffuser is composed of $N_{dx}N_{diff} \times N_{dy}N_{diff}$ SLM pixels. Here, the diffusion ratio N_{diff} is defined as the ratio of the sizes of the original and scattered modes, and it is calculated as

$$N_{diff} = \frac{\theta_d + \tan^{-1}(N_{dx}L_{dx} / 2L_f)}{\tan^{-1}(N_{dx}L_{dx} / 2L_f)} \tag{4.9}$$

where θ_d is the diffusion angle of the diffuser, L_{dx} is the pitch of the data pixels, and L_f is the focal length of the Fourier transform lens.

Table 4.2. Simulation Parameters of VHET combined with a diffuser.

Common parameters			
Wavelength of beam source, λ (nm)	1550	Average refractive index, n	1.5
Incident angle of reference beam, θ_r (degree)	6	Number of data pixels, $N_{dx} \times N_{dy}$	32 × 32
Thickness of photopolymer, L_p (μm)	150	Pitch of data pixel, $L_{dx} \times L_{dy}$	Variable
Focal length of Fourier transform lens, L_f (mm)	150	Diffusion angle by diffuser, θ_d (degree)	Variable
Pitch of z-direction, Δz (μm)	1.0	Gray level of random diffuser, G_d (level)	2048

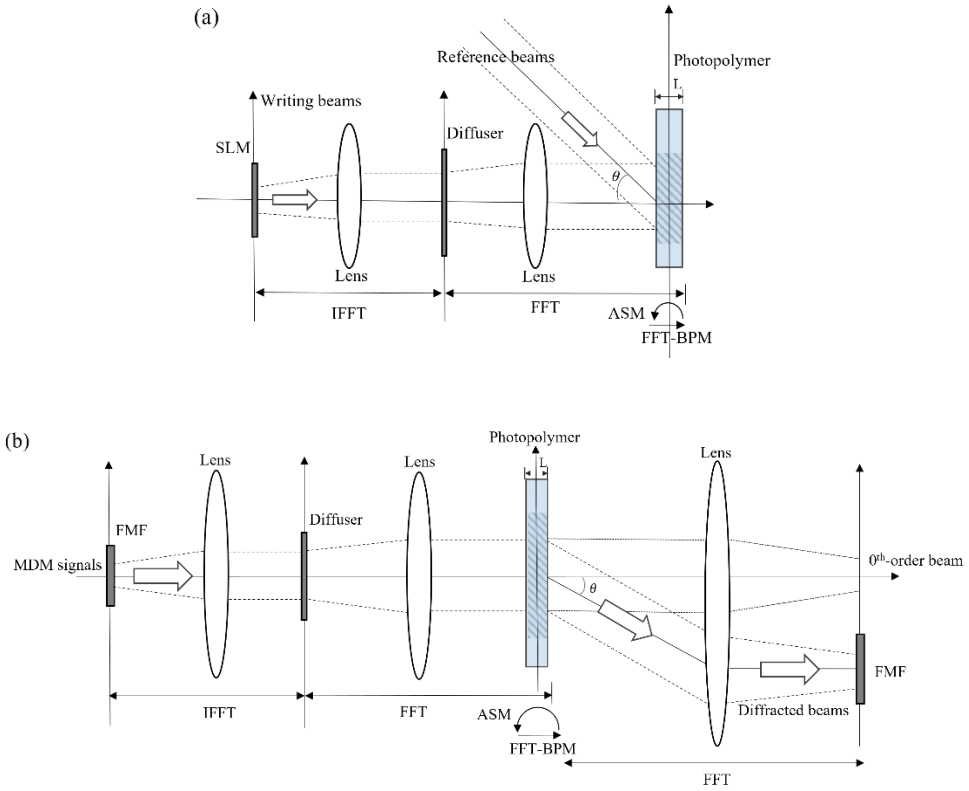

Figure 4.8. Simulation models. (a) Recording procedure. (b) Exchange procedure.

The models and flow of the simulations are shown in Figure 4.8. During the recording procedure (Fig. 4.8(a)), the writing beam is collimated by FFT. The intensity of the writing beam is then modulated by using a random phase distribution. The complex amplitudes on the back surface of the recording medium are then calculated by FFT. Subsequently, the complex amplitudes of the spatial modes on the front surface of the recording medium are acquired using an antidromic ASM. We calculate the refractive index distribution of each layer induced by the interference fringe profile in the photopolymer by FFT-BPM. This process is performed for the number of modes *m*, and the refractive index distribution in the photopolymer is obtained by *m* multiple recordings. During the exchange procedure (Fig. 4.8(b)), the intensity distribution of signal beams is transformed by granting a random phase distribution, and the complex amplitude of the diffracted beam is acquired in the same manner as the recording procedure. Subsequently, the complex amplitude of the diffracted beam received on the FMF plane is calculated by FFT. This process is repeated *m* times.

4.3.3 Simulation results and discussion

To verify the principle of VHET combined with a random optical diffuser, and to confirm the dependence of the exchange performance on the diffusion angle, we performed a numerical simulation between LP01, LP11, and LP21. According to the transmission speed, LP01, LP11a, and LP11b were

changed to LP11a, LP11b, and LP01, respectively. We assume that only three spatial modes, LP01, LP11, and LP21, can be coupled to the second FMF. As mentioned above, of all the XT components generated by the hologram, only the modal components that can be coupled to the FMF remain as XTs. Thus, only the XT components between LP01, LP11, and LP21 were considered. In this simulation, we evaluated the exchange performance based on the CE and XT characteristics.

Figure 4.9 shows the intensity distribution of spatial modes after modulating by a random optical diffuser. Different from the Fig. 4.3, the intensity of spatial modes is scattered uniformly, reducing the crosstalk generated from the non-target holograms. The dependence of CE on the diffusion angle θ_d is shown in Fig. 4.10. These results indicate that the exchange accuracy is improved by increasing the diffusion angle. This is because the inhomogeneity of the intensity distribution of spatial modes is increased, and more information is transferred from the signal beam to the scattered wavefront with an increasing θ_d. When θ_d = 0.55°, the CE tends to saturate. Here, the CE of LP21 is transformed to LP01, and its value decreases as θ_d reaches 0.25°. Subsequently, it begins to increase beyond θ_d = 0.25°. This is because the scattered intensity distribution of LP21 is not considerably uniform, which degrades the exchange accuracy when θ_d is extremely small. We compared these findings to the results from the conventional scheme without the random optical diffuser, and we concluded that the CE was considerably improved for all combinations of the spatial modes for θ_d = 0.25°. Figure 4.11 shows the dependence of the XT characteristics of LP01, LP11, and LP21 on the diffusion angle begins from a value of θ_d = 0.5°. For all values of θ_d beyond 0.55°, the values of XTs were all above -14 dB. These results indicate that the XT characteristics were significantly improved by the proposed scheme. If the size of the scattered beam exceeds the imaging range, it can cause a loss of information of the signal beam and thus deteriorate the reconstruction quality. Thus, to prevent this, the diffusion angle is set to 0.55°. This value of the diffusion angle maximizes the reconstruction quality.

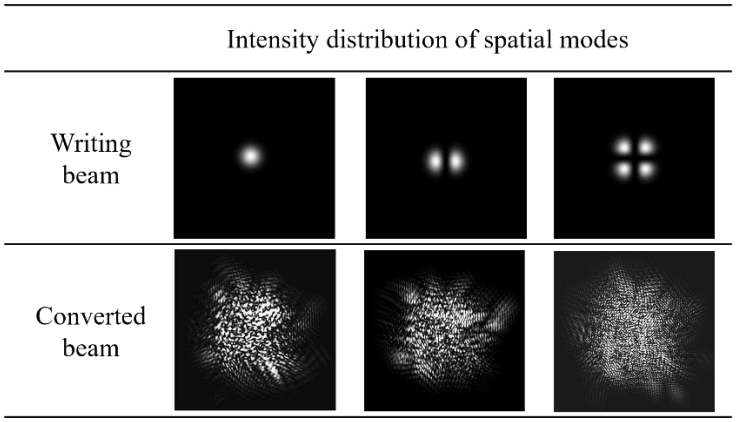

Figure 4.9. Schematic diagram of exchange behavior.

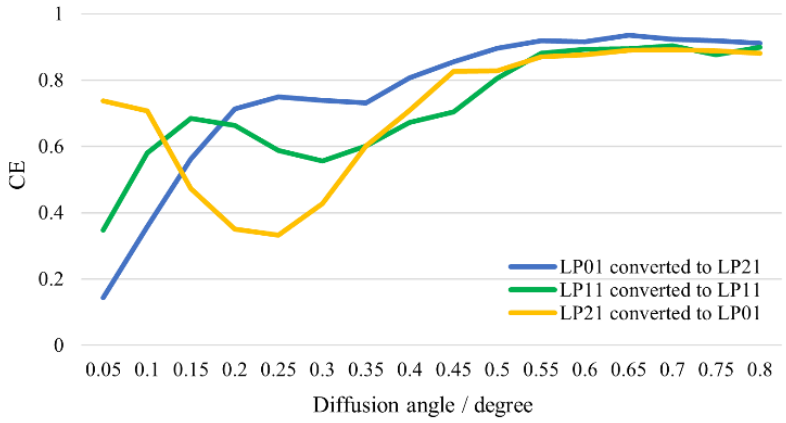

Figure 4.10. CE vs. diffusion angle θ_d.

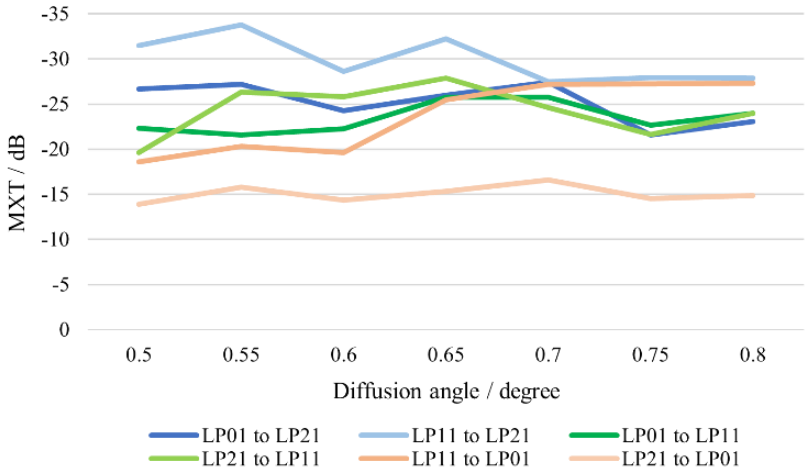

Figure 4.11. XT vs. diffusion angle θ_d.

Under these circumstances, Table 4.3 and Table 4.4 shows the CE and XT characteristics with and without phase modulation. Figure4.12 shows the intensity distribution of the diffracted spatial modes LP21, LP11, and LP01. The size of image is 50×50 pixels. As a result, the intensity peaks of the XT components are reduced compared to the conventional method shown in Fig. 3.8. The intensity distribution of the diffracted mode is close to that of the ideal mode. Moreover, the CE of the signal components is improved beyond 87%, and the CE of the maximum XT components is lower than 2.3%, as shown in Table 4.3. This indicates that the exchange accuracy is significantly improved. Consequently, the maximum XT is improved from 0.4 dB to -15.8 dB, as shown in Table 4.4. As mentioned, the XT components obtained by mode conversion by VHET and those obtained by mode separation by a mode DEMUX differ considerably. Even so, in the output port of the mode DEMUX,

the effect of XT components having the same spatial mode as the signal also decreases, as seen from Table 4.4.

The normalized intensity distribution of the spatial mode after mode exchange with and without phase modulation along the transmission delay time is shown in Fig 4.13. Although the DMD can be reduced by VHET, the pulse width will be expanded. XTs are extremely large and deteriorate the mode exchange accuracy, which affects the compensation of the DMD. In the proposed method, the impulse intensity peaks of the XT components are reduced. The impulse intensity of the diffracted mode is close to that of the ideal mode. These results indicate that the XT components are significantly suppressed in the MDM transmission system, and a high exchange performance can be attained by scattering the intensity distribution of the signal beam using a random optical diffuser. In this way, the DMD can be compensated effectively.

Table 4.3. CE with and without phase modulation.

CE (%)	LP01 (a_i)		LP11 (b_i)		LP21 (c_i)	
	w/o	w/	w/o	w/	w/o	w/
LP01	17.06	87.04	0.02	0.81	18.55	2.30
LP11	0.03	0.61	29.56	88.10	0.02	0.20
LP21	10.61	0.18	0.02	0.04	51.54	91.78

Table 4.4. XT with and without phase modulation.

XT (dB)	LP01 (a_i)		LP11 (b_i)		LP21 (c_i)	
	w/o	w/	w/o	w/	w/o	w/
LP01	-6.9	-27.2	-30.1	-21.6	0	0
LP11	-35.5	-33.8	0	0	-30.3	-20.3
LP21	0	0	-32.2	-26.3	0.4	-15.8

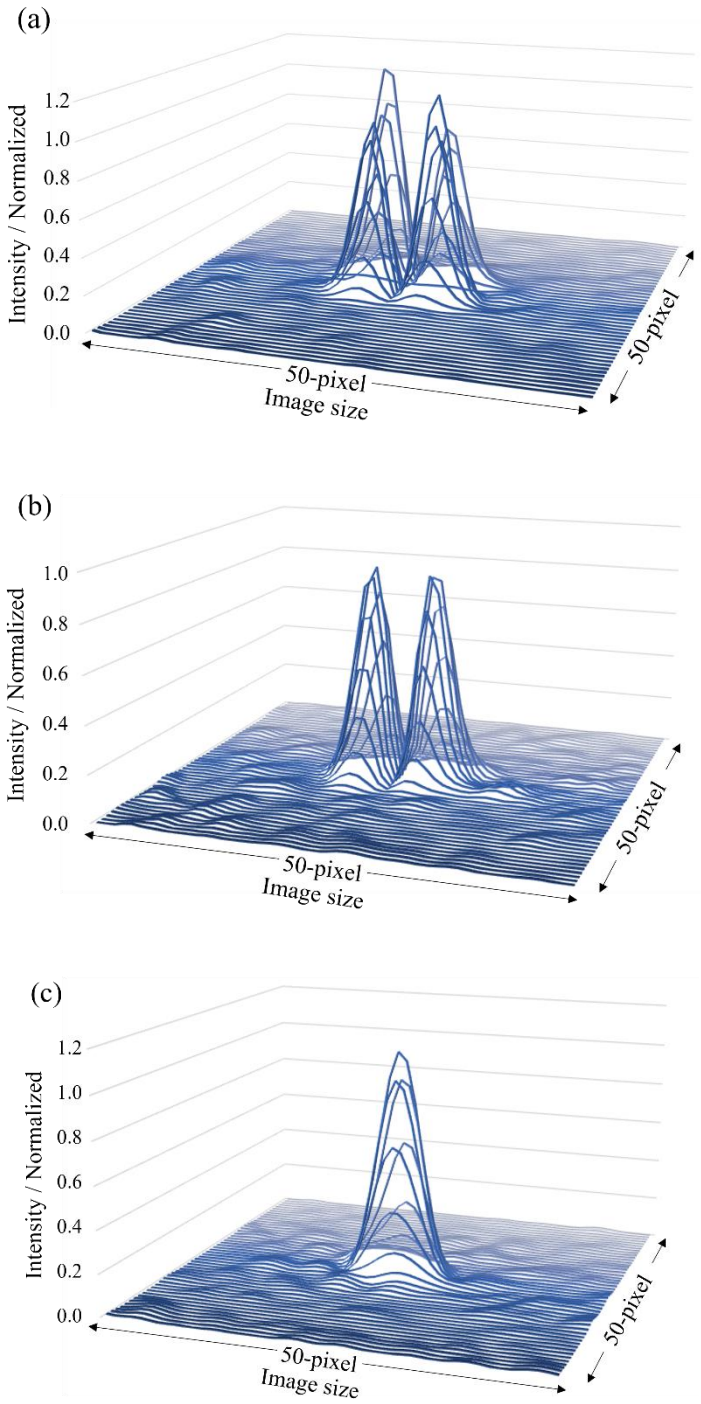

Figure 4.12. Intensity distribution of spatial modes with phase modulation.

(a) LP21. (b) LP11. (c) LP01.

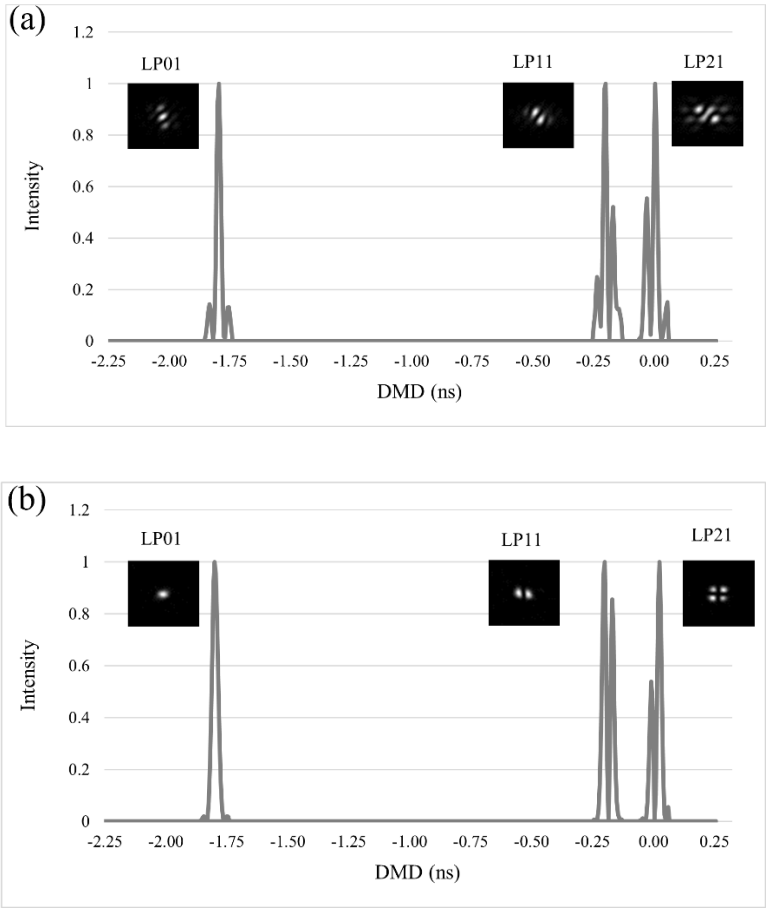

Figure 4.13. Intensity distribution of modes along delay time.
(a) without and (b) with phase modulation.

4.4 Mode diffusion technique in VHET

In the previous sections, we proposed a VHET combined with a phase plate to improve the reconstruction quality. The overlap ratio and crosstalk are markedly improved by the proposed method. However, these methods cannot reduce such crosstalk with phase equivalent to data page information. In this work, a mode diffusion technique [1] using random optical diffusers for crosstalk reduction is applied in VHET to improve the exchange performance. The inter-page crosstalk shown in Fig. 4.14, can be removed by separating the signal and crosstalk components because of the propagation angle difference. Numerical simulations of the exchange behavior between LP01, LP11, and LP21 are performed to confirm the basic operation and compensation efficiency. In addition, we confirm the dependence of the reconstruction quality on the diffusion angle, which is an essential parameter that restricts the reconstruction quality.

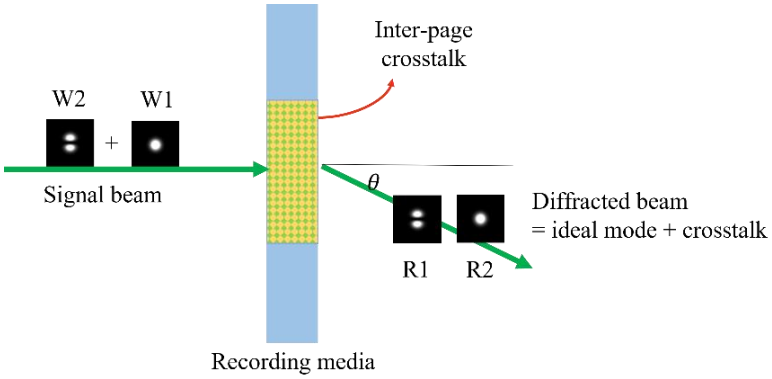

Figure 4.14. Generation of inter-page crosstalk.

4.4.1 Operational principle

Figure 4.15 shows the schematic of VHET combined with the mode diffusion technique. The scheme consists of recording and exchange procedures. The basic principle for suppressing the crosstalk is as follows: during the recording procedure, the intensity of the reference beam is scatted by through a random optical diffuser. The propagation angle of the reference beam is widely spread. During the exchange procedure, the scatted diffracted beam, including the signal and inter-page crosstalk components, repasses through the diffuser whose profile is conjugate with that of in the recording procedure. The original signal distribution recovers owing to the cancellation effect of the phase modulation. The crosstalk is spread widely owing to the lack of phase correlation with the diffuser. In this way, inter-page crosstalk components can be suppressed. During the recording procedure (Fig. 4.15(a)), the writing beam is vertically incident on the recording medium and propagates along the *z*-axis. The reference beam forms an angle θ with the *z*-axis. Thus, for the i^{th} hologram, the writing beam W_i (i = 1, 2, …, m) and reference beam R_{m-i+1} are expressed as equations 4.1 and 4.2.

$$W_i = A_i(x, y, z)\exp[jkz + j\varphi_i(x, y, z)]$$

$$R_{m-i+1} = A_r(x, y, z)\exp[jk(x\sin\theta + z\cos\theta) + j\varphi_r(x, y, z)]$$

where A_i (x, y, z) and A_r (x, y, z) are the amplitudes and φ_i (x, y, z) and φ_r (x, y, z) are the phase distributions of the writing and reference beams, respectively; k is the wave number in the recording medium. Then, the reference beam is modulated by a random optical diffuser installed in the Fourier plane, and the propagation angle of the reference bema is widely spread. It is noted that different from the improvement methods proposed in Sections 4.2 and 4.3, we modulate the phase distribution of reference beams instead of recorded signal beams in this work. The scatted reference beam R_{m-i+1}' is expressed as

$$R'_{m-i+1} = A'_r(x,y,z)\exp[jk(x\sin\theta + z\cos\theta) + j\varphi_r(x,y,z) + j\varphi_d(x,y,z)] \tag{4.10}$$

where $A_r'(x, y, z)$ is the amplitude of the diffused reference bean. $\varphi_d(x, y, z)$ is the phase distribution of the random optical diffuser. The complex amplitude transmittance $T(x, y, z)$ of the recorded holograms of the writing beam and scattered reference beam is expressed as

$$\begin{aligned} T(x,y,z) = \sum_{i=1}^{N} A'_r(x,y,z)A_i^*(x,y,z)\exp[j(\varphi_r(x,y,z) + \varphi_d(x,y,z) - \varphi_i(x,y,z)) \\ + jkx\sin\theta + jkz(\cos\theta - 1)] \end{aligned} \tag{4.11}$$

where * denotes a complex conjugate. During the exchange procedure (Fig. 4.15(b)), by irradiating the multiplexed holograms with the signal beams, the spatial mode components are diffracted with complex amplitude distributions corresponding to those of the scattered reference beams, and they are expressed as

$$\begin{aligned} D &= \eta\int_0^L TSdz \\ &= \eta\sum_{n=1}^{m}\sum_{i=1}^{m}\int_0^L a_n(t)A_nA_i^*A'_r\exp\left[j\left(\varphi_n - \varphi_i + \varphi_r + \varphi_d\right) + jk\left(x\sin\theta + z\cos\theta\right)\right]dz \end{aligned} \tag{4.12}$$

where L is the thickness of the recording medium, η is the diffraction efficiency, and $a_n(t)$ is the time series signal. A_n and φ_n ($n = 1, 2, \ldots, m$) are the amplitude and phase distribution of the signal beam, respectively. When $n = i$, the spatial mode component is converted to a beam, of which, the spatial phase corresponds to that of the scattered reference beam and is strongly diffracted in the direction of θ. When $n \neq i$, the mode fields between the writing beams and signal beams are mismatched, and the spatial mode components are weakly diffracted as crosstalk components. Consequently, the scattered diffraction beam D is expressed as follows:

$$D_d = \eta\sum_{n=1}^{m} a_n(t)\int_0^L \left\{|A_n|^2 A'_r\exp[j(\varphi_r + \varphi_d) + jk(x\sin\theta + z\cos\theta)] + A_c\exp(j\varphi_c)\right\}dz \tag{4.13}$$

where A_c is the amplitudes and φ_c is the phase distributions of the crosstalk components, respectively. The spatial mode components of the signal beams are diffracted simultaneously at the incident angle of the reference beams. When the scattered diffracted beam contains both the scattered signal components and the crosstalk components repassed through the random optical diffuser whose profile is conjugate with that of in the recording procedure, the scattered signal components are recovered owing to the cancellation effect of the phase modulation. The crosstalk components are separated from the signal components and spread widely owing to the lack of phase correlation with the diffuser. The diffracted beam is expressed as

$$D = A_r \exp[j\varphi_r + jk(x\sin\theta + z\cos\theta)] + A_c \exp[j(\varphi_c - \varphi_d)] \tag{4.14}$$

The signal components are then extracted by a pinhole. The crosstalk components are suppressed by the proposed method as the signal and crosstalk components get separated from the propagation angle difference.

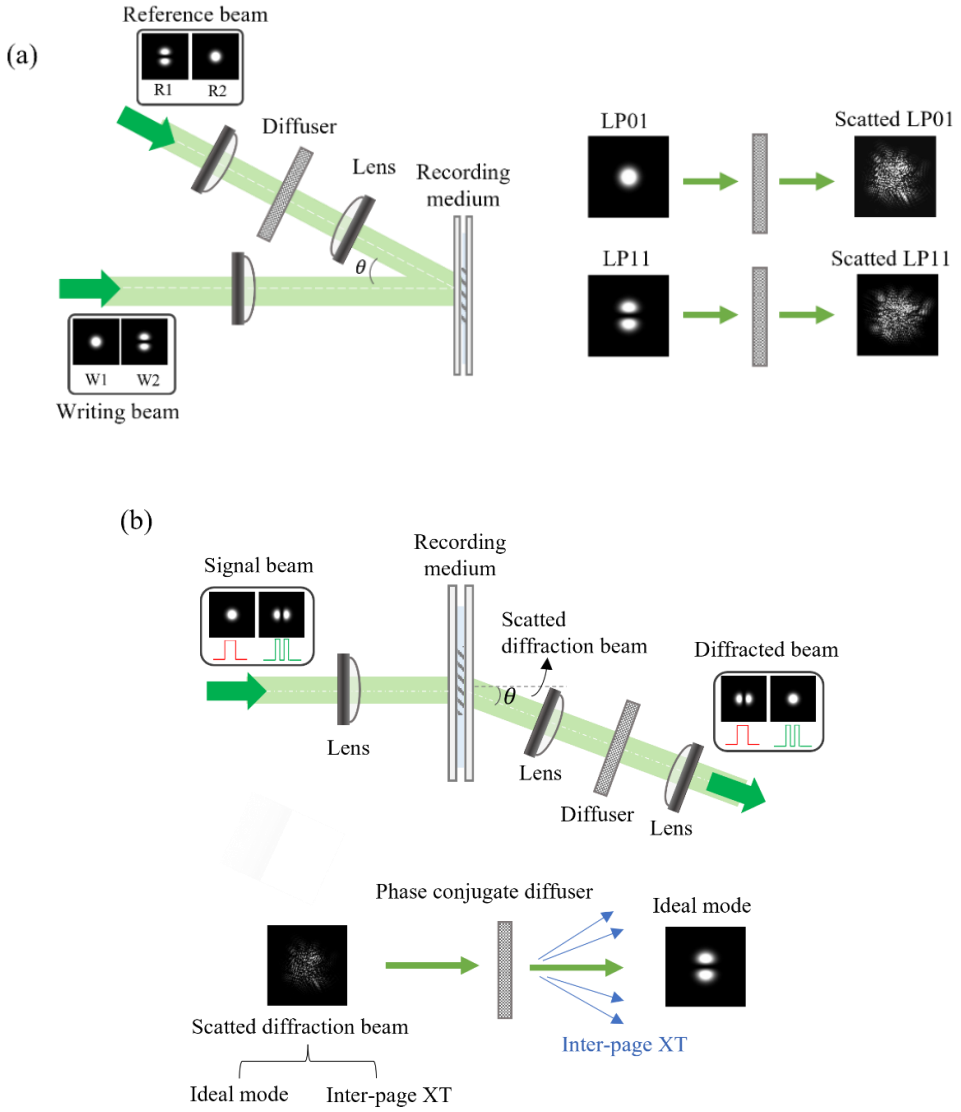

Figure 4.15. Schematic diagrams of VHET combined with mode diffusion technique. (a) recording procedure and (b) exchange procedure.

4.4.2 Simulation model

To validate the basic operation of the proposed method, we performed a numerical simulation of an LP mode group comprising LP01, LP11, and LP21 with different transmission speeds. The simulation parameters are presented in Table 4.5. We assumed that the wavelength of the light source is 1550 nm. The recording medium was a photopolymer with a thickness of 150 μm, and the incident angle θ was set to 6°. Figure 4.16 shows the simulation model of VHET combined with the mode diffusion technique. The simulation model is divided into two main steps, the recording procedure (Fig. 4.16(a)) and the exchange procedure (Fig. 4.16(b)). The recording procedure includes writing beam generation and reference beam generation. During the recording procedure, the complex amplitudes of the spatial modes are generated as the writing beam and reference beam with an oblique phase corresponding to the incident angle θ in the Fourier space, and they are collimated by FFT. Subsequently, as shown in Fig. 4.16(a), the intensity of the reference beam is transformed using a random phase distribution by granting it a random phase distribution. The complex amplitudes on the back surface of the recording medium are then calculated by FFT. Subsequently, the complex amplitudes of the spatial modes on the front surface of the recording medium were acquired using an antidromic ASM. We calculated the refractive index distribution of each layer induced by the interference fringe profile in the photopolymer using FFT-BPM. This process was performed for the number of modes m, and the refractive index distribution in the photopolymer was obtained by m multiple recordings.

During the exchange procedure (Fig. 4.16(b)), the complex amplitude of the spatial modes, which is consistent with the writing beams, is generated as the MDM signals. The complex amplitude of the diffracted beam is acquired in the same manner as the recording procedure. Then, the multiplication between the scattered diffracted beam and diffuser transmittance function is performed in the Fourier plane. Here, it is noted that the phase conjugation is computed by inverting the sign of the phase of the diffuser that used in the recording procedure. Finally, the scattered reference beam is recovered in the Fourier plane by FFT. This process was repeated m times.

Table 4.5. Simulation Parameters of VHET combined with mode diffusion technique.

Common parameters			
Wavelength of beam source, λ (nm)	1550	Average refractive index, n	1.5
Incident angle of reference beam, θ_r (degree)	6	Number of data pixels, $N_{dx}\times N_{dy}$	32×32
Thickness of photopolymer, L_p (μm)	150	Pitch of data pixel, $L_{dx}\times L_{dy}$	Variable
Focal length of Fourier transform lens, L_f (mm)	150	Diffusion angle by diffuser, θ_d (degree)	Variable
Pitch of z-direction, Δz (μm)	1.0	Gray level of random diffuser, G_d (level)	2048

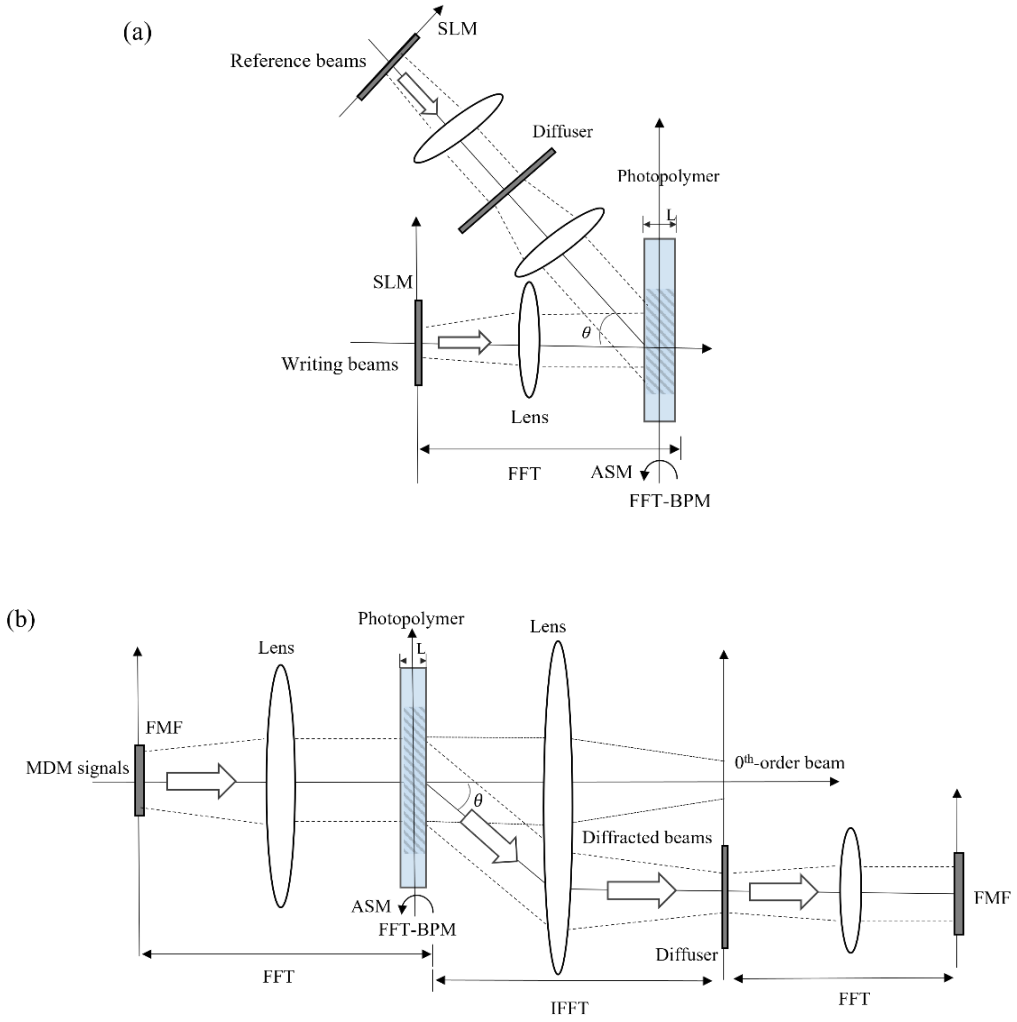

Figure 4.16. Simulation models. (a) Recording procedure. (b) Exchange procedure.

4.4.3 Simulation results and discussion

We performed numerical simulations for the exchange behavior between two spatial modes LP01 and LP11 at first to confirm the dependence of the reconstruction quality on the diffusion angle of the random optical diffuser. The reconstruction accuracy by calculating the coupling efficiency and crosstalk characteristics. The dependence of CE on the diffusion angle θ_d is shown in Fig. 4.17. These results indicate that the reconstruction accuracy is improved by increasing the diffusion angle, because the signal component and crosstalk components are separated by the propagation angle difference produced by the random optical diffusers. When θ_d is beyond 0.5°, the CE slightly decreases and then tends to saturate. This is attributed to the size of the scattered beam exceeding the captured imaging range, it can cause a loss of information of the signal and thus deteriorate the reconstruction quality. It is noted that when the diffusion angle of diffuser is extremely small, the CEs are lower than that of the conventional method. This is because the scattered intensity distribution of spatial modes is not

considerably uniform, which degrades the exchange accuracy. The dependence of the XT characteristics of the diffracted beams on the diffusion angle is shown in Fig. 4.18. These results indicate that the value of XT is improved by increasing the diffusion angle. Subsequently, XTs both begins to deteriorate when $\theta_d = 0.5°$ which is in accordance with the results of CE. Thus, in theory, the separation performance is improved by increasing the diffusion angle to increase the propagation angle difference; but the information of signal components will be lost as the size of the scattered signal components exceeds the captured imaging range, resulting in the low reconstruction quality. Thus, considering both the coupling efficiency and crosstalk characteristics, the diffusion angle is set to 0.5° to maximize the reconstruction quality. Figure 4.19 shows the intensity distribution of scattered incident mode LP11 and diffraction mode LP01. The intensity distributions of LP11 show that increasing the diffusion angle increases the inhomogeneity of the intensity distribution of the reference beam. The intensity distributions of LP01 show that the intensity peaks of the XT components are reduced by increasing the diffusion angle. When $\theta_d = 0.5°$, the intensity distribution of the diffracted beam is close to that of the ideal desire mode. As mentioned, the reconstruction quality can be improved by adjusting the diffusion angle of the random optical diffuser. The CE is drastically improved beyond 0.8, and the MXT is significantly suppressed to -23.1 dB for $\theta_d = 0.5°$.

Moreover, we performed the exchange behaviors between LP01, LP11, and LP21. In this simulation, LP01, LP11, and LP21 are changed to LP21, LP11, and LP01, respectively. Figure 4.21 shows the intensity distributions of the diffracted beam with (w/) and without (w/o) the mode diffusion technique. Compared with the conventional method, the intensity peaks of the crosstalk components are spread widely owing to the lack of phase correlation with the random optical diffuser, and the intensity distribution of the diffracted mode is close to that of the ideal mode by the proposed method. Moreover, the CEs are improved remarkably for all combinations of the spatial modes, and the maximum crosstalk is also significantly suppressed from 0.4 to -14.7 dB. When converting from LP11 to LP11, crosstalk increases because the amount of overlap between the scattered LP11 and original LP11 is reduced during recording; thus, the scattered LP11 as the reference object cannot match the original LP11 as the writing object perfectly. Nonetheless, the overall exchange performance improved compared with that of the conventional method, which indicates that the crosstalk components are significantly suppressed. A high reconstruction quality can be attained by separating the signal and crosstalk components from the propagation angle difference using the mode diffusion technique. Consequently, the CE is significantly improved by more than 78%, and the maximum crosstalk is suppressed to -14.7 dB.

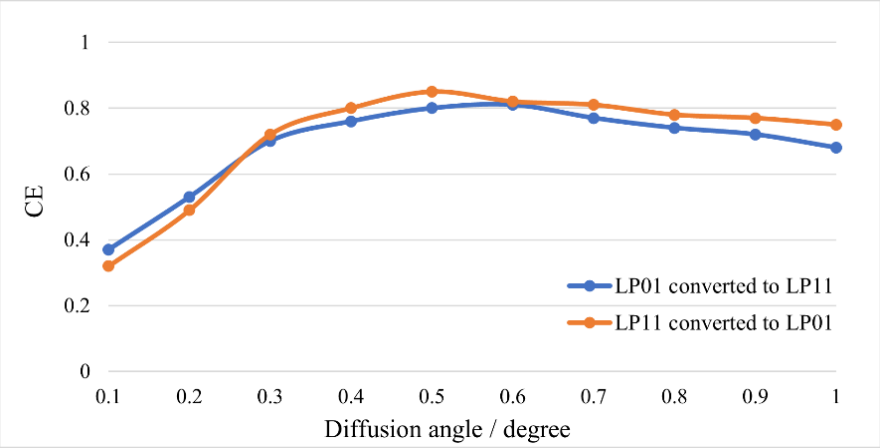

Figure 4.17. CE vs. diffusion angle θ_d.

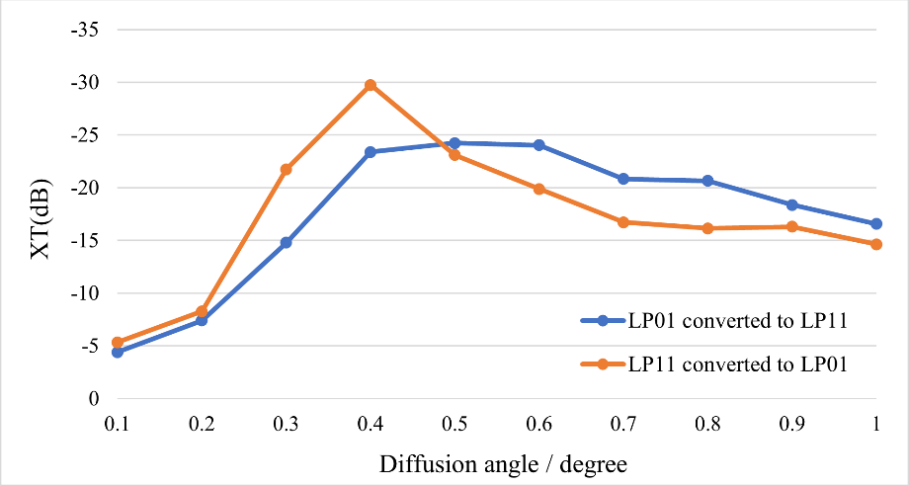

Figure 4.18. XT vs. diffusion angle θ_d.

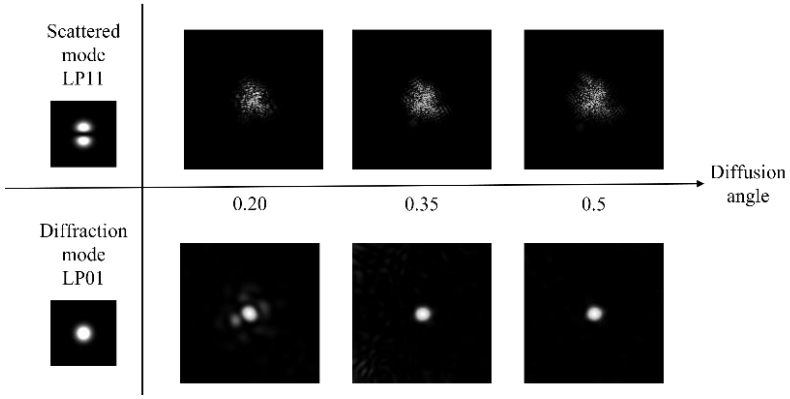

Figure 4.19. Intensity distribution of the diffraction beam vs. diffusion angle θ_d.

Diffracted beam			Coupling efficiency		Maximum crosstalk (dB)	
Ideal mode	w/o	w/	w/o	w/	w/o	w/
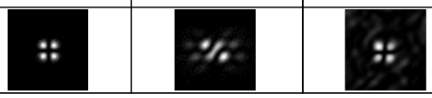			52%	82%	-6.9	-18.2
LP01 converted to LP21						
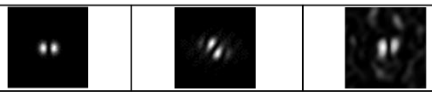			30%	78%	-30.1	-14.7
LP11 converted to LP11						
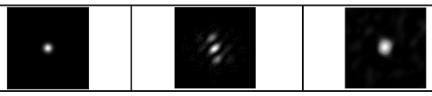			17%	91%	0.4	-19.5
LP21 converted to LP01						

Figure 4.20. Simulation results with and without the mode diffusion technique.

4.5 Summary

In this chapter, we proposed three improved methods for combing volume holograms with phase plates to ameliorate the reconstruction quality without significantly increasing the number of optical elements. To confirm the basic operation of the proposed method, mode-exchange numerical simulations were conducted using an LP mode group comprising of LP01, LP11, and LP21. In VHET combined with a phase plate, the intensity of the signal beam was modulated by a phase plate. The overlap ratio between LP01 and LP11 was remarkably reduced from 0.49 to 0.26. The crosstalk was reduced from -1.49 dB to -23.5 dB. In VHET combined with a random optical diffuser, the intensity distribution of the signal beam is scattered uniformly by a random optical diffuser; this results in a high exchange performance. We then confirmed the dependence of the reconstruction quality on the diffusion angle during an attempt to acquire a better exchange performance. As a result, the CE was improved beyond 87%, and the maximum XTs were significantly suppressed to -15.8 dB. In VHET combined with the mode diffusion technique, the inter-page crosstalk can be removed by separating the signal and crosstalk components due to the propagation angle difference. The signal components can be recovered owing to the cancellation effect of the phase modulation and the crosstalk components were spread widely owing to the lack of phase correlation with the random diffuser. Moreover, by adjusting the diffusion angle of the random optical diffuser, the CE was improved beyond 78%, and the maximum XT was significantly suppressed to -14.7 dB. Comparing these three improvement methods, the exchange performance of VHET combined with a random optical diffuser is best according to the CE and XT characteristics. However, there are several factors that should be considered when the random optical diffused is applied to VHET. The visibility of the inference fringes recorded in the recording medium will become weak because the intensity of the light beam is scattered uniformly by a random optical diffuser. Moreover, power loss is a critical

problem because the light beam is scattered in free space. It is essential to compensate for optical power by other means. Besides, phase matching is required during the recording and exchange procedure. In summary, the exchange performance can be improved by proposed methods.

References

[1] A. Shibukawa, A. Okamoto, Y. Wakayama, A. Tomita, H. Funakoshi, and K. Sato, “Digital image diffusion technique for suppressing interpage crosstalk in holographic data storage,” Jpn. J. Appl. Phys. **52**, 09LD03 (2013).

[2] S. Shimizu, A. Okamoto, F. Mizukawa, K. Ogawa, A. Tomita, T. Takahata, S. Shinada, and N. Wada, “Spatial mode demultiplexing technique using angularly multiplexed volume holograms with a phase plate,” Jpn. J. Appl. Phys. **56**, 09NA05 (2017).

[3] Y. Wakayama, A. Okamoto, K. Kawabata, A. Tomita, and K. Sato, “Mode demultiplexer using angularly multiplexed volume holograms,” Opt. Express, **21**(10), 12920-12933 (2013).

[4] T. Oda, A. Okamoto, D. Soma, A. Tomita, and Y. Wakayama, "All-optical demultiplexer based on dynamic multiple holograms for optical MIMO processing and mode division multiplexing," Proc. SPIE 7958, 79580J (2011).

[5] K. Matsushima, H. Schimmel, and F. Wyrowski, “Fast calculation method for optical diffraction on tilted planes by use of the angular spectrum of plane waves,” J. Opt. Soc. Am. A, **20**(9), 1755-1762 (2003).

[6] J. Tanaka, A. Okamoto, and M. Kitano, “Development of Image-Based Simulation for Holographic Data Storage System by Fast Fourier Transform Beam-Propagation Method,” Jpn. J. Appl. Phys., **48**(3), 03A028 (2009).

[7] Y. Wakayama, D. Soma, K. Igarashi, H. Taga and T. Tsuritani, “Intermediate mode interchange for reduction of differential mode-group delay in weakly-coupled 6-mode fiber transmission line,” Proc. OFC2016, M3E.6 (2016).

[8] S. Zhang, A. Okamoto, T. Shiba, H. Hayashi, K. Ogawa, A. Tomita, T. Takahata, S. Shinada, Y. Goto, and N. Wada, "Spatial mode exchange technique using volume holograms with a random optical diffuser to reduce modal cross-talks," Proc. SPIE 11309, 1130909 (2020).

Chapter 5

Spatial-light-modulator-based optical-fiber joint switch for few-mode multicore fiber

5.1 Introduction

In space-division multiplexing (SDM) [1-3]transmission systems, few-mode multicore fibers (FM-MCFs), known as multicore fibers with few-mode cores, have considerable potential for meeting the large capacity and spatial-channel counts, thus enabling optical fibers with over 100 spatial channels and total bit rates over 10 Pbit/s when using both the C and L bands [4]. In the FM-MCF transmission systems, spatial channels are susceptible to crosstalk between multiple parallel transmission paths, thereby limiting system capacity. Although multiple-input multiple-output signal processing techniques can compensate for crosstalk, it is essential to ensure that all spatial channels are routed together as a unit from the transmitter to receiver [5]. Thus, integration and implementation cost of the switching elements are decisive factors in SDM networks [6,7]. To realize economical, high-capacity, and energy-efficient optical networks, the optical-fiber joint switch (OFJS) is proposed herein to connect and switch all the spatial channels of an optical network to improve the integration without electrical signal regeneration. Moreover, OFJS must maintain the complex amplitude distributions of all spatial modes in all cores while routing signals from the input FM-MCF in a certain direction. In recent years, liquid-crystal-on-silicon (LCoS) spatial light modulators (SLM) have been used for optical signal processing and signal monitoring because of their high spatial resolutions, high light efficiencies, and phase-only modulation capabilities [8]. Considering the realization requirements, routing flexibility, and scaling potential, an SLM-based OFJS for FM-MCFs is proposed in this work.

The SLM-based OFJS is a cost-effective integration technique with a simple configuration that can switch all signal paths of the FM-MCF as a unit in an optical free space to obtain a greater throughput; in addition, it can achieve selective operation by changing the display patterns. Unlike the OFJS applied in SMF transmission systems, internal crosstalk and port crosstalk are serious issues that must be considered in FM-MCF transmission systems. The internal crosstalk can be divided into intermodal crosstalk caused by mode coupling and intercore crosstalk caused by adjacent cores. The port crosstalk is defined as the light intensity that is leaked to and coupled into non-selected output ports, and it is

divided into device-level and system-level crosstalk [9].

To confirm the feasibility of SLM-based OFJS for FM-MCFs, in Section 5.2, we demonstrate its operating principle. In Section 5.3, we perform numerical simulations by jointly switching optical signals. In Section 5.4, we present experiments with switching signal paths for a 6-mode 19-core fiber (6M-19CF) using an LCoS-SLM and measuring the intensity of the diffracted light and mode-field pattern after switching. In Section 5.5, the experiments of changing the positions of output ports are performed to reduce the port crosstalk. In Section 5.6, we summarize and discuss the research results and prospects of this work.

5.2 Operational principle of OFJS based on phase-SLM

The LCoS-SLM utilizes the electrically modulated optical properties of liquid crystals to modulate the amplitude, phase, or polarization of the input light signal. Compared with amplitude modulation of the input light in LCoS-SLM, phase modulation is preferred for better light usage efficiency in an SDM system. Figure 1 shows the schematic of the FM-MCF joint switch based on the reflective phase-only SLM (PSLM) using a standard Fourier transform arrangement. The SLM and input/output ports are placed at the front and back focal planes of a collimating lens of focal length *f*. Since the OFJS system follows a standard Fourier transform setup along the switching axis, the input light signal is diffracted and refocused on the target output port by the phase-only blazed grating written on the LCoS. As shown in Fig. 5.1, the light signal emitted from the FM-MCF is collimated by the optical Fourier transform (OFT) scheme through a lens. Then, the collimated light is modulated by the phase-only blazed grating on the LCoS display, which is placed along the Fourier plane of the 4-*f* system, and routed in a specified direction by oblique phase distribution corresponding to the target grating pattern. Since the angular separation is transformed to spatial separation by a lens, the modulated light signal received at the output port is retrieved by an optical inverse Fourier transform (OIFT). Here, as shown in Fig. 5.2, when the light signal is modulated by the phase pattern A on the LCoS display, the modulated light signal is routed to output port A. When the phase pattern changes to B at the LCoS display, the modulated light signal is routed to output port B. Thus, the input light signal is selectively routed to the target output port by SLM-based OFJS.

In the proposed method, the input light signal is linearly polarized parallel to the liquid-crystal display and switched by the phase-only blazed grating on the LCoS. The diffraction angle is generated by display blazed gratings with different phase levels added to each pixel, which cause phase retardation with respect to the propagation direction. Since the light signal is jointly switched, it is essential to ensure a uniform diffraction angle for the entire light spectrum. As noted above, the internal and port crosstalks are serious issues that must be considered in the OFJS system. The internal crosstalk is an important phenomenon in FM-MCFs, and the crosstalk impairment accumulates as the transmission distance increases. At the device level, port crosstalk is closely related to the diffraction

efficiency of the blazed grating written on the LCoS, such as the fringing field effect [10,11]. Owing to phase modulation of the SLM being mostly LC-based, when the optical phase is controlled spatially by the voltage level applied to each pixel, the LC directors near the pixel edges are distorted by the lateral components of the fringing field to prevent abrupt spatial variations in phase modulation. Severe fringing field effects will thus degrade the reflectance significantly, specifically for the ultrahigh-resolution LCoS. At the system level, the crosstalk is related to the coupling characteristics of the light signals corresponding to the output fiber positions, field spots on the LCoS, and grating pitch, among others [9]. In this study, we focus on the port crosstalk at the system level to improve the efficiency of fiber joint switching.

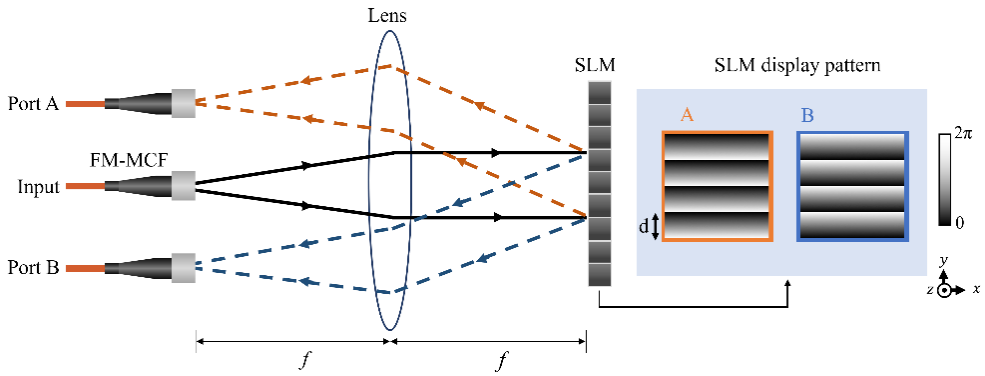

Figure 5.1. Schematic of the SLM-based FM-MCF joint switch.

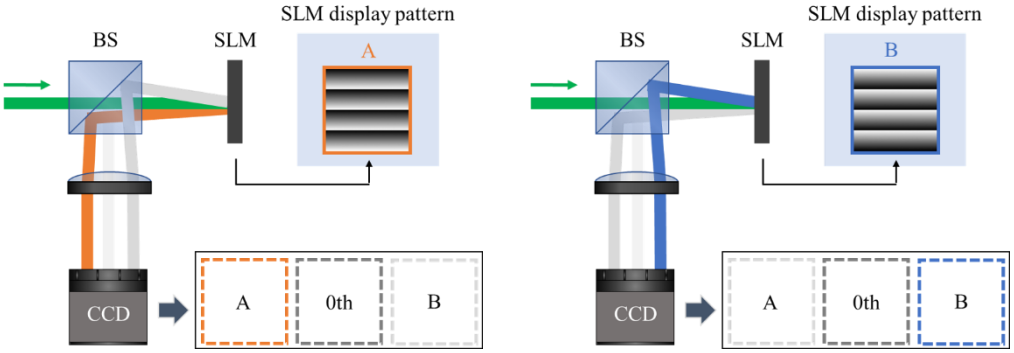

(a) (b)

Figure 5.2. Selectively switching by SLM. (a) Port A. (b) Port B.

5.3 Numerical simulation

5.3.1 Simulation model

To validate the basic operation of the proposed method, we performed numerical simulations to model the switching within a 6M-19CF comprising six linearly polarized (LP) modes (LP_{01}, LP_{11a}, LP_{11b},

LP_{21a}, LP_{21b}, and LP_{02}). The simulations were performed by switching the signal paths by granting diffraction angles to the light signals emitted from the 6M-19CF using an SLM, as shown in Fig. 5.3. The cross section of the 6M-19CF is shown in Fig. 5.4, and the simulation parameters are presented in Table 5.1. Owing to the simulation involving a linear system, we simulated each core separately to simplify the numerical analysis. As mentioned above, the input light signal is collimated through a lens, and the phase modulation by the SLM for switching the signal path was performed with a blazed grating pattern on the LCoS. Assuming that the horizontal pixel pitch and number of pixels of the SLM display are D_x and N_x, respectively, the diffraction angle θ_d can be expressed as

$$\theta_d = \pm \sin^{-1}\left(\frac{\lambda}{nD_x}\right) \quad \left(2 \le n \le N_x\right) \tag{5.1}$$

where λ is the wavelength. We assume that the wavelength of the light source is 1550 nm, and D_x and N_x are 10 nm and 512, respectively. The maximum angle of diffraction is 4.45°. Thus, in this simulation, the diffraction angle is set to 2.2° in the horizontal direction to avoid exceeding the captured range of the output light signal. When the diffraction angle is set to 2.2°, the blazed phase-stepped grating is divided into eight equidistant phase steps, and the maximum phase depth is 2π rad. However, when the input light signal is diffracted and refocused on the target output port at the desired angle by the blazed grating on the LCoS, the components other than the main diffracted light are generated as crosstalk owing to the imperfections of the hologram on the LCoS. Here, we ignore the influence of the imperfections of the hologram on the LCoS and assume that all components are modulated by the ideal SLM. To briefly show the effects of the OFJS, we only analyze and discuss the components of the outer core (core 1), inner core (core 13), and center core (core 19). To evaluate the switching accuracy, we calculate the coupling efficiency (CE) between the complex amplitude of the path-switched light and that of the desired ideal mode. The CE of i^{th} (i =1, 2, …, 6) spatial mode of the output light is calculated by

$$CE_i = \left| \iint E_i^*(x,y) E_{id}(x,y) dxdy \right|^2 \tag{5.2}$$

where * denotes the complex conjugate. Note that $E_i(x,y)$ and $E_{id}(x,y)$ are the complex amplitude distributions of the path-switched output signal beam and i^{th} ideal desired mode, respectively.

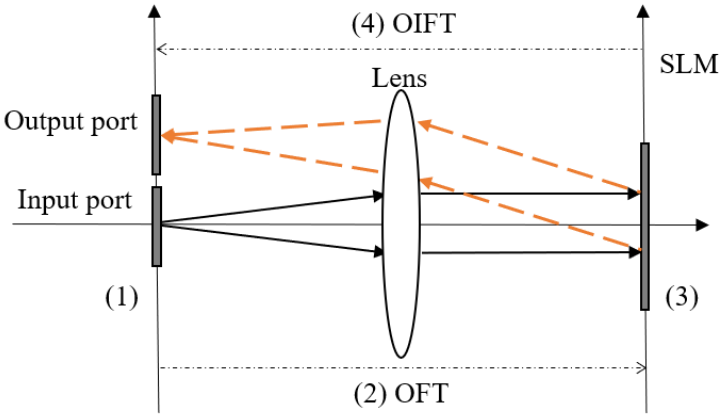

Figure 5.3. Simulation model showing the overviews of the following processes: (1) set complex amplitude of each mode; (2) calculate complex amplitude on the SLM plane using OFT; (3) multiply the complex amplitude of the mode and phase pattern of SLM in Fourier space; (4) calculate the complex amplitude of the mode on the output plane using OIFT. Processes (1)–(4) are repeated for all modes.

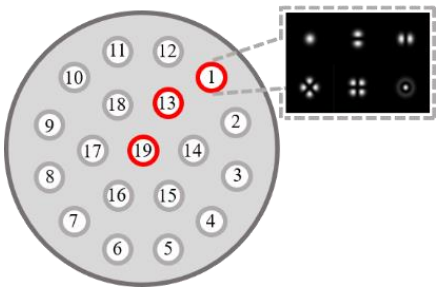

Figure 5.4. Cross section of the 6M-19CF.

Table 5.1. Simulation parameters of OFJS.

Common parameters			
Wavelength of beam source, λ	1550 nm	Diffraction angle, θ_d	2.2°
SLM pixel size, D_x	10 μm	Number of samples	1024 × 1024
Number of SLMs, $N_x \times N_y$	512 × 512	Pixel size on fiber plane	0.45 μm
Core diameter of fiber	18.4 μm	Core pitch	51.2 μm
V number of fiber	7.78	Shift amount on output plane (x axis)	57.6 μm

5.3.2 Simulation results and discussion

For a given set of simulation conditions, the simulation results of core 1, core 13, and core 19 are similar, with only slight differences. Thus, we discuss only the simulation results of core 19 after switching, as shown in Table 5.2. The coupling efficiency between the same spatial modes in each

core was approximately -0.8 dB, indicating that the light signals were efficiently routed to the target output ports. Regarding the relationships between these results, the coupling efficiency between signal modes A and B is the same as that between signal modes B and A. The coupling efficiency relationships for the modes are thus symmetrical. However, the coupling efficiencies in the case of LP_{11a} and LP_{11b} are similar because they are the degenerate modes orthogonal to each other by rotation of the LP mode. Moreover, although LP_{21a} and LP_{21b} have the same orthogonal characteristics, there are large discrepancies in their coupling efficiencies for LP_{01} and LP_{02}. This is attributed to the pattern size being set to an even value in the simulations; thus, the phase pattern of LP_{21a} is asymmetric when generating the phase profile. Nonetheless, the discrepancies in the coupling efficiencies between LP_{21a} and LP_{21b} may not affect the analysis of simulation results significantly. From the simulation results, we observe that the coupling efficiencies between the same spatial modes are approximately -0.8 dB each and that the maximum coupling efficiency is -21.1 dB, which indicates that SLM-based OFJS enables switching the signals emitted from each of the cores. However, the crosstalk between adjacent cores is a crucial factor that needs to be considered because a portion of the optical power launched into one of the cores may be coupled with the adjacent cores during propagation. In the simulation, the coupling efficiency between the adjacent cores was less than -300 dB, indicating that the core crosstalk was negligibly small. It is noted here that in the present simulation, we assumed that all components are modulated by the ideal SLM under ideal conditions. However, in the application of LCoS-SLM to actual optical systems, device-level crosstalk caused by phase flicker and fringing field effects cannot be ignored. With reference to the wavelength-selective switches based on phase-only LCoS devices, the Cambridge group considered a simulated annealing process to reduce crosstalk between the different channels to less than -40 dB for all ports [12]. Thus, it is essential to reduce crosstalk by adjusting the relative parameters of the system.

Table 5.2. Coupling efficiency (dB) of each mode in core 19.

	LP_{01}	LP_{11a}	LP_{11b}	LP_{21a}	LP_{21b}	LP_{02}
LP_{01}	-0.8	-21.1	-22.0	-62.1	-42.3	-42.2
LP_{11a}	-21.1	-0.8	-42.3	-21.1	-22.0	-21.1
LP_{11b}	-22.0	-42.3	-0.8	-21.9	-21.1	-22.0
LP_{21a}	-62.1	-21.1	-21.9	-0.9	-103.7	-56.2
LP_{21b}	-42.3	-22.0	-21.1	-103.7	-0.9	-36.3
LP_{02}	-42.2	-21.1	-22.0	-56.2	-36.3	-0.9

5.4 6M-19CF signal path switching experiment

We experimented fiber joint switching in a 6M-19CF comprising six LP modes. The six modes, namely LP_{01}, LP_{11a}, LP_{11b}, LP_{21a}, LP_{21b}, and LP_{02}, are propagated in each core. Herein, we describe

the experimental setup in detail and show that the signal paths can be selectively switched by the LCoS-PSLM and mode-field patterns of the diffracted light can be maintained after joint switching.

5.4.1 Experimental setup

Figure 5.5 shows the experimental setup for the PSLM-based OFJS. In the graded-index trench-assisted 6M-19CF that maintains a small coupling between the modes, the length is 10 m, cladding diameter is 267 μm, core pitches between the outer, inner, and center cores are 51.1 μm, 51.2 μm, and 50.8 μm, respectively. The pixel size of the PSLM (Santec SLM-100) is 10 μm, and the gap between each pair of adjacent pixels is 0.4 μm. The phase shift of the PSLM is 2π, and a low-coherence amplified spontaneous emission (ASE) light source is used in the experiments. The light source is filtered to obtain a Gaussian-shaped spectrum at the center wavelength of 1550 nm with a full-width at half maximum bandwidth of 10 nm. The optical path is divided into the signal and reference arms for low-coherence digital holography (LCDH) based on Mach–Zehnder interferometry. At the signal arm, six modes are simultaneously launched into the 6M-19CF as the light signal. The light signal is cleaned up and collimated using an objective lens and a pinhole after passing through the 6M-19CF. The collimated light is then modulated by the blazed grating pattern on the PSLM display. Here, number of output ports is set to two, namely ports A and B. At the reference arm, the light is applied to a standard SMF as the reference. The length of the reference light path is shifted in steps of 100 μm using a translation stage to acquire specific spatial modes. Then, the reference light is modulated to horizontally polarized light using a quarterwave plate and halfwave plate to interfere with the light signal. The interference fringes of the light signal and each of the spatial modes are sequentially captured by a charge-coupled device (CCD, Xenics XS-4234).

In the experiments, we evaluate the performance by two methods. The first method evaluates the relationship between the intensity of diffracted light and diffraction angle. The light signal emitted from the 6M-19CF is switched to the target output port by the PSLM by changing the grating pattern displayed on the PSLM, and the intensity of the diffracted light related to the diffraction angle is evaluated. The second method involves detecting the mode-field pattern of the diffracted light in each core after joint switching by the LCDH [13,14]. LCDH allows easy derivation of the mode fields from interferograms. First, the intensity distribution of the reference light is captured and stored. Then, the interferograms are obtained at different stage positions. The mode fields of the diffracted light $E(x,y;\tau)$ are finally obtained from each interferogram as follows:

$$E(x,y;\tau) = IFFT\left\{FFT\left[\frac{I(x,y;\tau)}{\sqrt{I_r(x,y)}\exp(-i\theta)}\right]\times W\right\} \tag{5.3}$$

where τ is a temporal delay corresponding to the relative position of the translation stage, θ is the angle between light signal and reference light on the CCD camera. W is a circular window function,

which is a rectangle filter used to extract the mode field; the window size depends on the size of mode fields. $I(x,y;\tau)$ is an interferogram, and $I_r(x,y)$ is the intensity distribution of the reference light captured on the CCD camera. FFT $\{\cdot\}$ and IFFT $\{\cdot\}$ are the operators of the fast Fourier transform and inverse fast Fourier transform, respectively.

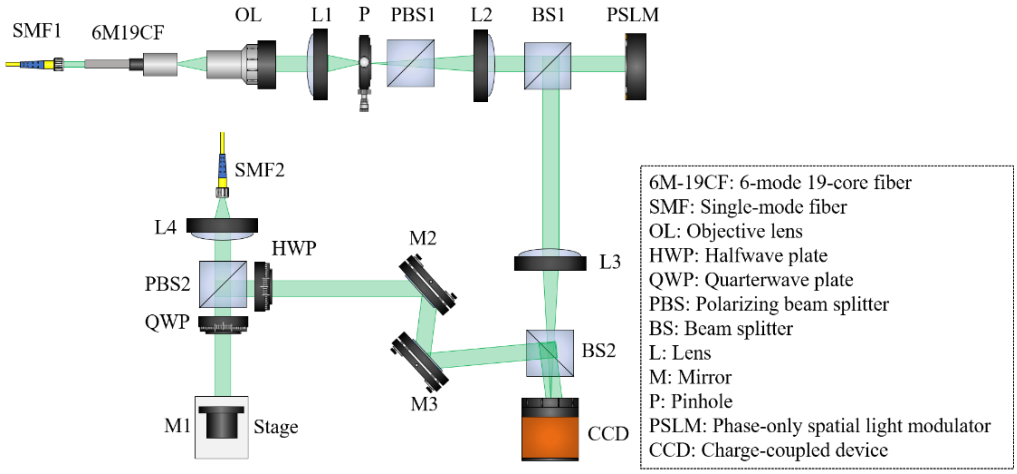

Figure 5.5. Experimental setup for 6M-19CF joint switch.

5.4.2 Results and discussion

Figure 5.6 shows the dependence of the intensity of the normalized first-order diffracted light on the diffraction angle. The dots in the figure indicate the experimental measurements. These values were obtained by measuring the intensities at the first diffraction order for displaying the various phase patterns corresponding to the different diffraction angles. Comparing the intensities of the diffracted light at the target output port for diffraction angles of 0.3° and 3.0°, the intensity loss is noted to be about 1.6 dB. This shows that the intensity of the first-order diffracted light decreases as the diffraction angle increases. A lower diffraction power for the first-order diffracted light indicates higher diffraction power for the other orders. The main reasons for this intensity reduction are assumed as the fill factor and fringing field effect [9,15]. Without considering the output position, the device-system crosstalk is related to the diffraction efficiency of the blazed grating on the SLM display. For a simplified model of the fringing field effect [16], the diffraction efficiency is calculated as

$$\eta \approx \left(1-\frac{\Delta X_{FB}}{\Lambda}\right)^2 \tag{5.4}$$

where η is the blazed grating diffraction efficiency, Λ is the length of the grating period, and ΔX_{FB} is the fly-back zone width, which is defined as the broadening width of the phase profile. The grating equation is given as

$$\Lambda = \frac{\lambda}{2\sin\theta} \tag{5.5}$$

where λ is the wavelength, and θ_d is the diffraction angle. We thus conclude that the intensity of the first-order diffracted light decreases when the diffraction angle increases (grating period decreases), which is in accordance with the theoretical prediction.

We also experiment switching of the signal path by granting a diffraction angle to the light signal on the horizontal axis. Figure 5.7 shows the diffracted light modulated by the PSLM. The diffracted light is routed to output port A when θ_d = 1.27°, as shown in Fig. 5.7(a), and the light is routed to output port B when θ_d = -1.27°, as shown in Fig. 5.7(b). The red, white, and blue frames represent the diffracted light signals at port A, zero diffraction order, and port B, respectively. The intensity distribution of the diffracted light indicates that the light signal can be selectively routed to the target output port by the SLM-based OFJS. We evaluate the switching performance by calculating the crosstalk (XT) between the output ports as

$$XT = 10\log_{10}\left(\frac{I_o}{I_s}\right) \tag{5.6}$$

where I_o is the intensity of diffracted light at the other output ports; I_s is the intensity of diffracted light at the target output port. As shown in Fig. 5.7, when the light signal is routed to the target output port, other higher order diffracted light signals are generated. Here, it is noted that crosstalk is the light diffracted to orders other than the first order and coupled into the non-selected output port; in other words, only the components output from the target port are considered as crosstalk. Owing to the output ports being set symmetrically along the horizontal axis, for light signals routed to output port A, the first-order diffracted light generated at port A is regarded as the signal, and the negative first-order diffracted light generated at port B is regarded as crosstalk. In the case of the light signal routed to output port B, the first-order diffracted light at port B is regarded as the signal, and the negative first-order diffracted light generated at port A is regarded as crosstalk. The components of the other-order diffracted light signals are not considered as crosstalk because they are not output from port A or B in this experiment. Thus, as shown in Table 5.3, when the signal path is routed to port A, it causes crosstalk with -15.1 dB at the position of the zero-order beam and -11.6 dB at port B. Compared with the intensity of the input light signal, the intensity loss at port A is -1.4 dB. When the signal path is routed to port B, it causes crosstalk with -13.1 dB at the position of the zero-order beam and -14.7 dB at port A. The intensity loss at port B is -0.7 dB. However, the intensity loss and crosstalk values should be the same because the output ports are symmetric about the horizontal axis. This can be attributed to the alignment error of the system and difference between optical paths when passing through the beam splitter. From the results, the intensity loss at the target output port is less than -1.4

dB, and the maximum port crosstalk is -11.6 dB. It is essential to reduce the crosstalk for OFJS with low insertion loss.

Moreover, we also measured the mode-field patterns of the diffracted light in the outer core (core 1), inner core (core 13), and center core (core 19) by LCDH. The diameter of the circular window was set to 18.4 μm to be equal to the core diameter. The specific mode-field patterns were measured by changing the optical length of the reference light using a translation stage. However, the modes of LP_{21} and LP_{02} could not be sufficiently separated owing to strong coupling in the fiber under test; hence, the coupling mode-field patterns of LP_{21} and LP_{02} are obtained. Table 5.4 shows the measured results of each mode pattern in the core. The pixel pitch is 30 μm, and the captured size is 50 × 50 pixels. As shown in Table 5.4, although the mode-field patterns are slightly distorted by the imperfections of the hologram on the SLM, the mode patterns are maintained when the signal path is jointly switched by the OFJS. The above results confirm that the signal path can be selectively switched by the PSLM-based OFJS while maintaining the mode-field patterns.

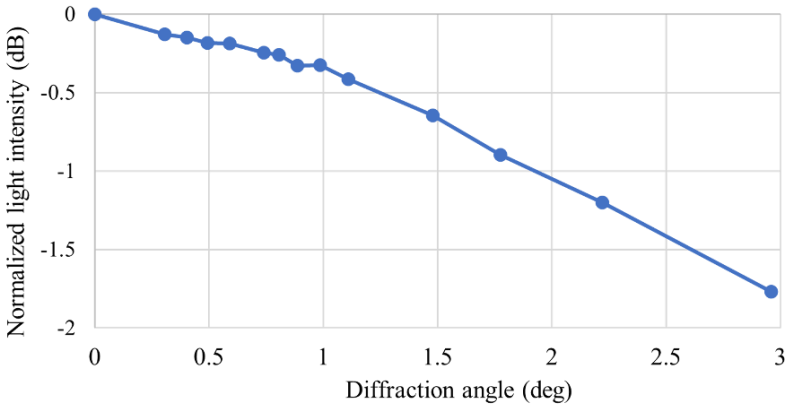

Figure 5.6. Normalized first-order diffracted light intensity for various difference angles.

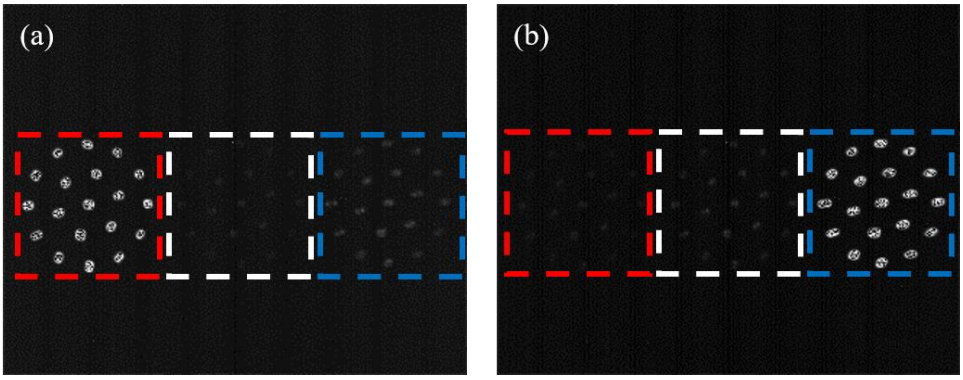

Figure 5.7. Diffracted light signals modulated by the PSLM along the horizontal axis. The red frame represents port A, white frame represents the zeroth diffracted beam, and blue frame represents port B. (a) Diffracted light when θ_d is set along the horizontal axis with 1.27°. (b) Diffracted light when θ_d is set along the horizontal axis with -1.27°.

Table 5.3. XT (dB) from each output port along the horizontal axis.

Port A	Zeroth	Port B
0	-15.1	-11.6
-14.7	-13.1	0

Table 5.4. Mode-field patterns of the diffracted light signals in cores 1, 13, and 19.

	LP_{01}	LP_{11}	LP_{21} and LP_{02}
	Amplitude/Phase	Amplitude/Phase	Amplitude/Phase
Core 1	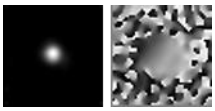	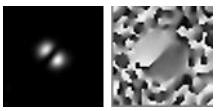	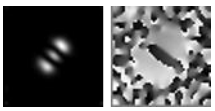
Core 13	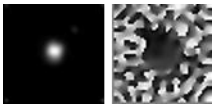	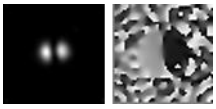	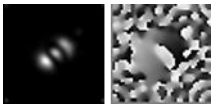
Core 19	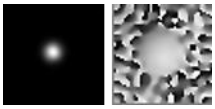	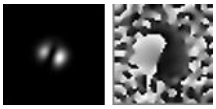	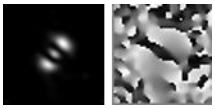

5.5 Port crosstalk reduction

In Section 5.4, we experimented SLM-based optical fiber joint switch in a 6M-19CF. As the experiment results, when the output ports are set symmetrically along the horizontal axis, the maximum port crosstalk is -11.6 dB. Thus, it is essential to reduce the crosstalk for OFJS with low insertion loss. As noted above, When the signal path is switched by the OFJS, other order diffracted light signals are also generated along the horizontal axis. The components that overlap with the target output port are regarded as crosstalk. Under this circumstance, if the output ports are set along different axes as shown in Fig. 5.8, it is possible to reduce the effect of crosstalk components generated from the other diffraction orders on the target output ports. In this section, we introduce the principle and experiment with reducing the port crosstalk by changing the output fiber position.

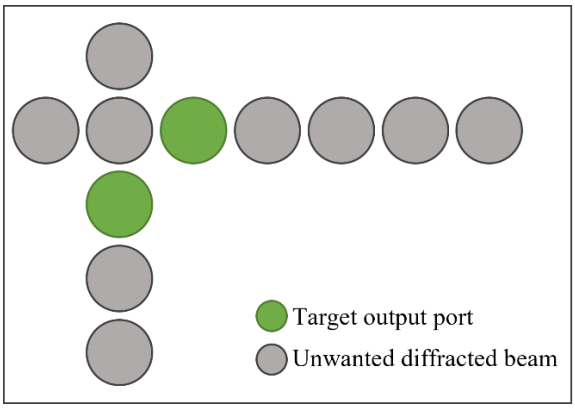

Figure 5.8. Schematic of output ports arranged along different axes.

5.5.1 Experimental setup

As noted above, the system-level port crosstalk can be reduced by adjusting the output fiber position. This strategy uses the inefficient coupling of higher diffraction orders with the target output port. The experimental setup and experimental parameters are the same as shown in Section 5.4. In the experiment, six modes LP_{01}, LP_{11a}, LP_{11b}, LP_{21a}, LP_{21b}, and LP_{02}, are simultaneously launched into the 6M-19CF as the light signal. The light signals are modulated by the blazed grating pattern on the PSLM display. The light signal is then switched to the target outport port and captured by a CCD. The performance is evaluated by the port crosstalk and intensity loss. Figure 5.9 shows the position of output ports. The number of output ports is set to two: ports A and B. In Section 5.4, two output ports are set symmetrically along the horizontal axis as shown in Fig. 5.9(a). The diffracted angle is set to 1.27°. In this section, two output ports are set along horizontal and vertical axes as shown in Fig. 5.9(b). The diffracted angle is set along the horizontal axis and vertical axis with 1.27°, respectively.

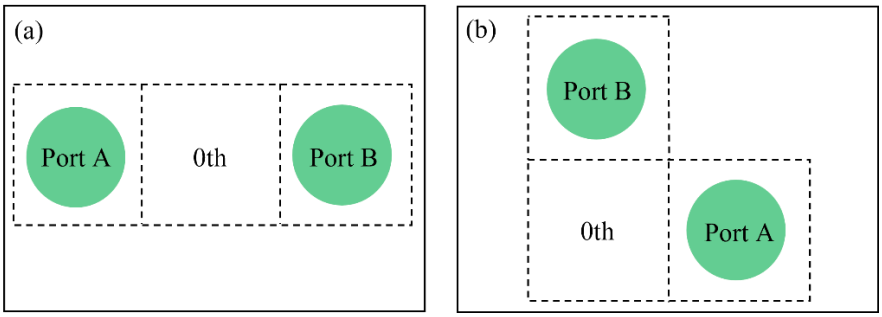

Figure 5.9. Position of the output ports.(a) Output ports are set along the horizontal axis. (b) Output ports are set along the horizontal and vertical axes.

5.5.2 Results and discussion

The experimental results in Table 5.3 indicated that when the signal path is switched by OFJS, the negative first-order diffracted light will be regarded as crosstalk components for target output ports. When the signal path is switched to port A, it causes crosstalk with -11.6 dB at port B. When the signal path is switched to port B, it causes crosstalk with -14.7 dB at port A. Under this circumstance, if the output ports are set along different axes, the port crosstalk can be reduced because the components of the other-order diffracted light signals are not launched into the target output port. Based on the above theory, we performed experiments to verify the feasibility of the proposed method. Figure 5.10 shows the experimental results of the diffracted light modulated by the PSLM along horizontal and vertical axes. The red, white, and blue frames represent the diffracted light signals at port A, zero diffraction order, and port B, respectively. From the intensity distribution of the diffracted light at the output ports, the other-order diffracted light signals are not generated at the positions of the target output ports. As shown in Table 5.5, routing the signal path to port A causes a crosstalk of -15.3 dB at the position of

the zero-order beam and -25.1 dB at port B. The intensity loss is -1.2 dB at port A. When routing the signal path to port B, a crosstalk of -15.4 dB is seen at the position of the zero-order beam and -31.3 dB at port B. The intensity loss is -0.7 dB at port B; it is further noted that when the signal path is routed to port B, the intensity loss at the target port is almost the same for output ports set along the horizontal and different axes. Because there is no component overlap at the position of the zeroth order diffracted light in the experiment, compared with the switching performance of setting output ports along the same axis, the maximum port crosstalk is reduced from -11.6 to -25.1 dB for output ports along different axes without the influence from the zeroth-order diffracted light. These results show that the port crosstalk from other higher order diffracted light signals can be significantly reduced by changing the output positions. However, it is difficult to estimate the intermodal crosstalk in the experiments because arbitrary signal patterns are produced when the spatial mode is launched into each core. Moreover, as noted in Section 5.3, all components of the light signal are modulated by the ideal SLM under ideal conditions. In the experiments, the influences from several factors (e.g., lens thickness, fiber misalignments, and fringe-field effects) should be considered. The intermodal crosstalk in the experiments is expected to be greater than that observed from the results of numerical simulations, as shown in Table 5.2.

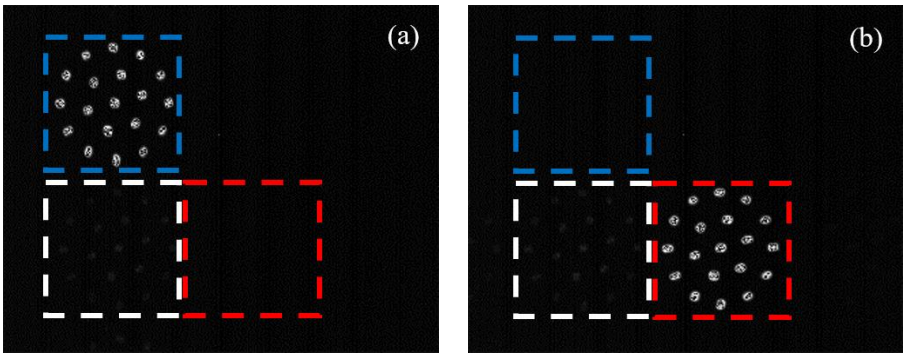

Figure 5.10. Diffracted light signals modulated by the PSLM along the horizontal and vertical axes. The red frame represents port A, white frame represents the zeroth diffracted beam, and blue frame represents port B. (a) Diffracted light when θ_d is set along the horizontal axis with 1.27°. (b) Diffracted light when θ_d is set along the vertical axis with 1.27°.

Table 5.5. XT (dB) from each output port along the horizontal and vertical axes.

Port A	Zeroth	Port B
0	-15.3	-25.1
-31.3	-15.4	0

On the other hand, when the number of output ports exceeds two, the crosstalk also can be reduced by adjusting their diffraction angles and output positions based on the above observations. As shown in Fig. 5.6, the intensity of the first-order diffracted light decreases when the diffraction angle increases

(grating period decreases). Moreover, the experimental results show that the port crosstalk from other higher-order diffracted light signals can be significantly reduced by changing the output port positions. On the other hand, the intensity loss at target ports is lower than -1.4 dB when the light signal is switched horizontally or vertically. Thus, even if the number of output ports exceeds two, the port crosstalk can be reduced by adjusting the diffraction angle and the output port positions. we experiment with the switching of the signal path by granting a diffraction angle to the light signal on the different axes when the output ports are set to three. As shown in Fig. 5.11, the blue frame, red frame, and white frame represent port A, port B, and port C, respectively. Due to the limitation of the display size of the SLM, the port A and B are set along the horizontal axis. Port C is set along the vertical axis. As shown in Table 5.6, when the signal path is switched to port A, it causes crosstalk with -13.7 dB at port B and -26.9 dB at port C. When the signal path is switch to port B, it causes crosstalk with -17.0 dB at port A and -24.1 dB at port C. When the signal path is switch to port C, it causes crosstalk with -20.6 dB at port A and -22.5 dB at port B. As the results show, crosstalk at port C is smaller than that of port A and port B, indicating that port crosstalk can be improved by adjusting the output port positions. Thus, for the SLM-based joint switch, the crosstalk can be reduced by changing the output positions when the number of the output ports exceeds two.

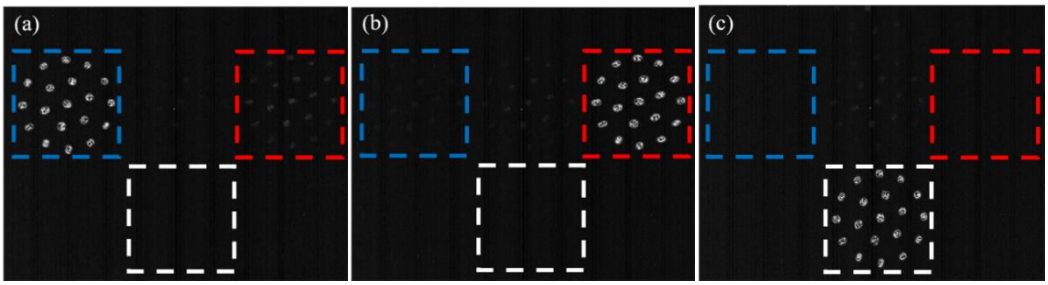

Figure 5.11. Diffracted light signals modulated by the PSLM along different axes. The blue frame represents port A, red frame represents port B, and while frame represents port C. (a) Diffracted light when θ_d is set along the horizontal axis with 1.27°. (b) Diffracted light when θ_d is set along the horizontal axis with -1.27°. (c) Diffracted light when θ_d is set along the vertical axis with -1.27°.

Table 5.6. XT (dB) from each output port along different axes.

Port A	Port B	Port C
0	-13.7	-26.9
-17.0	0	-24.1
-20.6	-22.5	0

5.6 Summary

In this chapter, to realize simplified cost-efficient optical networks with switching flexibility and scaling potential, a spatial-light-modulator-based optical-fiber joint switch for few-mode multicore fibers is proposed herein, which can switch all the spatial channels together as a unit. Numerical simulations and experiments were conducted, and the results show that the signal paths for a 6-mode 19-core fiber can be switched to the target output ports by the proposed method simultaneously. Moreover, the intensity of the first-order diffracted light at the target output port decreases as the diffraction angle increases, and the complex mode-field patterns were maintained even after joint switching. It is noted that compared with the switching performance of setting the output ports along one axis, the maximum port crosstalk reduced from -11.6 to -25.1 dB when the output ports were set along different axes. Moreover, even if the number of output ports exceeds two, the crosstalk also can be reduced by adjusting their diffraction angles and output positions based on the above observations.

References

[1] R. Ryf, S. Randel, A. H. Gnauck, C. Bolle, A. Sierra, S. Mumtaz, M. Esmaeelpour, E. C. Burrows, R.-J. Essiambre, P. J. Winzer, D. W. Peckham, A. H. McCurdy, and R. Lingle, "Mode-division multiplexing over 96 km of few-mode fiber using coherent 6 × 6 MIMO processing," J. Light. Technol. **30**(4), 521-531 (2012).

[2] Y. Awaji, "Review of space-division multiplexing technologies in optical communications," IEICE Trans. Commun. **E102-B**(1), 1-16 (2019).

[3] D. J. Richardson, J. M. Fini, and L. E. Nelson, "Space-division multiplexing in optical fibres," Nat. Photonics **7**(5), 354-362 (2013).

[4] D. Soma, Y. Wakayama, S. Beppu, S. Sumita, T. Tsuritani, T. Hayashi, T. Nagashima, M. Suzuki, M. Yoshida, K. Kasai, M. Nakazawa, H. Takahashi, K. Igarashi, I. Morita, and M. Suzuki, "10.16-peta-b/s dense SDM/WDM transmission over 6-mode 19-core fiber across the C+L band," J. Light. Technol. **36**(6), 1362-1368 (2018).

[5] P. J. Winzer and G. J. Foschini, "MIMO capacities and outage probabilities in spatially multiplexed optical transport systems," Opt. Express **19**(17), 16680-16696 (2011).

[6] D. M. Marom and M. Blau, "Switching solutions for WDM-SDM optical networks," IEEE Commun. Mag. **53**(2), 60-68 (2015).

[7] N. K. Fontaine, T. Haramaty, R. Ryf, H. Chen, L. Miron, L. Pascar, M. Blau, B. Frenkel, L. Wang, Y. Messaddeq, S. LaRochelle, R. J. Essiambre, Y. Jung, Q. Kang, J. K. Sahu, S. U. Alam, D. J. Richardson, and D. M. Marom, "Heterogeneous space-division multiplexing and joint wavelength switching demonstration," Proc. Opt. Fiber Commun. Conf. (OFC), Th5C.5 (2015).

[8] N. Collings, T. Davey, J. Christmas, and B. Crossland, "The applications and technology of phase-only liquid crystal on silicon devices," J. Disp. Technol. **7**(3), 112-119 (2011).

[9] M. Wang, L. Zong, L. Mao, A. Marquez, Y. Ye, H. Zhao, and F. J. V. Caballero, "LCoS SLM study and its application in wavelength selective switch," Photonics **4**(2), 22 (2017).

[10] Z. Guo, J. Yan, Y. Xing, Y. Zheng, and Q. Li, "A novel three electrodes structure LCoS with low fringing field effect," SID Symp. Dig. Tech. Papers **47**(1), 183-184 (2016).

[11] M. Persson, D. Engström, and M. Goksör, "Reducing the effect of pixel crosstalk in phase only spatial light modulators," Opt. Express **20**(20), 22334-22343 (2012).

[12] H. Yang, B. Robertson, and D. Chu, "Crosstalk reduction in holographic wavelength selective switches based on phase-only LCOS devices," Proc. Opt. Fiber Commun. Conf. (OFC), Th2A.23 (2014).

[13] Y. Wakayama, H. Taga, and T. Tsuritani, "MFD measurement of a six-mode fiber with low-coherence digital holography," IEICE Trans. Commun. **E100-B**(10), 1734-1739 (2017).

[14] Y. Wakayama, H. Taga, K. Igarashi, and T. Tsuritani, "DMD measurement of 114-SDM transmission fibre using low-coherence interferometry with digital holographic processing," 41st Eur. Conf. Exhibit. Opt. Commun. (ECOC), P.1.19 (2015).

[15] I. Morenoa, B. K. Gutierrez, M. M. Sánchez-López, J. A. Davis, H. P. Khanal, and D. M. Cottrell, "Diffraction efficiency of stepped gratings using high phase-modulation spatial light modulators," Opt. Lasers Eng. **126**, 105910 (2020).

[16] U. Efron, B. Apter, and E. B. Treidel, "Fringing-field effect in liquid-crystal beam-steering devices: an approximate analytical model," J. Opt. Soc. Am. A **21**(10), 1996-2008 (2004).

Chapter 6

Conclusion

To satisfy the increasing communication traffic demands, space-division multiplexing (SDM) transmission systems have been investigated as potential candidates for a breakthrough technology to offset this capacity crunch. To realize simplified cost-efficient SDM optical networks with scaling potential, in this paper, we have proposed and developed two spatial mode conversion schemes: the spatial mode exchange technique using volume holography (VHET) for mode division multiplexing (MDM) systems, and the spatial-light-modulator-based optical-fiber joint switch (SLM-based OFJS) for few-mode multi-core fiber (FM-MCFs) systems. The VHET as the main technology can reduce differential mode delay (DMD) by exchanging the spatial modes with different transmission speeds in few-mode fibers (FMFs) requiring only a single holographic medium, which is independent of the number of multiplexed modes. Moreover, it is also a crucial technique for mode conversions between foundational modes and high-order modes in MDM systems, which supports the flexibility of the optical networks. The SLM-based OFJS is a cost-effective integration technique with a simple configuration that can switch all signal paths as a unit in an optical free space to obtain a greater throughput; in addition, it can achieve selective operation by changing the SLM display patterns. Further, we proposed improved methods to suppress cross-talks to improve conversion preformation.

In Chapter 2, the configuration and key technologies of SDM transmission systems were introduced in detail. SDM technologies includes two approaches: mode division multiplexing using FMFs and core multiplexing using MCFs, treating each core/mode as an independent optical path. Thus, in SDM systems, mode conversion techniques are essential to connect different types of fibers in SDM transmission systems. The volume holograms and spatial light modulators as the key components used for the mode conversion techniques proposed were introduced. Due to the practical application of holography depends largely on the properties of recording materials, photopolymers were chosen as the recording medium in our study due to their ease of preparation, high dynamic range, and self-processing. On the other hand, liquid crystal on silicon SLMs, the reflective micro-display technology, were chosen for the mode conversion in FM-MCFs due to the high spatial resolution, high light efficiency, and quick response.

In Chapter 3, VHET was proposed for mode exchange between high-order modes. In this scheme, VHET utilizes multiplexed volume holograms to exchange multiplexed spatial modes simultaneously.

Thus, the cost and the size of the optical system are markedly lower because this scheme requires only a volume hologram medium, which is independent of the number of multiplexed modes. To confirm the basic operation of the proposed method, a mode-exchange numerical simulation was conducted using an LP mode group comprising of LP01, LP11, and LP21. Moreover, dual-wavelength method was proposed to realize the application of VHET in the practical optical transmission bands. As a result, in the exchange of the two modes, the CEs were beyond 53.6% and the maximum crosstalk was -24.5 dB. In the exchange of three modes, the CEs were beyond 17% and the maximum crosstalk was 0.4 dB. Although the multiple spatial modes can be exchanged simultaneously by the proposed method, it is essential to reduce the crosstalk to improve the reconstruction quality. Moreover, the simulation results of the VHET combined with dual-wavelength method are the same as the conventional method, which indicated that VHET can be applied in the practical optical transmission bands by using dual-wavelength method.

In Chapter 4, we proposed three improved techniques for combing volume holograms with phase plates to improve the reconstruction quality without significantly increasing the number of optical elements. To confirm the basic operation of the proposed method, mode-exchange numerical simulations were conducted using an LP mode group comprising of LP01, LP11, and LP21. In VHET combined with a phase plate, the intensity of the signal beam was modulated by a phase plate. The overlap ratio between LP01 and LP11 was remarkably reduced from 0.49 to 0.26. The crosstalk was reduced from -1.49 dB to -23.5 dB. In VHET combined with a random optical diffuser, the intensity distribution of the signal beam is scattered uniformly by a random optical diffuser; this results in a high exchange performance. We then confirmed the dependence of the reconstruction quality on the diffusion angle during an attempt to acquire a better exchange performance. As a result, the CE was improved beyond 87%, and the maximum XTs were significantly suppressed to -15.8 dB. In VHET combined with the mode diffusion technique, the inter-page crosstalk can be removed by separating the signal and crosstalk components due to the propagation angle difference. By adjusting the diffusion angle of the random optical diffuser, the CE was improved beyond 78%, and the maximum XT was significantly suppressed to -14.7 dB. The exchange performance was remarkably improved by three proposed methods. Comparing these three improved methods, the exchange performance of VHET combined with a random optical diffuser is best according to the CE and XT characteristics.

In Chapter 5, to improve integration and reduce the cost of switching elements for SDM, a SLM-based OFJS is proposed in this chapter, which can switch all the signal paths of the FM-MCFs as a unit. Numerical simulations and experiments were conducted, and the results show that the signal paths for a 6-mode 19-core fiber can be switched to the target output ports by the proposed method simultaneously. Moreover, the intensity of the first-order diffracted light at the target output port decreases as the diffraction angle increases, and the complex mode-field patterns were maintained even after joint switching. It is noted that compared with the switching performance of setting the output ports along one axis, the maximum port

crosstalk reduced from -11.6 to -25.1 dB when the output ports were set along different axes. Further, even if the number of output ports exceeds two, the crosstalk can be reduced by changing the output positions.

We proposed and developed two spatial mode conversion techniques in this study. The simulation and experiment results show that spatial mode conversion techniques can convert the mode effectively in FMFs or MF-MCFs with low crosstalk. Nonetheless, there are still many points in the proposed scheme need to be optimized. In this work, we only confirmed the basic operation of VHET by using three spatial modes. Although the transmission capacity of MDM systems using three modes can meet the current traffic demand, for the maximum transmission capacity of MDM systems based on FMFs, six modes are expected to be applied. Therefore, increasing the number of spatial modes applied in VHET is a priority for future research. On the other hand, dense SDM transmission systems are widely investigated to satisfy the significantly increasing communication traffic. Typically, the number of channels in a dense SDM exceeds 30, thus, the crosstalk between channels is relatively high. The crosstalk reduction is a critical problem to be solved in future research. Moreover, the mode conversion technique using SLM allows for core-to-core and mode-to-mode switching in addition to fiber joint switching. The combination of fiber joint switching and core switching can improve the flexibility and granularity of the dense SDM networks. This is also a promising research topic for future research.

Acknowledgments

Undertaking the doctoral degree in information science and technology at Hokkaido University has been a truly life-changing experience for me, and it would not have been possible without the support and guidance that I received from many people.

First and foremost, I would like to express my deep and sincere gratitude to my supervisor, Prof. Atsushi Okamoto, for giving me the opportunity to do research and providing invaluable guidance throughout this research. He led me into the fieldwork of optics and taught me the methodology to carry out the research. The completion of this study could not have been possible without his guidance. His vision, sincerity, and profession have deeply inspired me. Besides, he is not only a research supervisor but also a warm-hearted life mentor. He remembered my desire to be a researcher, and helped me greatly in my life and career. His wife is very kind, and his daughters are so-cute. It is a great honor and luck to study under his guidance.

My sincere thanks go to Prof. Akihisa Tomita, who generously provided professional guidance and research assistance. His insightful suggestions and comments have significantly improved the quality and presentation of my research. Many thanks are to Prof. Sueoka Kazuhisa for his invaluable advice on my research and thesis. I also thank all professors and staff of information science and technology at Hokkaido University for their support and kindness.

I deeply appreciate the support from the collaborative work with the company and research institution. I am especially grateful to Mr. Yuta Goto, Mr. Satoshi Shinada, and Mr. Naoya Wada of the National Institute of Information and Communications Technology (NICT), Mr. Daiki Soma, Mr. Yuta Wakayama, and Mr. Takehiro Tsuritani of KDDI Research, Inc., and Mr. Taketoshi Takahata of OPTOQUEST Co., Ltd., and others who were always so helpful and provided me with their assistance throughout my dissertation.

A very special thanks to Assistant Prof. Tomohiro Maeda of Aoyama Gakuin University, Mr. Shijie Zhou of Oplink communications, Mr. Taijun Shiba, and Mr. Yuta Abe for their invaluable guidance and feedback on my research. They taught me knowledge about optics and always answer my questions which laid the foundation for my research. Their invaluable instruction improved my presentation quality, and there is no doubt that they are my second mentors.

I am indebted to all my research colleagues and friends who always encourage me and help me in numerous ways. Special thanks to Dr. Weiyang Zhang, Mr. Yamagishi Nobuhiro, Mr. Haobo Ge, Mr. Zeyu Shen, Ms. Jingyan Yang, Ms. Xinruinan Zhang, Mr. Ryo Watanabe, and Mr. Jianlian Wang. Thanks for their friendship extended to me, making me feel so warm.

I gratefully acknowledge the funding received from the D-Drive research assistance of Hokkaido University which helped me reduce my tuition burden, and the scholarship received from the China

scholarship council program which helped me reduce my life burden.

I am incredibly grateful to my parents for their love, always believing in me and encouraging me to follow my dreams. And I special thank my brother for his support, understanding, and taking responsibility for taking care of our parents. I also thank Mr. Xin Gong for his love and helping me through the tough time.

Thanks to all the people who have supported me in my research career. I am so lucky to meet them.

February 14, 2023
Graduate School of Information Science and Technology
Hokkaido University
Shuanglu Zhang

Research Achievements

1 Original articles

1.1 Scholarly journal articles

[1] Shuanglu Zhang, Atsushi Okamoto, Taijun Shiba, Hotaka Hayashi, Kazuhisa Ogawa, Akihisa Tomita, Taketoshi Takahata, Satoshi Shinada, Yuta Goto, and Naoya Wada, "Spatial mode exchange technique using volume holograms with a random optical diffuser for reduction of crosstalk," Optical Review, Vol. 28, No. 2, pp. 181–189 (2021). (IF=0.89)

[2] Shuanglu Zhang, Atsushi Okamoto, Yuta Abe, Ryo Watanabe, Akihisa Tomita, Daiki Soma, Yuta Wakayama, and Takehiro Tsuritani, "Spatial-light-modulator-based opticalfiber joint switch for few-mode multicore fibers," Optics Express, Vol. 29, No. 24, pp. 39096–39106 (2021). (IF=3.894)

1.2 International conference proceedings

[1] Shuanglu Zhang, Atsushi Okamoto, Kazuhisa Ogawa, and Akihisa Tomita,"Spatial Mode Exchange Technique Using Volume Hologram with a Phase Plate," Proc. of 29th International Symposium on Imaging, Sensing, and Optical Memory 2019 (ISOM'19), Niigata, Japan, October, Tu-J-189, pp. 91–92 (2019).

[2] Shuanglu Zhang, Atsushi Okamoto, Taijun Shiba, Hotaka Hayashi, Kazuhisa Ogawa, Akihisa Tomita, Taketoshi Takahata, Satoshi Shinada, Yuta Goto, and Naoya Wada,"Spatial mode exchange technique using volume holograms with a random optical diffuser to reduce modal cross-talks," Proc. of SPIE (Photonics West 2020), San Francisco, USA, February, 11309, pp. 11309-1–11309-8 (2020).

[3] Zhang Shuanglu, Atsushi Okamoto, Kazuhisa Ogawa, Akihisa Tomita, Taketoshi Takahata, Satoshi Shinada, Yuta Goto, Naoya Wada, "Improving the reconstruction quality of spatial mode exchange technique by adjusting the diffusion angle of diffuser," Proc. of 30th International Symposium on Imaging, Sensing, and Optical Memory 2020 (ISOM'20), online, Japan, November, Mo-C-01, pp. 35–36 (2020).

[4] Zhang Shuanglu, Atsushi Okamoto, Akihisa Tomita, "Mode diffusion technique for crosstalk reduction in volume holographic mode exchanger," Proc. of 32th International Symposium on Imaging, Sensing, and Optical Memory 2022 (ISOM'22), Sapporo, Japan, August, P-ITu-09 (2021).

2 Co-authored articles

2.1 Scholarly journal articles

[1] Zeyu Shen, Atsushi Okamoto, Shuanglu Zhang, Akihisa Tomita, “Spatial mode compensation technique using Progressive Phase Conjugation,” Optical Review, Vol. 29, pp. 440–449 (2022). (IF=0.89)

2.2 International conference proceedings

[1] Zeyu Shen, Atsushi Okamoto, Shuanglu Zhang, Akihisa Tomita, “Improvement of mode compensation accuracy using a random diffuser in progressive phase conjugation,” Proc. of 31th International Symposium on Imaging, Sensing, and Optical Memory 2021 (ISOM’21), Online, Japan, October, We-B-03, pp. 133–134 (2021).

3 Presentation

[1] 張霜露, 岡本淳, 小川和久, 富田章久, “モード分割多重伝送におけるモード間群遅延差の低減に向けた体積ホログラムを用いたモード交換技術,” 平成 30 年度電気・情報関係学会北海道支部連合大会, 137, 札幌, 2018 年 10 月.

[2] 張霜露, 岡本淳, 柴泰純, 小川和久, 富田章久, 高畠武敏, 品田聡, 和田尚也, “モード分割多重通信における体積ホログラムを用いた空間モード交換技術,” 第 32 回光通信システムシンポジウム, P-36, 三島, 2018 年 12 月.

[3] 張霜露, 岡本淳, “体積ホログラムを用いた空間モード交換技術,” 国際光デーシンポジウム 2019, P-53, 東京, 2019 年 6 月.

[4] 張霜露, 岡本淳, 富田章久, “体積ホログラムを用いたモード分離器におけるクロストーク低減に向けたモード拡散技術,” 令和 4 年度 マルチメディアストレージ研究会 (ITE-MMS), 14, オンライン, 2022 年 2 月.

4 Award

[1] 30th International Symposium on Imaging, Sensing, and Optical Memory 2020 (ISOM’20), Student Award, November 2020. (Article: Shuanglu Zhang, Atsushi Okamoto, Kazuhisa Ogawa, Akihisa Tomita, Taketoshi Takahata, Satoshi Shinada, Yuta Goto, and Naoya Wada, “Improving the reconstruction quality of spatial mode exchange technique by adjusting the diffusion angle of diffuser,” ISOM’20 Technical Digest, Mo-C-01, 2020).